Investigation of the diffusion of U(VI) and Am(III) through Opalinus Clay down to ultra-trace levels

Zur Erlangung des akademischen Grades eines
DOKTORS DER NATURWISSENSCHAFTEN
(Dr. rer. nat.)
von der KIT-Fakultät für Chemie und Biowissenschaften
des Karlsruher Instituts für Technologie (KIT)

genehmigte

DISSERTATION

von

M. Sc. Daniel Glückman

Referent: Prof. Dr. Horst Geckeis
Korreferentin: Prof. Dr. Petra Panak
Tag der mündlichen Prüfung: 26.10.2022

Statement of originality / Erklärung

Ich versichere hiermit, die vorliegende Arbeit selbstständig verfasst und keine anderen Quellen oder Hilfsmittel verwendet zu haben als die hier angegebenen. Außerdem versichere ich, dass alle Stellen der Arbeit, die aus anderen Quellen wörtlich oder sinngemäß übernommen wurden, als solche kenntlich gemacht worden sind und die schriftliche Version der Arbeit mit der digitalen übereinstimmt. Die Arbeit wurde in gleicher oder ähnlicher Form noch bei keiner anderen Prüfungsbehörde vorgelegt. Die Satzung des Karlsruher Instituts für Technologie zur Sicherung guter wissenschaftlicher Praxis wurde in der jeweils gültigen Fassung beachtet. Des Weiteren versichere ich, dass die Arbeit in ähnlicher oder gleicher Form noch keiner Prüfungskommission vorgelegt wurde.

…… ……

(place and date / Ort und Datum) (signature / Unterschrift)

Acknowledgements / Danksagung

First and foremost, I would like to express my deep gratitude to the institute head of KIT-INE, Prof. Dr. Horst Geckeis, for offering me the opportunity to do research on this fascinating and promising scientific field and for have given me valuable scientific input in numerous refreshing discussions. Furthermore, I want to express my deep appreciation and gratitude to my supervisors Dr. Francesca Quinto and Dr. Claudia Joseph for teaching me all the skills and knowledge necessary to tackle the topic of this Ph.D. Their unlimited support and patience during countless scientific and personal conversations is unforgotten. I also want to give a very special thanks to my department head Dr. Volker Metz, who not only offered me constant support in scientific matters — his pleasant and humorous nature also helped me with staying motivated and optimistic.

I also want to thank my colleagues Aline Thumm, Florian Steegborn, Neşe Çevirim-Papaioannou, Pelin Çakir-Wuttke, Péter Szabó, Philipp Müller, Sarah Duckworth, Tim Platte, Tobias König, and Yasmine Kouhail. They were not just colleagues, but have become great friends over the course of the years.

I want to thank the analytics group, in particular Frank Geyer, Cornelia Beiser, Annika Fried, and Elvira Rolgejzer for offering me scientific input and assistance with the ICP–MS measurements, Stefanie Kuschel for performing IC analyses, as well as Melanie Böttle and Tanja Kisely for helping me with laboratory equipment. A big thanks goes also to the INE workshop, in particular to Volker Krepper and Kirsten Hardock, for planning and building the diffusion reservoirs. Furthermore, I want to thank Frank Heberling for his input on the PHREEQC calculations. I would like to thank the entire INE institute for everybody´s readiness to help and the excellent working atmosphere.

My biggest thanks goes to the staff of the Vienna Environmental Research Accelerator Faculty of Physics — Isotope Physics, in particular to Ass.-Prof. Dr. Karin Hain and Ass.-Prof. Mag. Dr. Peter Steier for their continuous and profound support in AMS analysis and data evaluation.

I also want to thank Dr. Yuankai Yang (FZJ) for his input on data interpretation and Dr. Martin Glaus (LES-PSI), Dr. Luc van Loon (LES-PSI), and Prof. Dr. Tobias Reich (JGU Mainz) for their support during the planning of the diffusion experiments, as well as Adrian Lindner (KIT-IAM-ET) for performing and interpreting the µCT scans.

In closing, I would like to thank my parents. Their continuous support and openness for every choice in my life allowed me to become who I am today.

Abstract

Clay rocks are considered as potential host rocks and geoengineered barriers for the disposal of high-level nuclear waste (HLW) in deep geological formations. Although the host rock, geoengineered barriers (e.g., bentonite), and engineered barriers (e.g., waste container) delay groundwater intrusion into the disposal rooms, long-term safety assessments for an HLW repository have to consider water ingress and the consecutive corrosion of containers and waste, resulting in the release of radionuclides. Potentially released actinides, such as uranium (U) and americium (Am), could be transported through the clay matrix of the geoengineered barrier and host rock mainly by diffusion. Actinides are known to exhibit low solubility and to sorb strongly onto clay surfaces under the reducing conditions of a repository. Diffusion experiments at the expected very low actinide concentrations are, thus, difficult to perform due to analytical constraints. Diffusion of U in clay rocks has not been investigated below concentrations of 10^{-4} mol/m³ clay. In the case of Am, up to now, no diffusion experiments have been performed in a clay rock, considered suitable as host rock, such as Opalinus Clay (OPA).

This Ph.D. aims at the investigation of the diffusion behavior of U(VI) and Am(III) down to ultra-trace concentrations ($<< 10^{-4}$ mol/m³) in OPA. In particular, potential differences in the diffusion properties of the two investigated actinide elements at ultra-trace concentrations compared to higher concentrations shall be explored.

As part of the investigations, four laboratory-scale diffusion experiments were conducted with samples of OPA, obtained from the Mont Terri underground laboratory (Switzerland) for 20 d, 36 d, 126 d, and 240 d, respectively. Within these experiments, cylindrical OPA samples (length: 10 mm, diameter: 6 mm) were contacted with synthetic pore water (ionic strength: 0.22 mol/L, pH: 7.2),[1] which was spiked with 1.8×10^{-11} to 3.2×10^{-9} mol/L of ^{233}U and 9.6×10^{-13} to 3.0×10^{-9} mol/L of ^{243}Am. After termination of the experiments, the OPA cylinders were segmented via abrasive peeling into thin layers of 20–400 µm. The obtained clay segments were analyzed for their ^{233}U and ^{243}Am content with accelerator mass spectrometry (AMS), one of the most sensitive analytical techniques for the determination of rare long-lived actinides in environmental samples.

The use of ultra-trace analysis demanded special attention toward actinide tracer background and cross-contamination. Such demands were met by the development of an optimized diffusion setup and sample processing procedure, comprising various preventive measures, in

particular the removal of the external surface of the OPA specimens´ sample holder prior to abrasive peeling.

Diffusion profiles of U(VI) and Am(III) were determined down to $\approx 10^{-9}$ mol/m³, which represents an improvement in detection sensitivity for U(VI) by five orders of magnitude compared to a previous study on the U(VI)–OPA system.[2] In the case of Am(III), it was the first time that diffusion profiles were determined in OPA. U(VI) showed typical diffusion profiles which were interpreted by applying Fick´s laws. The obtained effective diffusion coefficients were up to ten times higher than previously published.[2] One of the reasons was the present anisotropy of OPA, since diffusion was studied parallel to the clay bedding in the present study in contrast to perpendicular to the bedding in the previous study. No changes in the diffusion behavior of U(VI) through OPA over a concentration range of 10^{-3} mol/m³ to 10^{-9} mol/m³ were observed. The Am profiles were more complex, with a strongly sorbing section (i.e., short diffusion distance) and a "fast runner" section (i.e., long diffusion distance). Such two-part profiles were also observed in diffusion experiments with Eu(III) through OPA in a previous study.[3] Eu(III) is considered to behave analogously to Am(III).

µCT (X-ray microtomography) investigations of the OPA diffusion samples revealed the presence of micro-fractures 40–80 µm wide, potentially being responsible for the observation of an Am fraction with a higher diffusion length. Modelling of the two parts of the Am profile with a 1D pore diffusion model was possible hypothesizing the presence of two migrating Am species dominating the mobile phase. One was assumed to be the aqueous species $[Am(CO_3)]^+$. This cationic species undergoes strong retardation by negatively charged clay mineral surfaces, resulting in slow migration and causing the observed Am short diffusion profile. The other species is believed to be colloidal, present at approximately 10 times lower concentration compared to the aqueous species, featured by poor retention and faster migration through the micro-fractures in the OPA cylinder.

While presence and nature of the hypothesized colloids needs still to be investigated, the results of the present study provide relevant insight into the transport behavior of U(VI) and Am(III) in OPA over a wide range of concentrations down to ultra-trace levels.

This work was performed in the frame of the iCross project, with partial funding from the German Federal Ministry for Education and Research through the iCross collaborative project under grant agreement 02NUK 053 C, and from the Helmholtz association under grant agreement SO-093.

Zusammenfassung

Tongesteine werden als mögliches Wirtsgestein für die tiefengeologische Endlagerung hochradioaktiver Abfälle diskutiert. Das Wirtsgestein, die geotechnischen und technischen Barrieren sollen in der Lage sein, den Grundwasserzutritt in die Einlagerungskammern zu verzögern. Langzeitsicherheitsanalysen für ein Endlager für hochradioaktive Abfälle müssen das Eindringen von Grundwasser und die damit einhergehende Korrosion des Einlagerungsbehälters, sowie des Abfalls selbst und die daraus folgende Freisetzung von Radionukliden berücksichtigen. Der Transport freigesetzter Actinoide, wie zum Beispiel Uran (U) und Americium (Am), könnte dann durch Diffusion durch die geotechnische Barriere und das Wirtsgestein erfolgen. Unter den reduzierenden Bedingungen, die in einem Endlager vorherrschen, zeichnen sich Actinoide durch ihre geringe Löslichkeit und die starke Sorption an Tonmineraloberflächen aus. Die erwarteten sehr niedrigen Actinoidkonzentrationen stellen sowohl die Durchführung von Diffusionsversuchen als auch die anschließende Analytik vor besondere Herausforderungen. Das Diffusionsverhalten von U in Tongesteinen wurde bisher nicht unterhalb eines Gehalts von 10^{-4} mol/m³ Tongestein bestimmt. Für Am sind bis dato keine Diffusionsversuche in Tongesteinen, die als Wirtsgestein in Betracht gezogen werden (z.B. Opalinuston (OPA)), durchgeführt worden.

Die vorliegende Doktorarbeit befasst sich mit der Untersuchung des Diffusionsverhaltens von U(VI) und Am(III) in OPA bis hinab zum Ultraspurenkonzentrationsbereich ($<< 10^{-4}$ mol/m³). Insbesondere sollte untersucht werden, ob Unterschiede in den Diffusionseigenschaften der beiden untersuchten Actinoidelemente im Ultraspurenkonzentrationsbereich verglichen mit höheren Elementkonzentrationen vorliegen.

Im Rahmen der Studie wurden vier Diffusionsversuche mit Laufzeiten von jeweils 20, 36, 126 und 240 Tagen an OPA-Proben aus dem Untertagelabor in Mont Terri, Schweiz, durchgeführt. Hierfür wurden zylinderförmige OPA-Proben (Länge: 10 mm, Durchmesser: 6 mm) mit synthetischem Porenwasser (Ionenstärke: 0.22 mol/L, pH: 7.2)[1] kontaktiert, welches im Vorfeld der Experimente mit den Tracern ^{233}U und ^{243}Am versetzt wurde. Die Anfangskonzentrationen lagen für ^{233}U bei 1.8×10^{-11} bis 3.2×10^{-9} mol/L und für ^{243}Am bei 9.6×10^{-13} bis 3.0×10^{-9} mol/L. Nach Beendigung der Experimente wurden die OPA-Proben mittels schichtweisen Abtragens mit Sandpapier in Schichten von jeweils 20–400 µm Dicke segmentiert. Die Tonsegmente wurden auf ihre ^{233}U- und ^{243}Am-Gehalte mittels Beschleunigermassenspektrometrie (accelerator mass spectrometry (AMS)) analysiert. AMS

ist eine der empfindlichsten analytischen Methoden für die Bestimmung seltener, langlebiger Actinoide in Umweltproben.

Der Einsatz von Ultraspurenanalytik erforderte besondere Anforderungen mit Blick auf Hintergrund, verursacht durch die eingesetzten Actinoid-Tracer, und Querkontamination. Um diesen Anforderungen zu genügen, wurden das Diffusionssetup und das Verfahren der Probenbearbeitung optimiert. Das optimierte Verfahren beinhaltete mehrere vorbeugende Maßnahmen, insbesondere die Entfernung der äußeren Oberfläche des OPA-Probenhalters vor der Segmentierung mittels Abreibens mit Sandpapier.

Für U(VI) und Am(III) wurden Diffusionsprofile bis zu $\approx 10^{-9}$ mol/m³ bestimmt. Im Falle des U(VI) stellt dies, verglichen mit einer vorigen Studie zum U(VI)–OPA–System,[2] eine Verbesserung der Nachweisempfindlichkeit um fünf Größenordnungen dar. Uran zeigte für U(VI) typische Diffusionsprofile, die anhand der Fick´schen Gesetze beschreibbar waren. Die erhaltenen effektiven Diffusionskoeffizienten waren bis zu zehnmal höher als in einer vorigen Studie beschrieben.[2] Dies ist jedoch durch die Anisotropie der Diffusion erklärbar, da in der hiesigen Arbeit Diffusion parallel zur Tonschichtung untersucht wurde, während in der zitierten Studie Diffusion senkrecht zur Tonschichtung untersucht wurde. Im untersuchten Konzentrationsbereich von 10^{-3} mol/m³ bis 10^{-9} mol/m³ waren hinsichtlich des Diffusionsverhaltens von U(VI) keine Änderungen feststellbar. Im Fall von Am(III) wurden zum ersten Mal Diffusionsprofile in OPA ermittelt. Sie waren komplexer und zeichneten sich durch ein zweiteiliges Profil aus, bestehend aus einem stark sorbierenden Anteil mit schnell abfallenden ^{243}Am-Konzentrationen und einem „Schnellläufer“-Anteil mit moderatem Konzentrationsabfall und einer deutlich weitergehenden Migration. Ein solches zweiteiliges Profil wurde bereits im Rahmen von Diffusionsversuchen in OPA mit dem homologen Eu(III) beobachtet.[3]

µCT-Untersuchungen haben gezeigt, dass die zylinderförmigen OPA-Proben Mikrorisse mit einer Ausdehnung zwischen ungefähr 40 und 80 µm aufwiesen, welche die erhöhte Am-Mobilität erklären könnten. Die beiden Am-Profile wurden mittels eines 1D-Porendiffusionsmodels modelliert, unter der Annahme, dass zwei dominante Am-Spezies, mit unterschiedlicher Mobilität im Porenwasser vorliegen. Für den stark sorbierenden Anteil des Am-Profils wird die Dominanz der wässrigen Spezies $[Am(CO_3)]^+$ angenommen, die aufgrund starker Sorption an Tonmineraloberflächen zurückgehalten wird und folglich einem langsamen diffusiven Transport unterliegt. Für das „Schnellläufer“-Profil wird eine kolloidale Spezies vermutet, die in einer zehnfach niedrigeren Konzentration als die wässrige Spezies vorliegt und

sich durch schwache Rückhaltung und raschen Transport durch die Mikrorisse in der OPA-Probe auszeichnet. Während Anwesenheit und Art der vermuteten Kolloide noch zu zeigen sind, gewähren die Ergebnisse der durchgeführten Studie einen Einblick in das Migrationsverhalten von U(VI) und Am(III) über einen großen Konzentrationsbereich hinweg bis in den Ultraspurenbereich.

Die vorliegende Doktorarbeit wurde im Rahmen des Verbundprojekts iCross durchgeführt, unter Förderung durch das Bundesministerium für Bildung und Forschung (02NUK 053 C), sowie durch die Helmholtz-Gemeinschaft (SO-093).

Table of contents

Abstract vii

Zusammenfassung ix

1 Introduction 1

1.1 Motivation 1

1.2 Objectives 4

2 Clay minerals and natural clay rock 6

2.1 Characteristics of clay rock and clay minerals 6

2.1.1 Structure of clay minerals 7

2.1.2 Clay mineral particles 10

2.1.3 Basal and edge surface properties 12

2.1.4 Porous structure of clay rock 14

2.2 The natural clay rock Opalinus Clay (OPA) 15

3 Diffusive transport of radionuclides 18

3.1 Theoretical background of molecular diffusion 18

3.2 Diffusion of radionuclides through clay materials 19

3.2.1 Influence of radionuclide speciation and accessible porosity 20

3.2.2 Influence of clay properties on diffusion 25

3.3 Comparison of diffusion setups 26

3.3.1 Through-diffusion method 27

3.3.2 Radial diffusion method 29

3.3.3 Planar-source diffusion method 30

3.3.4 In-diffusion method 32

3.3.5 Summary 34

4 Accelerator Mass Spectrometry (AMS) 35

4.1 Introduction 35
4.2 Working principle 36
4.2.1 Cs sputter negative ion source 36
4.2.2 Low-energy injection system 38
4.2.3 Tandem accelerator 39
4.2.4 High-energy analyzing system & particle detector 40
4.3 Principle of measurement and data evaluation 41
4.3.1 Tuning and calibration of beam 41
4.3.2 Internal standardization 42
4.3.3 Background 43
4.3.4 Measurement procedure 43
5 Materials and methods 46
5.1 Chemicals and actinide tracers 46
5.2 Opalinus Clay (BLT-14) 47
5.3 Synthetic pore water 48
5.4 pH measurements 49
5.5 E_h measurements 49
5.6 Experimental details on diffusion experiments 49
5.6.1 Diffusion reservoir and diffusion sample holder 49
5.6.2 Equipment sorption test 52
5.6.3 Diffusion experiments 53
5.6.4 Abrasive peeling 54
5.6.5 Desorption 58
5.7 Inductively coupled plasma–mass spectrometry (ICP–MS) 58
5.7.1 Basic principle 58
5.7.2 ICP–MS analyses in this study 60
5.8 Ion chromatography (IC) 61

5.9 Dissolved inorganic carbon determination (DIC) 61
5.10 AMS sample preparation 61
5.11 X-ray microtomography (µCT) 62
5.12 Modeling software 63
5.12.1 Solubility and speciation calculations with PHREEQC 63
5.12.2 Modelling of diffusion profiles with COMSOL Multiphysics® 64

6 Development of diffusion experiments at ultra-trace actinide levels 66

6.1 Estimation of laboratory background 66
6.2 Diffusion experiment I (126 d) 66
6.3 Diffusion experiment II (240 d) 68
6.3.1 Clean laboratory and glove bags 69
6.3.2 Removal of external surface of sample holder 69
6.3.3 Profile samples including the investigation of potential rim mobility 71
6.4 Diffusion experiments III (20 d) and IV (36 d) 74

7 Results and discussion 76

7.1 Results on minimization of cross-contamination effects and ultra-trace background corrections 76
7.1.1 Laboratory background prior to the experiment 76
7.1.2 Potential airborne contamination due to abrasive peeling 77
7.1.3 Contamination on external surface of sample holder 78
7.1.4 Discussion of sources of background and cross-contamination 79
7.1.5 Low AMS count rates of internal standards 80
7.1.6 Concentration corrections in diffusion experiment I (126 d) 82
7.2 Speciation of U(VI) and Am(III) in OPA pore water 84
7.3 Scoping calculations of U(VI) and Am(III) diffusion profiles in OPA 86
7.4 Determination of tracer sorption onto equipment components 88

7.5 Decreased dissolved inorganic carbon inventory due to degassing of CO_2 88
7.6 U(VI) and Am(III) diffusion profiles after 126 d (experiment I) 89
7.6.1 Characterization of the reservoir solution 89
7.6.2 Discussion of the U(VI) and Am(III) diffusion profile 90
7.7 U(VI) and Am(III) diffusion profiles after 240 d (experiment II) 94
7.7.1 Characterization of the reservoir solution 94
7.7.2 Discussion of the U(VI) and Am(III) diffusion profile 95
7.8 U(VI) an Am(III) diffusion profiles after 20 d and 36 d (experiments III and IV) ... 99
7.8.1 Characterization of the reservoir solution 99
7.8.2 Discussion of the U(VI) and Am(III) diffusion profiles 101
7.9 Hypothesis for the development of an Am(III) fast-diffusing species profile 106
7.10 Summary and comprehensive interpretation of diffusion profiles 108

8 Conclusions and outlook 111

9 References 113

Appendix 123

Appendix A 123
Appendix B 126

List of figures

Fig. 1 Time-dependent radiotoxicity of spent nuclear fuel expressed in dose per mass of heavy metal [Sv/t SM]. SP: fission products, Pu: plutonium, MA: minor actinides, U nat: natural uranium, S: overall radiotoxicity as function of time (adopted from Gompper *et al.* (2010)[6]). 3

Fig. 2 Orientation of clay mineral particles during sedimentation (A: "House of cards" structure) and after compaction (B: Layered structure) (adopted from Van Loon *et al.* (2004)[22])…… 7

Fig. 3 Illustration of $M_{tet}O_4$ units forming a tetrahedral clay mineral sheet from top and side view (adopted from Schulze (2004)[24]). 7

Fig. 4 Illustration of $M_{oct}(O,OH)_6$ units forming an octahedral clay mineral sheet from top and side view (adopted from Schulze (2004)[24]). 8

Fig. 5 Illustration of 1:1 type clay mineral, consisting of one tetrahedral and one octahedral sheet from side view. For better visibility, metal cations were omitted from the illustration (adopted from Schulze (2004)[24]). 8

Fig. 6 Illustration of 2:1-type clay mineral, consisting of two tetrahedral sheets and one octahedral sheet from side view. For better visibility, metal cations were omitted from the illustration (adopted from Schulze (2004)[24]). 9

Fig. 7 Illustration of a smectite particle structure (adopted from Tournassat *et al.* (2015)[23])….. 10

Fig. 8 Unit layer structures of clay mineral groups. A: Muscovite-Illite, B: Smectite, C: Kaolinite-Serpentinite, D: Chlorite (adopted from Schulze (2004)[24]). 12

Fig. 9 The concept of the electrical double layer (Stern model) is applied to the interaction of charged solutes with clay surfaces. Hydration shells of ions in the diffuse layer were omitted for better visibility. 14

Fig. 10 Through-diffusion setup for the study of $^{233}U(VI)$ diffusion through OPA (adopted from Joseph *et al.* (2013)[2]). 28

Fig. 11 Evolution of diffusive flux and total diffused tracer mass as function of time in the source reservoir of a through-diffusion experiment (adopted from Van Loon *et al.* (2004)[57])….. 28

Fig. 12 Radial diffusion setup for the study of $^{22}Na^+$ and $^{36}Cl^-$ diffusion through OPA (adopted from Van Loon *et al*. (2004)[22]). Red arrows indicate the direction of diffusion, as well as the orientation of the bedding. 30

Fig. 13 Planar-source diffusion setup for the study of ^{60}Co(II) and ^{152}Eu(III) in FEBEX bentonite (adopted from García-Gutiérrez *et al.* (2011)[62]). 31

Fig. 14 Symmetrical diffusion profile of Eu(III) in FEBEX bentonite obtained via planar-source method. Positive and negative distances represent spatial Eu(III) distributions in the right and left clay tablet, respectively (adopted from García-Gutiérrez *et al.* (2011)[62]). 32

Fig. 15 Experimental setup for in-diffusion experiment (adopted from Van Loon *et al.* (2014)[46])… 33

Fig. 16 Overview of the AMS beamline at VERA (adopted from Winkler *et al.* (2015)[72])…… 36

Fig. 17 Pictures of aluminum sample cathode (left) and sample wheel holding up to 40 sample cathodes (right). 37

Fig. 18 Drawing of a Cs sputter negative ion source suitable for AMS (adopted from Vogel (2013)[77])… 38

Fig. 19 Pulse plot for detection of energy signals for incoming $^{243}Am^{3+}$. Pulse width on the y-axis and pulse height on the x-axis. Signals of $^{243}Am^{3+}$ are shown in the red box, counting events rom cations with lower *m* and *q* in orange box, and signals from the pulser in the green box……..... 41

Fig. 20 Location of borehole BLT-14 at the Mont Terri URL (adopted from Gräsele and Plischke (2007)[84]). 47

Fig. 21 Piece of OPA bore core BLT-14, red arrow indicating the orientation of bedding…... 48

Fig. 22 **a)** Drawing of diffusion reservoir with components: vessel (1), lid (2), cross with rails (3), sample holder for cylindrical OPA samples (4), **b)** picture of diffusion reservoir, during the diffusion experiment, the lid was wrapped with parafilm for reduction of pore water loss, **c)** drawing of sample holder for cylindrical OPA samples, **d)** technical drawing of sample holder……..... 51

Fig. 23 **a)** Cylindrical OPA sample, **b)** sample glued to Zinsser vial cap, **c)** sample immersed into epoxy resin inside PMMA sample holder, **d)** embedded sample in PMMA sample holder. 52

Fig. 24 Illustration of diffusion reservoir of experiments I (126 d) and II (240 d), with two clay samples partially immersed into the pore water solution, spiked with the diffusing tracers ^{233}U(VI) and ^{243}Am(III). 54

Fig. 25 **a)** PMMA sample holder with embedded OPA sample; PMMA cylinder was glued on top as support, **b)** bench vise and small handsaw, **c)** PMMA sample holder with embedded OPA sample after sawing. 55
Fig. 26 Abrasive peeling setup with its components: (1) collet, (2) carriage, (3) abrasive paper, (4) support, (5) quick-release, (6) micrometer. 56
Fig. 27 Drawing of carriage and support of the abrasive peeling setup. 56
Fig. 28 SiC paper sheets and abraded clay powders stored in centrifuge tubes. 57
Fig. 29 Principle setup of a quadrupole ICP–MS device (adopted from Linge *et al.* (2009)[90]). 59
Fig. 30 AMS sample press with sample cathode (highlighted with orange circle). 62
Fig. 31 Glove bag, equipped with handsaw, vise, and KODAN ® tissues. 69
Fig. 32 a) Top view of the clay cylinder embedded into PMMA sample holder with external surface (orange dashed lines), b) illustration of PMMA sample holder; external surface was abraded to a depth of approximately 100 µm at three different heights relative to the proximal sample side: 0–2 mm (purple dashed lines); 2–8 mm (light blue dashed lines); 10–18 mm (orange dashed lines). 70
Fig. 33 Illustration of abrasion and drilling of clay diffusion sample II after removal of the external surface of the sample holder, shown as dashed orange lines; **a)** abrasion of three successive segments, **b)** drilling of clay cylinder core region (diameter: 4.2 mm, length: 1373 µm, red segment), **c)** abrasion of rim region in five separate segments; segments 1 and 3 indicated in purple, **d)** drilling of clay cylinder core region (diameter: 2.5 mm, length: 933 µm, light blue segment), **e)** abrasion of rim region in four separate segments; segments 1 and 4 indicated in purple, **f)** abrasion of the remaining sample. 72
Fig. 34 Overview of sampling methods and positions in clay diffusion sample II; abraded full segments (green), drilled core segments (light blue & red), and abraded rim segments (dark blue and purple). External surface of sample holder, abraded prior to the segmentation of the clay diffusion sample is indicated as dashed orange lines. 72
Fig. 35 ^{233}U and ^{243}Am recovered from external surface of diffusion sample holder at three different positions: sampling was performed at heights of 0–2, 2–10, and 10–18 mm, highlighted as purple, light blue, and orange dotted lines, respectively. 79
Fig. 36 Diffusion profiles of **a)** ^{233}U and **b)** ^{243}Am in OPA after 126 d of diffusion. Predicted profiles are shown as dashed lines, experimentally obtained data points as grey error bars. Green and red error bars represent the profiles of ^{233}U and ^{243}Am, respectively, after correction for excess tracer previously sorbed onto the external surface of the sample holder. 83

Fig. 37 Calculated speciation of U(VI) as function of pH in synthetic OPA pore water (Tab. 9). Only species > 5 % are shown. For pH 7–8, DIC concentrations were assumed to be constant. For pH ≥ 8, depletion of CO_3^{2-} due to the precipitation of calcite was taken into account….. 85

Fig. 38 Calculated speciation of Am(III) as function of pH in synthetic OPA pore water (**Tab. 9**). Only species > 5 % are shown. 85

Fig. 39 Simulated diffusion profiles of **a)** U(VI) and **b)** Am(III) in cylindrical OPA sample with a diameter of 6 mm, after 120, 240, and 480 d of diffusion. LODs of ICP–MS and AMS are indicated with blue and brown dashed lines, respectively. 87

Fig. 40 Evolution of ^{233}U and ^{243}Am concentrations in PMMA reservoir containing OPA pore water.. 88

Fig. 41 Tracer concentrations in clay layers in mol of tracer per m³ of OPA after 126 d of diffusion, determined with AMS as function of distance; corresponding background levels are indicated as shaded dark cyan and purple areas. Predicted, experimentally obtained, and modelled diffusion profiles of **a)** ^{233}U and **b)** ^{243}Am. 93

Fig. 42 Experimental and modelled diffusion profiles of Eu(III) in OPA after 200 d of diffusion (adopted from PSI annual report 2019).[3] 94

Fig. 43 Diffusion profile of ^{233}U in OPA after 240 d of diffusion (represented as green error bars)…… 96

Fig. 44 Diffusion profile of ^{243}Am in OPA after 240 d of diffusion (represented as red error bars)…… 97

Fig. 45 Experimentally obtained diffusion profiles of ^{233}U after **a)** 20 d and **b)** after 36 d…… 102

Fig. 46 Experimentally obtained diffusion profiles of ^{243}Am after **a)** 20 d and **b)** after 36 d…… 104

Fig. 47 Experimentally obtained diffusion profiles of ^{243}Am after 36 d. The fast-diffusing species profile was fitted with K_d = 0.2 m³/kg and $D_e = 2 \times 10^{-11}$ m²/s, obtained after 240 d of diffusion. The fit is shown as black line. 105

Fig. 48 **a)** OPA cylinder contacted for 300 d with synthetic pore water; µCT scan at approximately 5 mm height, as indicated in yellow. Fracture highlighted with arrow: almost 6 mm long and 80 µm wide; **b)** 3D structure of OPA cylinder after segmentation. Fractures are represented as black areas, bulk clay matrix is highlighted in light red. 107

Fig. 49 Raw, unsaturated piece of OPA, mounted on a µCT sample holder (left); Exemplary CT image (right). 108

List of tables

Tab. 1 Overview of clay mineral groups and one respective clay mineral representative and their corresponding formula.[25] 9

Tab. 2 Overview of clay mineral groups and examples of representative clay minerals and their properties.[23,24] 11

Tab. 3 Range of mineralogical compositions of the shaly and sandy facies of OPA.[13] 16

Tab. 4 Selected parameter values for D_e and K_d of HTO, Cl^-, and I^- in OPA (bedding ⊥), obtained by diffusion and batch sorption experiments, reported by Van Loon *et al.* (2003) for pH = 7.6, I = 0.39 mol/L, and p = 5 MPa.[44] 20

Tab. 5 Parameter values for D_e, K_d, and D_a of selected mono- and divalent cations in clay materials, obtained from diffusion and/or batch sorption experiments. 23

Tab. 6 Charge and effective charge of cationic actinide species.[52] 24

Tab. 7 Parameter values D_e, K_d, D_a of selected actinide nuclides in clay materials, obtained by diffusion and/or batch sorption experiments, and their corresponding dominant aqueous species (dominant species account for ≥ 50 % of all occurring species in the studied system)…… 25

Tab. 8 Chemicals used in this work. 46

Tab. 9 Composition, pH, and I of synthetic OPA pore water at 25 °C according to Gimmi *et al.* (2014).[1] 49

Tab. 10 Model parameters and corresponding values for the simulation of the diffusion of U(VI) and Am(III) through OPA using COMSOL Multiphysics® (version 5.6) with a 1D pore diffusion model. 64

Tab. 11 Input parameter values for the modelling of the experimentally obtained second part of the Am(III) profiles, assuming water diffusion of Am(III) through fractured OPA, using a 1D pore diffusion model in COMSOL Multiphysics® (version 5.6). 65

Tab. 12 Procedural blanks and calibration samples from diffusion experiment I (126 d) for AMS analysis; thickness of each layer Δx_i [µm]. All segments were abraded with abrasive paper P220……. 67

Tab. 13 Clay diffusion samples from diffusion experiment I (126 d), selected for AMS analysis: the distance within the cylindrical clay sample before ($x_{i,\ \mathrm{before}}$) and after ($x_{i,\ \mathrm{after}}$) the respective abrasion step [µm]; sample 1 (9088 µm) represents the distal side of the clay cylinder and sample 10 (0 µm) the proximal side which was immersed into the diffusion reservoir solution; thickness of each layer (Δx_i) [µm]; sample position is represented as

($x_{i,\ before} - 0.5\Delta x_i)\pm\Delta x_i$ [µm]; abrasive paper grit number used for abrasion of corresponding layer…….....68

Tab. 14 Procedural blanks and calibration samples from diffusion experiment II (240 d) for AMS analysis; thickness of each layer Δx_i [µm]. All segments were abraded with abrasive paper P220…….....71

Tab. 15 Clay diffusion samples from diffusion experiment II (240 d) selected for AMS analysis: thickness of each layer (Δx_i) [µm]; the distance within the cylindrical clay sample before ($x_{i,\ before}$) and after ($x_{i,\ after}$) the respective abrasion step [µm]; sample 11 represents the distal side of the clay cylinder and sample 30 represents the proximal side, which was immersed into the diffusion reservoir solution; sample position indicated as ($x_{i,\ before} - 0.5\Delta x_i)\pm\Delta x_i$ [µm]…….....73

Tab. 16 Procedural blanks and calibration samples from diffusion experiment III (20 d) & IV (36 d) for AMS analysis; thickness of each layer Δx_i [µm]. All segments were abraded with abrasive paper P220. 74

Tab. 17 Clay diffusion samples from diffusion experiment III (20 d), selected for AMS analysis: thickness of each layer (Δx_i) [µm]; the distance within the cylindrical clay sample before ($x_{i,\ before}$) and after ($x_{i,\ after}$) the respective abrasion step [µm]; sample 31 represents the distal side of the clay cylinder and sample 37 represents the proximal side, which was immersed into the diffusion reservoir solution; sample position as ($x_{i,\ before} - 0.5\Delta x_i)\pm\Delta x_i$ [µm]. 75

Tab. 18 Clay diffusion samples from diffusion experiment IV (36 d), selected for AMS analysis: thickness of each layer (Δx_i) [µm]; the distance within the cylindrical clay sample before ($x_{i,\ before}$) and after ($x_{i,\ after}$) the respective abrasion step [µm]; sample 38 represents the distal side of the clay cylinder and sample 45 represents the proximal side, which was immersed into the diffusion reservoir solution; sample position as ($x_{i,\ before} - 0.5\Delta x_i)\pm\Delta x_i$ [µm]. 75

Tab. 19 Count rates of ^{233}U, ^{237}Np, ^{243}Am, and ^{248}Cm [cts/s] in glovebox and preparatory box background samples. Each ctr was determined as average of four samples. 77

Tab. 20 Count rates of ^{233}U, ^{243}Am, and internal standard ^{248}Cm [cts/s] in blank samples (B-1 to B-5), diffusion samples (DS-1 to DS-10), and calibration samples (Cal-1 to Cal-3), and corresponding tracer concentrations [mol/m³]; indicated concentrations in diffusion and calibration samples are blank and CIY corrected and normalized to count rates of internal tracer ^{248}Cm…….....81

Tab. 21 Calculated solubilities, dominant aquatic species of U(VI) and Am(III) and their respective fractions in OPA pore water in equilibrium with their respective solid phases.....84

Tab. 22 DIC concentrations in diffusion reservoir solution of diffusion experiments III (20 d) & IV (36 d) during conditioning (Pore water$_{cond}$ / (mol/L)) and during diffusion experiment (Pore water$_{diff}$ / (mol/L)). 89

Tab. 23 Diffusion experiment I (126 d): pore water composition in diffusion reservoir solution, I_t and pH during conditioning (Pore water$_{cond}$ / (mol/L)) and diffusion experiment (Pore water$_{diff}$ / (mol/L)). 90

Tab. 24 Dominant aquatic species of U(VI) and Am(III) in OPA pore water during diffusion experiment I (126 d) at the time of sampling. 90

Tab. 25 Parameter values for D_e and K_d for ^{233}U and ^{243}Am obtained from diffusion experiment I (126 d); comparison with parameters available from literature. 94

Tab. 26 Diffusion experiment II (240 d): pore water composition in diffusion reservoir solution, I_t and pH during diffusion experiment (Pore water$_{diff}$ / (mol/L)). 95

Tab. 27 Dominant aquatic species of U(VI) and Am(III) in OPA pore water during diffusion experiment II (240 d) at the time of sampling. For comparability, also compositions, aqueous speciations after 0 d and 126 d of diffusion are also shown. 95

Tab. 28 Parameter values for D_e and K_d for ^{233}U(VI) and ^{243}Am(III) obtained from diffusion experiment II (240 d) of diffusion; comparison with parameters available from literature. 98

Tab. 29 Diffusion experiments III (20 d) & IV (36 d): pore water composition in diffusion reservoir solution, I_t, pH, E_h, and oxygen concentration ([O_2]/ ppm) in glovebox during conditioning (Pore water$_{cond}$ / (mol/L)) and diffusion experiment (Pore water$_{diff}$ / (mol/L)). 100

Tab. 30 Dominant aquatic species of U(VI) and Am(III) in OPA pore water during diffusion experiments III (20 d) and IV (36 d) at the time of sampling. 101

Tab. 31 Parameter values for D_e and K_d for ^{233}U(VI) and ^{243}Am(III) obtained from diffusion experiments III & IV after 20 & 36 d of diffusion, respectively. 103

Tab. 32 Parameter values for D_e and K_d for ^{233}U(VI) obtained from diffusion experiments I, II, III, and IV after 126, 240, 20, and 36 d of diffusion, respectively; comparison with parameter values available from literature. 109

Tab. 33 Parameter values for D_e, D_a, and K_d for the profile of the slow-diffusing ^{243}Am(III) species obtained from diffusion experiment I, II, and IV after 126, 240, and 36 d of diffusion, respectively; comparison with parameters available from literature. 109

Tab. 34 Parameter values for D_e, K_d for profile of the fast-diffusing ^{243}Am(III) species obtained from diffusion experiment I and II after 126 and 240 d of diffusion, respectively. 110

Tab. A1 Diffusion experiment II (240 d): Count rates of ^{233}U, ^{243}Am, and internal standards ^{236}U and ^{248}Cm [cts/s] in diffusion samples (DS-11 to DS-24, as well as core and rim segments), calibration samples (Cal-4 to Cal-6), and blank samples (Blank 6 to Blank 9); corresponding tracer concentrations [mol/m³]; concentrations in diffusion and calibration samples are blank and CIY corrected and normalized to count rates of internal tracers ^{236}U and ^{248}Cm. 123

Tab. A2 Diffusion experiment III (20 d): Count rates of ^{233}U, ^{243}Am, and internal standards ^{236}U and ^{248}Cm [cts/s] in diffusion samples (DS-25 to DS-31) calibration sample (Cal-7), and blank samples (Blank 10, 12, and 13); corresponding tracer concentrations [mol/m³]; indicated concentrations in diffusion and calibration samples are blank and CIY corrected and normalized to count rates of internal tracers ^{236}U and ^{248}Cm..... 124

Tab. A3 Diffusion experiment IV (36 d): Count rates of ^{233}U, ^{243}Am, and internal standards ^{236}U and ^{248}Cm [cts/s] in diffusion samples (DS-32 to DS-39) and corresponding tracer concentrations [mol/m³]; indicated concentrations in diffusion and calibration samples are blank and CIY corrected and normalized to count rates of internal tracers ^{236}U and ^{248}Cm. 125

Tab. B1 Actinide tracer stock solutions: concentrations, matrices, and isotopic compositions of the of ^{233}U, ^{236}U, ^{243}Am, and ^{248}Cm solutions. 126

Tab. B2 Concentrations of ^{233}U, ^{236}U, ^{243}Am, and ^{248}Cm in diluted solutions, given in mol/L…… 126

1 Introduction

1.1 Motivation

The use of nuclear technology is accompanied by the production of radioactive waste of different types. Low- and intermediate-level waste is, for instance, composed of operational waste from nuclear power plants or the debris from the decommissioning of nuclear facilities. In countries with nuclear power plants, this waste type constitutes about 95 % of the total radioactive waste volume, but only about 1 % of its radioactivity. High-level waste (HLW) mainly consists of spent fuel assemblies from nuclear reactors and vitrified waste products from high-level liquid waste from reprocessing plants. HLW represents only about 1 % of the total volume of nuclear waste, but is responsible for about 99 % of its radioactivity in those countries.[4]

According to worldwide scientific consensus, HLW should be disposed in a deep geological repository (DGR), which is capable of isolating radionuclides at a suitable place and thereby excludes them from the biosphere over time periods of up to one million years, as required by the German site selection act.[5] Such time period allows for long-lived radionuclides contained in HLW, such as ^{237}Np ($t_{1/2} = 2.1 \times 10^6$ a) and ^{129}I ($t_{1/2} = 1.6 \times 10^7$ a), to decay to radiotoxicity levels encountered in natural uranium deposits (**Fig. 1**).[6]

In general, a DGR is featured by a multi-barrier system,[7] consisting of:

a) a technical barrier, comprising the waste form, such as (spent nuclear fuel) SNF, encapsulated by a metal container;
b) a geotechnical barrier, consisting of a backfill material such as bentonite clay or crushed rock salt, as proposed for a repository in rock salt. Such materials support the mechanical stability of the disposal rooms and minimize the release of radionuclides upon potential water ingress by strong retardation;
c) a geological barrier, which is, for instance, the host rock and an overlying lithology, called overburden.

As part of the geological barrier, three types of host rocks are currently under discussion, namely rock salt, crystalline and clay rock.

Salt formations are featured by low permeability and high plasticity, allowing for the tight containment of HLW after a certain time span of the early repository's post-closure phase. Furthermore, the high thermal conductivity supports the dissipation of the decay heat generated

inside the high-level waste products. Geological repositories for low- and intermediate-level radioactive waste in rock salt are in operation in Germany (Morsleben, Saxony-Anhalt) and in the United States ("Waste Isolation Pilot Plant", New Mexico). Rock salts are characterized by their low retention capability of radionuclides and their high water solubility. Furthermore, the saline solutions occurring upon water ingress are corrosive.

Crystalline rock (such as granite, gneiss, granodiorite or amphibolite) provides a high degree of mechanical stability and benefits from its low solubility. However, crystalline rock complexes consist of numerous fractures and fissures. In particular along these fractures, intruding ground water can facilitate the migration of radionuclides, released from the waste forms. For instance Finland and Sweden selected crystalline rocks as host rocks in the frame of their disposal concept (Olkiluoto, Finland, and Forsmark, Sweden, spent fuel repositories).[8] These multi-barrier systems in crystalline rocks are featured by a corrosion resistant copper-lined cast iron container, embedded in bentonitic backfill material in order to retard intruding groundwater.

Clay rock is characterized by high plasticity, swelling properties, and mesoporosity, which counteract fracture formation and delimit pollutant propagation to exclusively diffusive transport. A further advantage of clay rock is its retention capability toward many radionuclides, which sorb strongly onto the clay stratum. This is especially true for reducing conditions, as anticipated in the future repository. Concerning its suitability as a host rock for deep geological disposal of HLW, clay rock is subject to scientific investigations in many countries. For instance, France carries out research on the so-called Callovo-Oxfordian Clay (COx) in the Meuse/Haute-Marne underground research laboratory, located in the eastern part of the country. Switzerland is investigating the Opalinus Clay (OPA) in the frame of the Mont Terri underground laboratory. Diffusion is the predominant mechanism for radionuclide migration through the porous structure of clay rocks. For such migration processes, pH and redox conditions in the repository are of major relevance, since they govern the speciation of the radionuclides and, ultimately their mobility in clay rock.

Concerning the long-term safety of a DGR, knowledge on the radiotoxicity contribution of each radionuclide is of utmost importance. As shown in **Fig. 1**, short-lived fission products (e.g., ^{137}Cs and ^{90}Sr) reach radiotoxicity levels of naturally occurring uranium deposits already a few hundred years after discharge of the fuel from the reactor, whereas for long-lived Pu isotopes (e.g., ^{239}Pu) and long-lived isotopes of the minor actinides, mainly ^{243}Am, this level is reached only after 10^4 to 10^6 y.[6]

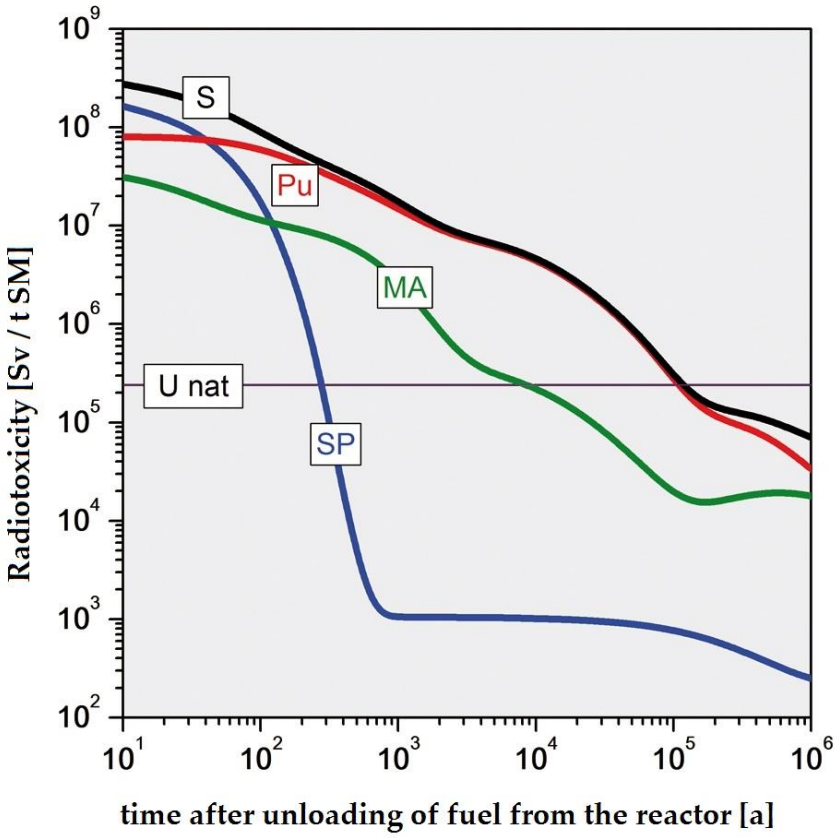

Fig. 1 Time-dependent radiotoxicity of spent nuclear fuel expressed in dose per mass of heavy metal [Sv/t SM]. SP: fission products, Pu: plutonium, MA: minor actinides, U nat: natural uranium, S: overall radiotoxicity as function of time (adopted from Gompper *et al.* (2010)[6]).

There is a strong interest in the environmental behavior of uranium (U), which is the main constituent of SNF, and of the minor actinides, such as Am, which contribute significantly to the long-term radiotoxicity of high-level nuclear waste. Note, although long-lived fission and activation products, such as ^{129}I and ^{36}Cl, are present in HLW in only very low amounts, they are rather mobile in the geosphere and are considered as dose-dominating radionuclides in most safety analysis calculations. Transuranium elements, such as Np, Pu, and Am mainly exist in the oxidation states +III and +IV under the reducing conditions of a DGR and are considered as rather immobile. For instance, in OPA, redox potentials of approximately −200 mV are expected. Respective aquatic actinide species normally exhibit low solubility and strong sorption onto clay mineral surfaces and are consequently featured by low mobility.

Diffusion of actinides has already been investigated under aerobic conditions for Np(V) in OPA[9] and under anaerobic conditions for U(VI) in both OPA[2] and bentonite clay.[10] Studies under reducing conditions have been performed for Np(IV), Pu(IV), and Am(III) in bentonite clay.[11,12] In the studies of Yamaguchi *et al.* (2007)[11] and Sawaguchi *et al.* (2013),[12] HCO_3^- was added as complexing agent, resulting in the formation of highly soluble actinide species and, in

this way, an increase of the aqueous actinide concentration. Furthermore, $S_2O_4^{2-}$ was added as reducing agent in order to induce and maintain a negative redox potential. However, the conditions established in these studies by the addition of complexing and reducing agents do not represent the conditions in the clay rock of a future HLW repository. For instance, in the work of Sawaguchi *et al.* (2013)[12] an aquatic carbonate concentration of $[CO_3^{2-}] = 0.3$ mol/L was used, while naturally occurring OPA pore water is featured by a much lower carbonate concentration ($[CO_3^{2-}] \approx 10^{-3}$ mol/L).[13] The analytical techniques employed in these studies — γ-spectrometry and liquid scintillation counting — allowed for detection limits of the studied actinides per clay sample volume not lower than approximately 10^{-4} mol/m³. Diffusion profiles in OPA with actinide concentrations below this level have not been investigated up to now. Furthermore, no experimentally determined transport parameter values for the diffusion of Am(III) in natural clay are available in literature. In order to experimentally examine diffusion profiles at ultra-trace levels, analytical constraints concerning detection sensitivity have to be overcome. One of the most sensitive analytical techniques for the determination of rare, long-lived actinides in natural samples is accelerator mass spectrometry (AMS). It allows for the determination of actinide nuclides down to quantities of 10^{-19} mol/sample without previous chemical separation from each other.[14,15] In clay matrices such as OPA, the AMS determination of actinide nuclides is possible down to approximately 10^{-11} mol/m³,[16] making it the analytical technique of choice for the exploration of actinide diffusion profiles at ultra-trace levels.

1.2 Objectives

Despite the expected limited release of actinides from the repository near-field upon water access and the resulting very low aqueous concentrations, it has to be examined if actinides present at ultra-trace levels may exhibit a different mobility compared to higher concentrations. The present study aims at studying the diffusion behavior of U and Am down to ultra-trace concentrations (amount of actinide per clay sample volume $<< 10^{-4}$ mol/m³) in the shaly facies of OPA. In particular, the diffusion behavior of U(VI) and Am(III) was investigated at ultra-trace concentrations and compared to the behavior at higher concentrations. By fitting the obtained diffusion profiles with a transport model, transport parameters (i.e., diffusion coefficients) and distribution coefficients (K_d values) were determined for U(VI) and Am(III). The quantification of ultra-trace concentration levels of U and Am in OPA was performed with AMS. In order to obtain reliable data of diffusion profiles at ultra-trace concentrations, particular attention was paid to the minimization of background and cross-contamination by the development of an optimized diffusion setup and sample processing method.

In the frame of the development of the diffusion setup, the laboratory (i.e., glovebox, exhaust hood) envisaged for the diffusion experiment was checked for background levels of the diffusing tracers U and Am prior to the diffusion experiments. Solubility calculations were carried out in order to estimate solubility limits and the dominant speciation of the diffusing tracers U(VI) and Am(III) in OPA pore water. Since trivalent actinides, such as Am(III), are prone to strong sorption onto equipment materials under neutral to alkaline conditions, while the fraction of hexavalent actinides undergoing sorption is much lower, an equipment sorption test was carried out. The aim of such test was to determine the necessary contact time to establish equilibrium between aqueous species and species sorbed onto the diffusion reservoir components. This would be the necessary equilibration time, before initiation of the clay diffusion experiment. Furthermore, for estimation of the expected diffusion distances and the resulting diffusion profiles of U(VI) and Am(III) in OPA, scoping calculations were carried out. The aim of the calculations was a) to determine dimensions of the clay samples and experimental durations suitable for diffusion experiments involving the determination of ultra-trace concentrations of the diffusing tracers, and, b) to assess which mass spectrometric techniques are required to determine tracer concentrations at different depths of the clay sample. In particular, it needed to be estimated, at which maximum diffusion distances the diffusing tracers would be still detectable with AMS.

The development of the sample processing method comprised multiple preventive measures with the aim of minimizing cross-contamination: a) removal of the external surface of the clay diffusion sample holder prior to abrasive peeling, b) segmentation of the clay diffusion sample in the direction of increasing tracer concentration, and, c) use of airtight glove bags for steps of the sample processing which involved the release of airborne particles (e.g., abrasive peeling).

2 Clay minerals and natural clay rock

2.1 Characteristics of clay rock and clay minerals

Clays are featured by specific chemical, physical, and mechanical properties which makes them suitable for their use as geological and geo-engineered barriers in a HLW repository. For instance, some clays are capable of swelling upon water contact, due to the presence of water absorbing interlayers. The swelling capacity as well as the plastic behavior of clays allow for the efficient sealing of fractures and, in this way, maintain the clay rock´s integrity. Such sealing characteristics result in a very low hydraulic conductivity (k_h [m/s] = 10^{-12}–10^{-13} m/s for FEBEX and MX-80 bentonite;[17,18] $k_h \leq 10^{-13}$ m/s for OPA and COx),[19,20] making clays almost impermeable for fluids via advective transport. Consequently, solute migration occurs mainly via diffusive transport and is rather slow. Such property is inherent for clay backfill materials, such as FEBEX and MX-80 bentonite, as well as for clay lithologies foreseen as host rocks for the final storage of HLW, such as OPA and COx. Furthermore, clays are known for their high sorption affinity toward a variety of organic and inorganic pollutants, resulting in strong retention of migrating radionuclides. In particular, cation retention can be very pronounced owing to the surface characteristics of clay minerals offering both areas of permanent negative charge for ion exchange binding and hydroxyl groups for surface complexation.

Natural clays are abundant consolidated or non-consolidated sedimentary rocks.[21] Clays and clay-stones considered as host rocks for HLW repositories formed during the cenozoic and mesozoic eras approximately 40 to 200 million years ago. Clay formation starts with the weathering of primary silicate rocks near the earth surface. Consecutive to the weathering process, sedimentary clay rocks are formed by sedimentation of clay particles in a “house-of-cards” structure (**Fig. 2**). With growing pressure, imposed by the overburden rocks and the resulting compaction, the clay particles re-arrange preferentially perpendicular relative to the direction of imposed lithological pressure, resulting in the distinct layered structure of clay formations (**Fig. 2**). Such preferential orientation of clay particles is called bedding and has an influence on the mobility of solutes by diffusive transport (see sub-chapter 3.2.2).

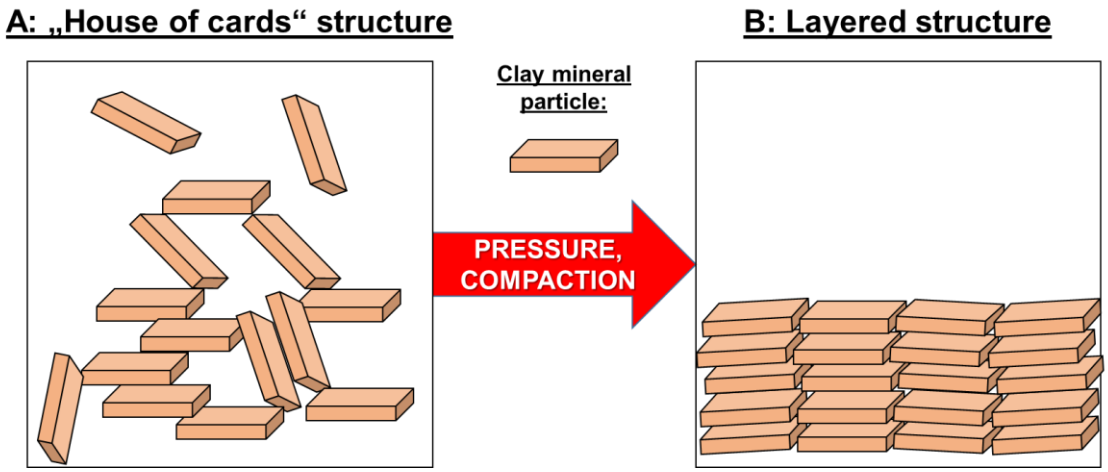

Fig. 2 Orientation of clay mineral particles during sedimentation (**A:** “House of cards” structure) and after compaction (**B:** Layered structure) (adopted from Van Loon *et al.* (2004)[22]).

2.1.1 Structure of clay minerals

Clay rocks primarily consist of mineral particles (< 20 µm) which are mainly composed of clay minerals (< 2 µm).[23] Clay minerals are aluminosilicates and, as a group of phyllosilicates, featured by the tendency to arrange themselves in layers. At the most basic level, clay minerals form two types of sheets: Multiple [$M_{tet}O_4$] tetrahedral units (M_{tet} = Si, Al) are corner-connected via shared basal oxygen (O_b) atoms, resulting in tetrahedral sheets with hexagonal cavities (**Fig. 3**). Octahedral sheets are formed, when multiple [$M_{oct}(O,OH)_6$] octahedral units (M_{oct} = Al, Mg, Fe) are edge-connected via shared octahedral oxygen (O_o) atoms (**Fig. 4**).

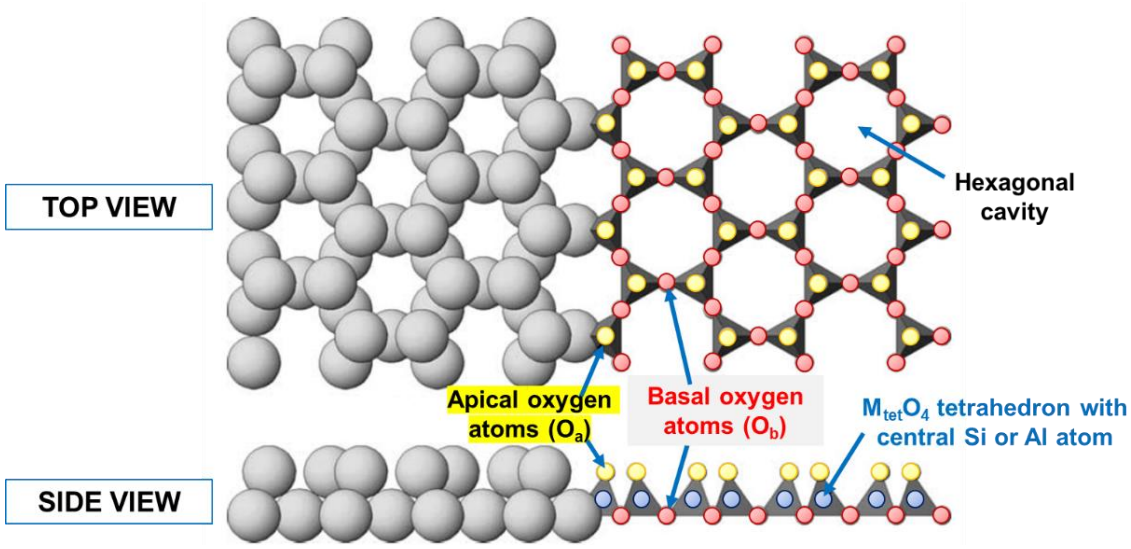

Fig. 3 Illustration of $M_{tet}O_4$ units forming a tetrahedral clay mineral sheet from top and side view (adopted from Schulze (2004)[24]).

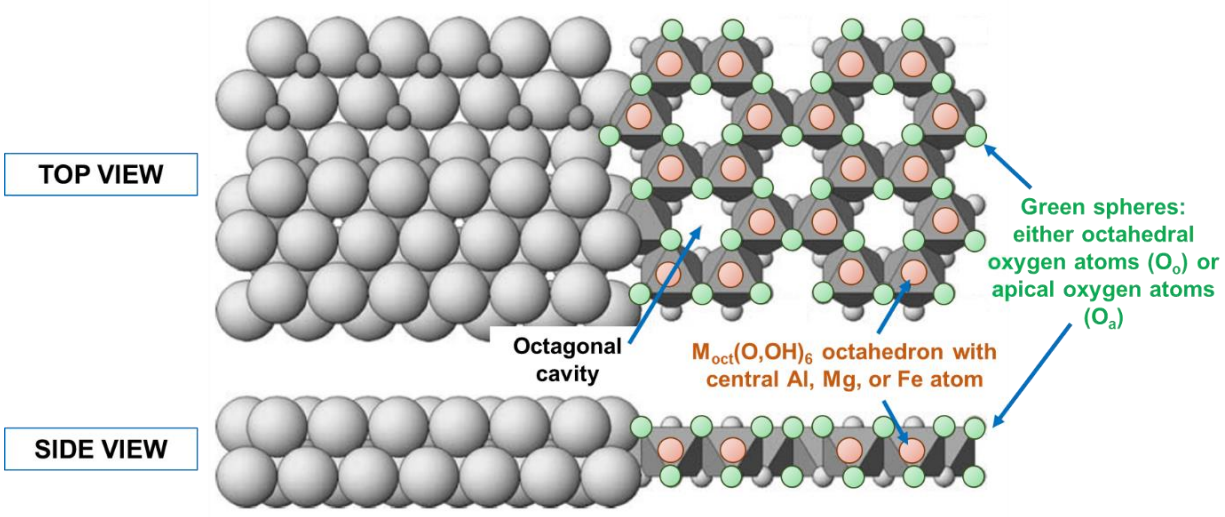

Fig. 4 Illustration of $M_{oct}(O,OH)_6$ units forming an octahedral clay mineral sheet from top and side view (adopted from Schulze (2004)[24]).

These two types of sheets form layered structures. There are two essential types of clay mineral layers: In a two-layer structure, one octahedral sheet is associated with one tetrahedral sheet, with a total layer thickness of ≈ 7 Å (**Fig. 5**). This layer type is also referred to as 1:1 or tetrahedral-octahedral (TO). In a three-layer structure, one octahedral sheet is sandwiched between two tetrahedral sheets (with a total layer thickness ≈ 9.5 Å of a non-swelled TOT alumosilicate). This is also referred to as 2:1 or tetrahedral-octahedral-tetrahedral (TOT) layer (**Fig. 6**). In both layer types, tetrahedral and octahedral units are linked to each other via shared oxygen atoms, which are called apical oxygen (O_a) atoms (**Fig. 5**, **Fig. 6**).

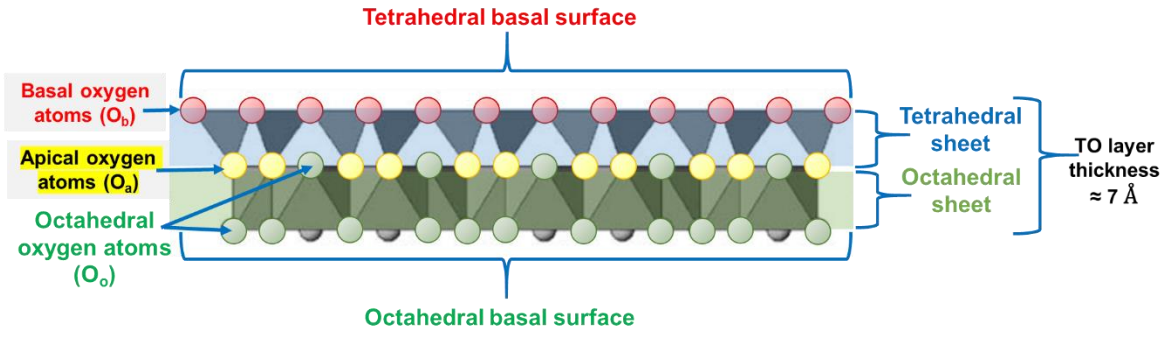

Fig. 5 Illustration of 1:1 type clay mineral, consisting of one tetrahedral and one octahedral sheet from side view. For better visibility, metal cations were omitted from the illustration (adopted from Schulze (2004)[24]).

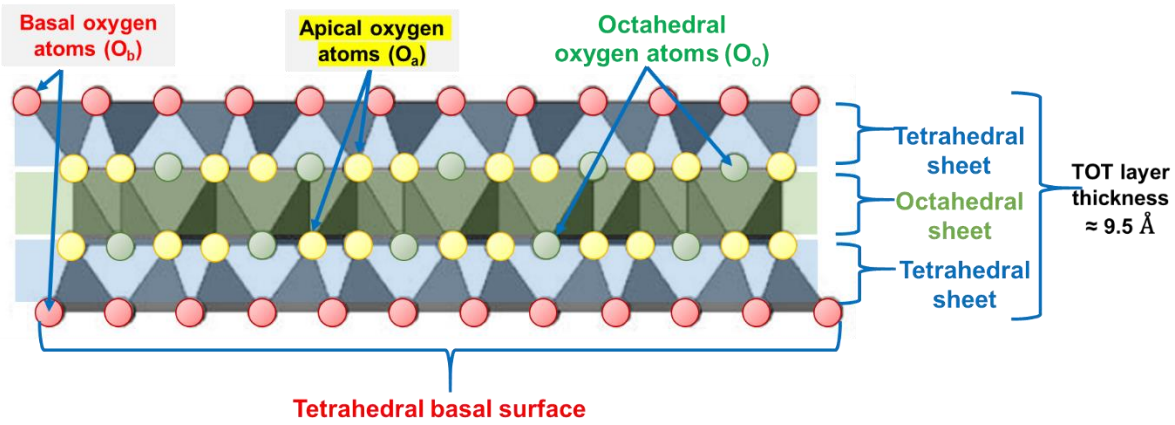

Fig. 6 Illustration of 2:1-type clay mineral, consisting of two tetrahedral sheets and one octahedral sheet from side view. For better visibility, metal cations were omitted from the illustration (adopted from Schulze (2004)[24]).

A sub-type of 2:1-clay minerals is featured by an additional octahedral sheet sandwiched between two TOT layers and is therefore referred to as 2:1:1-clay mineral layer. An important representative of this layer structure is the clay mineral group of chlorites. The described layer types can also be combined to form mixed-layer clay minerals. For instance, illite-smectite mixed layers are commonly found in natural clay rock such as OPA. An overview of important clay minerals and clay mineral groups and their corresponding formulas can be found in **Tab. 1**.

Tab. 1 Overview of clay mineral groups and one respective clay mineral representative and their corresponding formula.[25]

Clay mineral group	Clay mineral	Layer structure	Formula
Kaolinite-Serpentinite	Kaolinite	1:1	$Al_2Si_2O_5(OH)_4$
Muscovite-Illite	Illite	2:1	$K_{0.7}(H_3O)_{0.1}(Al,Fe^{III})_{1.7}(Mg,Fe^{II})_{0.3}(Al_{0.5}Si_{3.5}O_{10})(OH)_2$
Smectite	Montmorillonite	2:1	$(Na,Ca_{0.5})_{0.33}(Mg_{0.33}Al_{1.67})(Si_4O_{10})(OH)_2 \cdot n\ H_2O$
Chlorite	Clinochlore	2:1:1	$Mg_5Al(AlSi_3O_{10})(OH)_8$

The two large surfaces on either side of a clay mineral layer are called basal surfaces and have commonly maximum lengths between 50–100 nm in the case of illites and up to 1000 nm in the case of smectites (**Fig. 7**). In TO-layers, one basal surface is a siloxane surface, made of the shared O_b atoms of the connected tetrahedral units (**Fig. 5**), also referred to as tetrahedral basal surface. The other basal surface consists of mainly protonated shared O_o atoms of the linked octahedral units, called octahedral basal surface. In the case of TOT-layers, both basal surfaces

are tetrahedral basal surfaces (**Fig. 6**). Furthermore, the two small surfaces on either side of a clay mineral layer are the edge surfaces (**Fig. 7**). Both basal and edge surfaces play a key role in clay minerals' sorption affinity toward cations (see sub-chapters 2.1.2 and 2.1.3).

2.1.2 Clay mineral particles

Clay mineral layers can form bigger structures by stacking onto each other. The number of stacked layers per particle can range between 5 and 10 (e.g., illite) and several hundred (e.g., kaolinite). The space between the layers is called interlayer space and is occupied by water molecules only (i.e., hydrated interlayer) or by non-, partially, and fully hydrated cations. The kind of interlayer occupancy strongly depends on the degree of negative layer charge to be compensated and has a major impact on several physical and chemical properties of the clay mineral.

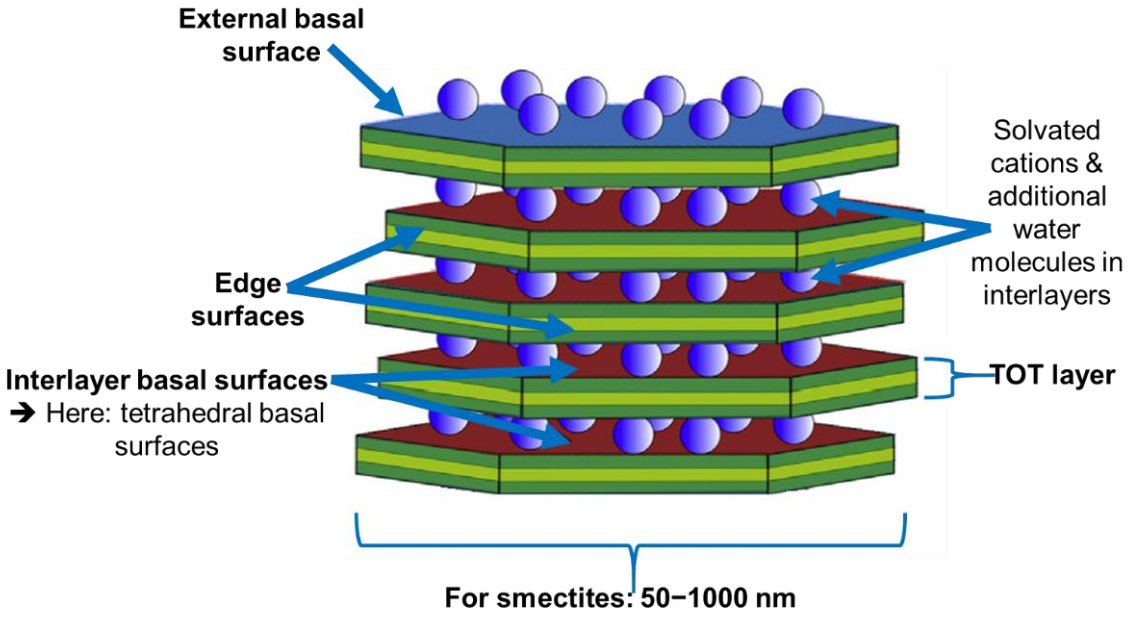

Fig. 7 Illustration of a smectite particle structure (adopted from Tournassat *et al.* (2015)[23]).

Clay mineral layers can be either charged or uncharged. For instance, most 2:1 type clay minerals bear a permanent negative charge, which is described with the layer charge density l_c [mol_c/mol], expressed as moles of charge/moles per clay mineral. For illites and smectites, such layer charge densities are 0.6–0.9 mol_c/mol and 0.2–0.6 mol_c/mol, respectively (**Tab. 2**). The negative layer charge arises from ionic substitutions in the tetrahedral (e.g., Si^{4+} vs. Al^{3+}) and octahedral sheets (e.g., Al^{3+} vs. Mg^{2+}) and is compensated usually by alkaline and alkaline earth metal cations, attached to external and interlayer basal surfaces (**Fig. 7**). For instance, due to its high l_c, the interlayers of illites contain non-hydrated cations for charge compensation

(e.g., K^+) and are featured by a small interlayer distance, referred to as collapsed interlayer (**Fig. 8A**). This causes the interlayers to be non-accessible for water molecules, which makes illites non-swelling clay minerals. Furthermore, the non-hydrated cations in these interlayers are bound via strong electrostatic forces and are, therefore, not readily exchangeable. This is reflected in a rather low cation exchange capacity (CEC) (**Tab. 2**), which is defined as milli-equivalents of exchangeable positive charge per 100 g of clay mineral [meq/100 g]. Conversely, clay minerals with low l_c, such as smectites (**Fig. 8B**), are featured by partially or fully-hydrated cations in the interlayer space. This results in a larger interlayer distance, allowing for the presence of additional water molecules, making them swelling clay minerals. The hydrated cations in the interlayers are only weakly bound and are readily exchangeable (high CEC, see **Tab. 2**). It shall be mentioned that not only cations in the interlayers contribute to a clay mineral´s CEC, but also those located at edge surfaces. Such edge surface charge is strongly pH-dependent (see sub-chapter 2.1.3). In contrast to TOT-clays, most TO-type clay minerals, such as kaolinite, have practically no permanent layer charge. In this case, clay mineral layers interact via van der Waals forces and hydrogen bonds between the O_b atoms of one TO-layer and H atoms bound to O_o atoms of the other TO layer. As a result of the empty interlayer space, kaolinite has a comparably small unit layer of 7.2 Å (**Fig. 8C**, **Tab. 2**). Another way of charge balance occurs in 2:1:1 clay minerals, such as chlorite. Here, an additional octahedral sheet between the two TOT-layers introduces positive charge due to the presence of Mg^{2+} (**Fig. 8D**).

Tab. 2 Overview of clay mineral groups and examples of representative clay minerals and their properties.[23,24]

Clay mineral group	l_c / (mol_c/mol)	Clay mineral	Unit layer / Å	CEC / (meq/100 g)
Kaolinite-Serpentinite	≈ 0	Kaolinite	7.2	1–10
Muscovite-Illite	0.6–0.9	Illite	10	10–40
Smectite	0.2–0.6	Montmorillonite	12.5–19	80–150
Chlorite	variable	Clinochlore	14	< 10

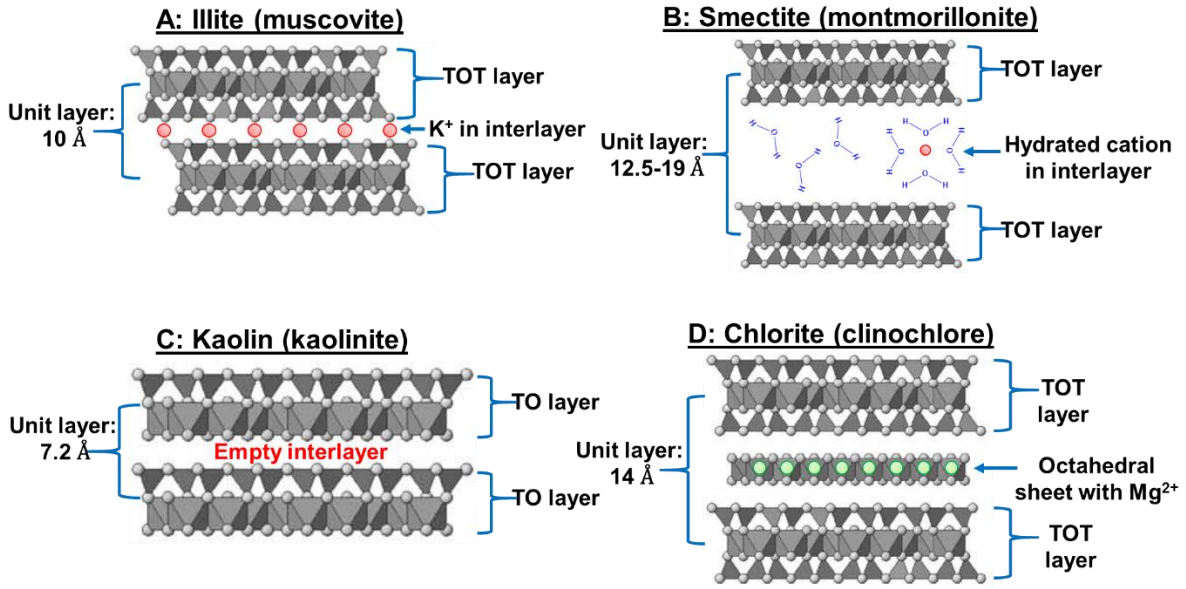

Fig. 8 Unit layer structures of clay mineral groups. **A:** Muscovite-Illite, **B:** Smectite, **C:** Kaolinite-Serpentinite, **D:** Chlorite (adopted from Schulze (2004)[24]).

2.1.3 Basal and edge surface properties

The physical and chemical properties of clay mineral basal and edge surfaces are of major relevance for the transport and retention of ionic solutes in the porous structures of clays. While anion sorption onto basal surfaces is rather weak due to repulsion by the negative surface charge, metal cations can sorb to basal surfaces via cation exchange. Depending on the metal´s effective charge and its speciation, metal retention can be considerable (see sub-chapter 3.2.1). As already described, the negative surface charge of 2:1-type clay minerals is balanced by alkaline and alkaline earth metal cations. Such negative surface charge is permanent and pH-independent, since the O_b atoms of the tetrahedral basal surfaces do not undergo protolysis. At external basal surfaces, metals can exchange for bound cations. Since such metals are always solvated, the exchanged cation does not interact with the clay mineral´s basal surface directly but via its hydration sphere, which is an electrostatically driven process. Therefore, cation exchange is also referred to as electrostatic surface complexation or outer-sphere complexation. Due to the permanent negative surface charge of clay mineral layers, cation exchange is practically pH-independent, but strongly dependent on the ionic strength (I [mol/L]) of the pore water. This is due to the fact that the competition between cations for sorption sites is more pronounced at higher I. The same trend is true for interlayer basal surfaces for swelling clay minerals (e.g., smectites), where the bound cations are easily exchangeable. However, metal sorption at interlayer basal surfaces cannot occur readily in non-swelling clay minerals, where the interlayer is occupied by strongly bound cations (e.g., K^+ in illites) or is non-accessible due

to the lack of permanent negative charge in 1:1-type clay minerals (e.g., empty interlayer in kaolinite), as shown in **Fig. 8C**.

The interaction between cations and clay mineral basal surfaces can be interpreted as an electrical double layer (EDL), based on the improved EDL concept proposed by Otto Stern in 1924. The permanent negative layer charge and the charge compensating cations at the basal surface form the so-called Stern layer, where cations are immobilized by electrostatically driven outer-sphere complexation. After the Stern layer, a diffuse layer follows, which contains both cations and anions, interacting with the basal surface via rather weak long-range electrostatic forces.[23] The ions in the diffuse layer are mobile and are able to migrate through the porous clay structure as well as the ions in the bulk water (see sub-chapter 3.2.1), while cations in the Stern layer are generally considered strongly bound (**Fig. 9**). It shall be noted that under specific conditions also strongly bound cations can be mobile and do diffuse, a process called surface diffusion. For instance, the surface diffusion of Cs^+ in illite was recently studied by Glaus *et al.* (2020).[26]

Clay mineral layers also have so-called edge surfaces (**Fig. 7, Fig. 9**), where the regular structure of the layer is interrupted. Edge surfaces account for the variable charge of a clay mineral and are strongly pH-dependent due to amphoteric functional groups (e.g., Si-OH). For the most part, metal sorption at edge surfaces occurs via inner-sphere surface complexation.

A special type of edge surface region called “frayed edge” is characterized by a widening of the regular interlayer space near the edge. This allows for the exchange of usually non-exchangeable cations, such as K^+, for other weakly-hydrated cations, such as Cs^+. Therefore, frayed edge sites are considered particularly relevant for Cs^+ sorption on illites.[27]

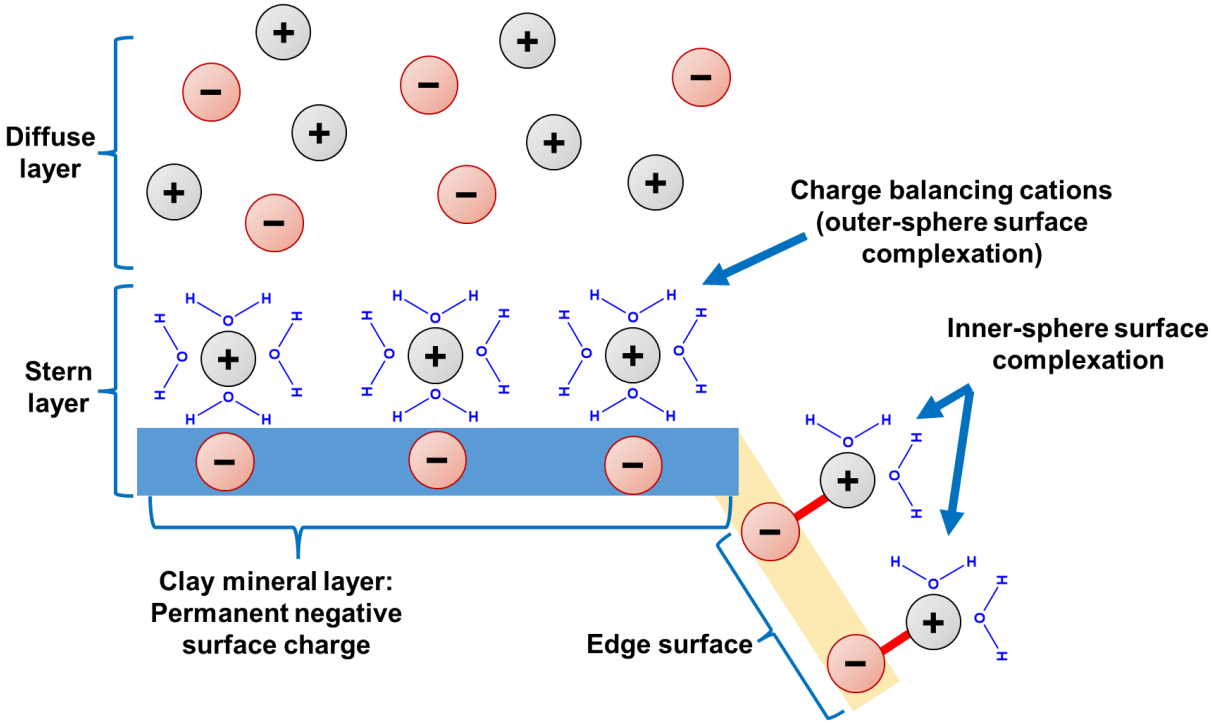

Fig. 9 The concept of the electrical double layer (Stern model) is applied to the interaction of charged solutes with clay surfaces. Hydration shells of ions in the diffuse layer were omitted for better visibility.

2.1.4 Porous structure of clay rock

Clay rocks are featured by a porous structure, comprising micro-pores, meso-pores, and macro-pores with pore diameters of < 2 nm, 2–50 nm, and > 50 nm, respectively.[28] The porous structure of the clay fraction consists mainly of the voids between adjacent clay mineral layers (i.e., interlayer space) with pore diameters ≤ 10 nm, and the clay mineral framework (clay layer stacks).[28] Although a major fraction of a clay matrix consists of clay minerals, natural clay rocks are heterogeneous in mineralogy. Medium and accessory constituents can be quartz (SiO_2), carbonate minerals (e.g., calcite ($CaCO_3$)), alkali feldspars ($(K,Na)AlSi_3O_8$), plagioclases ($(Na,Ca_{0.5})Al(Al_xSi_{3-x})O_8$), iron-bearing minerals, such as siderite ($FeCO_3$) and pyrite (FeS_2), and organic carbon, for instance in the form of humic materials.[13] Both clay minerals and medium and accessory constituents contribute to the porous structure by the formation of voids between mineral particles (i.e., interparticle space), and between aggregates of mineral particles (i.e., interaggregate space), which can have diameters of up to a few microns.[29] The proportion and distribution of the different clay rock constituting minerals have not only an impact on the different pore sizes (i.e., pore size distribution), but also on pore geometry and pore connectivity.[30]

The sum of pore spaces caused by the individual types of voids (V_{void} [m³]), normalized to the total volume of the porous material (V_{tot} [m³]) is defined as the clay material´s porosity ε [–]:

$$\varepsilon = \frac{V_{void}}{V_{tot}} \qquad \textbf{Eq. 1}$$

Clay porosity, in particular the effective porosity (ε_{eff}) accessible by diffusion, is of great importance for diffusive solute transport through the porous network. For cations and neutral solutes, in general, the complete pore space is available for diffusive transport ($\varepsilon_{eff} = \varepsilon$). Yet, for anions the diffusion-accessible porosity is smaller due to repulsion by the negative layer charge of clay mineral surfaces and the resulting exclusion of anions from small pores ($\varepsilon_{eff} < \varepsilon$). This phenomenon is called anion exclusion (see also sub-chapter 3.2.1).[31]

2.2 The natural clay rock Opalinus Clay (OPA)

OPA is one of the clay formations in Europe, which is under scientific investigation as potential host rock for a HLW repository in Switzerland. Comprehensive studies on OPA started in January 1996 at the underground research laboratory (URL) in Mont Terri, located nearby St. Ursanne (northwest Switzerland),[13] where 22 partner institutions from 9 countries are investigating geochemical, hydrogeological, and rock mechanical properties of OPA.[32] OPA is a fine-grained, compacted, sedimentary clay rock, which was deposited approximately 180 Ma ago in an epicontinental shallow-marine environment of the Jurassic sea.[13] Presently, OPA sediments can be found in the southern part of Germany, as well as in Northern Switzerland.[33]

OPA is featured by a dominantly mesoporous structure (pore diameters 2–50 nm).[34] Total porosities range between 0.14 and 0.18 and dry densities range between 2400 and 2500 kg/m³.[35] OPA can be subdivided into five lithological sub-units (i.e., facies), of which the most relevant are the shaly and the sandy facies.[13,35] The mineralogical compositions of the different facies are similar, however, there are slight facies-dependent variations in the relative proportions of the individual mineral components.

Tab. 3 gives an overview of the mineralogical compositions of the shaly and sandy facies of OPA, based on the average of 7 and four samples, respectively.[13] Note, the mineralogical composition exhibits variations also depending on bedding plane anisotropy and the actual location in the URL, where the sampling was performed. As it can be seen, in both facies, the main constituents are clay minerals, followed by calcite and quartz. In comparison, the shaly facies has a larger calcite fraction, while the sandy facies has a larger quartz fraction.

Tab. 3 Range of mineralogical compositions of the shaly and sandy facies of OPA.[13]

Component	OPA, shaly facies / wt.%	OPA, sandy facies / wt.%
Illite	16–40	15–35
Illite/smectite mixed layer	5–20	5–20
Kaolinite	15–33	13–35
Chlorite	4–20	4.4–15
Σ clay minerals	58–76	45–70
Quartz	6–24	16–32
Calcite	5–28	7–17
Siderite	1–4	1.1–3
K-feldspar	1–3.1	2.5–5
Albite	0.6–2.2	0.8–2.2
Dolomite	0.2–2	0.3–2
Pyrite	0.6–2	0.7–3.2
Organic carbon	< 0.1–1.5	0.2–0.5

Similar to the mineralogy of the clay rock, the OPA pore water compositions also exhibit a variability. This is also due to the fact that the low permeability of OPA makes pore water sampling a challenging undertaking. Two of the most common methods for pore water sampling are high-pressure squeezing and leaching of clay rock cores. Since not all pore water parameters are available experimentally, also geochemical modeling is utilized for determination of pore water chemistry. Based on the experimental and modelled data, reference pore water compositions were defined, which are used as background electrolytes, for instance, in laboratory-scale sorption and diffusion experiments (see also sub-chapter 5.3).[1,36]

The two main components of OPA pore water are Na^+ and Cl^- (> 5000 mg/L), resulting in $I \approx 0.3$ mol/L.[13] The pH of OPA pore water is neutral to slightly alkaline (≈ 7–8). The carbonate minerals calcite and dolomite are considered determinants for the pore water pH due to the HCO_3^-/CO_3^{2-} equilibrium.[13] Under unperturbed conditions (i.e., absence of atmospheric oxygen), OPA pore water is reducing ($E_h \approx -200$ mV)[37] mainly due to the presence of pyrite which releases Fe(II) and sulfide into the pore water. The most relevant redox couple controlling such redox potential is pyrite/sulfate.[37,38] This is particularly relevant in the context

of nuclear waste disposal, since pyrite is able to partially immobilize Np(V) species by reduction to Np(IV) (see sub-chapter 3.2.1).[39] Further components of OPA pore water with concentrations 10–5000 mg/L are K^+, Mg^{2+}, Ca^{2+}, Sr^{2+} as well as SO_4^{2-}.[40]

3 Diffusive transport of radionuclides

3.1 Theoretical background of molecular diffusion

The diffusive flux J [mol/(m²·s)] of a solute in one spatial direction is expressed by Fick's first law:

$$J = -D_e \cdot \frac{\partial c}{\partial x} \quad \textbf{Eq. 2}$$

where D_e [m²/s] is the effective diffusion coefficient, c [mol/m³] is the concentration of the diffusing tracer in the mobile phase, and x [m] is the spatial coordinate. The concentration change with time is given by Fick's second law:

$$\frac{\partial c}{\partial t} = D_a \cdot \frac{\partial^2 c}{\partial x^2} \quad \textbf{Eq. 3}$$

where t [s] is time and D_a is the apparent diffusion coefficient. D_e and D_a are linked by the rock capacity factor α [–]:

$$D_a = \frac{D_e}{\alpha} \quad \textbf{Eq. 4}$$

The rock capacity factor α is defined as

$$\alpha = \varepsilon_{eff} + \rho_d \cdot K_d \quad \textbf{Eq. 5}$$

where ε_{eff} [–] is the diffusion-accessible porosity, ρ_d [kg/m³] is the dry density of the stationary phase, and K_d [m³/kg] is the distribution coefficient. K_d is defined as

$$K_d = \frac{a_{eq}}{c_{eq}} \quad \textbf{Eq. 6}$$

where a_{eq} [mg/g] is the amount of tracer sorbed onto the solid phase and c_{eq} [mg/L] is the tracer concentration in the mobile phase in equilibrium.

For non-sorbing tracers (i.e., $K_d = 0$), α is equal to ε_{eff}. While D_e describes solely the diffusive transport through the porous matrix, D_a additionally considers the sorption of the tracer on the solid surface. Hence, when describing the diffusion of strongly sorbing tracers (e.g., Cs(I), Eu(III), Am(III)) through clay materials, where the transport is retarded by sorption processes, D_a is often given instead of D_e.

D_e is also related to the diffusion coefficient in bulk water D_w [m²/s]:

$$D_e = D_w \cdot \frac{\varepsilon_{eff} \cdot \delta}{\tau^2} \qquad \textbf{Eq. 7}$$

where δ [–] is the constrictivity, taking into account the pore diameter´s impact on a diffusing species and τ [–] is the turtuosity which describes to which extent the diffusion path (i.e., the pore) is twisted or bended. Since constrictivity and turtuosity cannot be determined independently from each other, they are usually combined in the geometrical factor G [–]:

$$G = \frac{\tau^2}{\delta} \qquad \textbf{Eq. 8}$$

For a known porosity of a porous material, diffusion coefficients can often be reliably estimated by applying an empirical formula, called Archie´s law:[41]

$$\varepsilon^m = \frac{D_e}{D_w} \qquad \textbf{Eq. 9}$$

where m is an empirical factor (cementation factor). D_e and D_w are also correlated to the pore diffusion coefficient D_p [m²/s]:

$$D_e = D_w \cdot \frac{\varepsilon_{eff}}{G} = D_p \cdot \varepsilon \qquad \textbf{Eq. 10}$$

3.2 Diffusion of radionuclides through clay materials

As already noted in sub-chapter 2.1, clay materials are generally featured by a very low hydraulic conductivity. Hence, the dominant process of radionuclide transport through clay is molecular diffusion, which is influenced by a variety of properties, both of the diffusing species,

and the clay material itself. In the following, an overview of the diffusion-affecting tracer and clay properties will be given.

3.2.1 Influence of radionuclide speciation and accessible porosity

The diffusive transport of radionuclides through clay materials is influenced by various parameters, such as pore water chemistry (i.e., elemental composition, I, pH, E_h), charge of the diffusing radionuclide and, ultimately, its aqueous speciation.[26,42,43] Depending on the radionuclide, additionally to effective diffusion, also sorption processes have to be taken into account. Sorption onto clay minerals can considerably retard the diffusion of radionuclides, resulting in D_a values which can be several orders of magnitudes lower, than the corresponding D_e (**Tab. 7**).[12] Based on its K_d value, a radionuclide can be roughly categorized in non-, weakly, moderately, and strongly sorbing.

As a neutral molecule, tritiated water (HTO) is non-sorbing (K_d = 0 m³/kg). Halide anions, such as Cl^- and I^-, are repelled from the negatively charged clay mineral layers and are therefore, also practically non-sorbing. As mentioned in sub-chapter 2.1.3, cations and neutral species, such as HTO, have a higher ε_{eff}, than anions, since small pores are not fully accessible for the anions due to anion exclusion. Therefore, in general, anions are less mobile through the porous structure of clays, than HTO. In diffusion experiments through OPA it was observed that ε_{eff} for Cl^- and I^- were 1.5 to 2 times lower compared to ε_{eff} of HTO, resulting in D_e values of Cl^- and I^- being approximately four times lower, than that of HTO (**Tab. 4**).[44]

Tab. 4 Selected parameter values for D_e and K_d of HTO, Cl^-, and I^- in OPA (bedding $\perp$), obtained by diffusion and batch sorption experiments, reported by Van Loon *et al.* (2003) for pH = 7.6, I = 0.39 mol/L, and p = 5 MPa.[44]

Radionuclide/ species	**Concentration / (mol/L)**	ε_{eff} / –	D_e / (× 10^{-11} m^2/s)	K_d / (m^3/kg)
HTO	5.9×10^{-10}	0.11±0.02	1.23±0.06	0
$^{36}Cl^-$	2.4×10^{-5}	0.05±0.01	0.40±0.02	0
$^{125}I^-$	3.4×10^{-11}	0.07±0.01	0.32±0.02	$\approx 10^{-5}$

Owed to their positive charge, cations exhibit sorption onto clay minerals to varying extent, in particular on negatively charged basal surfaces. However, cation sorption is fairly complex, since cations can sorb via different mechanisms onto clay mineral particles, such as ion exchange with subsequent outer-sphere complexation of the cation and inner-sphere surface complexation (see sub-chapter 2.1.3).[26,42] In order to understand why a particular sorption

mechanism is dominant for a certain metal ion, several underlying factors have to be considered, such as pH and *I* of the background electrolyte. In particular, the effective charge (i.e., charge-to-size ratio) of the cation has to be taken into account, since it governs the size of the cation´s hydration sphere and its ability to undergo hydrolysis (i.e., formation of hydroxo complexes).

Mono- and divalent metals (e.g., Na^+, Sr^{2+}) preferentially sorb electrostatically via cation exchange onto the basal surfaces of clay minerals (i.e., outer-sphere complexation). The sorption affinity of such mono- and divalent cations to clay mineral basal surfaces is mainly governed by the size of the cation´s hydration sphere (i.e., hydration radius $r_{aq.}$ [Å]), since it determines the average distance between the negatively charged clay mineral layer and the cation. The hydration radius depends on the cation´s effective charge, which itself is correlated with the cation´s charge and ionic radius *r* [Å]. Small cations, such as Na^+ ($r(Na^+)$ = 1.08 Å), bear a high effective charge, thus, are featured by a larger hydration radius ($r_{aq.}(Na^+)$ = 2.76 Å), than larger cations from the same group of the periodic table, such as Cs^+ ($r(Cs^+)$ = 1.67 Å, $r_{aq.}(Cs^+)$ = 2.28 Å).[45] Its larger hydration radius causes Na^+ to interact with clay mineral surfaces only weakly. Conversely, the smaller hydration radius of Cs^+ makes it a strongly sorbing nuclide. Such trends are also reflected in the corresponding K_d and D_a values. Under similar experimental conditions (i.e., pH, *I*, see **Tab. 5**) the K_d of Na^+ in OPA is lower by more than a factor of 10^4 compared with that of Cs^+. For an aqueous Cs^+ concentration of 1.7×10^{-9} mol/L, as established in the work of Van Loon and Müller (2014),[46] D_a of Cs^+ in OPA was $\approx 8 \times 10^{-13}$ m²/s, thus, more than 200 times lower, compared to that of Na^+ (**Tab. 5**) and hundred times lower, than that of Cl^- (**Tab. 4**). The dependency of cation exchange on r_{aq}(cation) was also observed by Molera *et al.* (2002)[42] for the sorption of Na^+, Cs^+, Sr^{2+}, and Co^{2+} in MX-80 bentonite. At pH = 7, K_d values increased in the direction of decreasing r_{aq} ($Na^+ > Sr^{2+} > Cs^+ > Co^{2+}$).[45] The same trend for these four nuclides was also observed in OPA (**Tab. 5**).[22,43,46,47] To a lesser extent, the *I* of the pore water has also an impact on the sorption of mono- and divalent cations, as pointed out in sub-chapter 2.1.3. With increasing *I* (0.05, 0.1, 1.0 mol/L), but otherwise identical experimental conditions, a slight decrease of the K_d of Na^+ by a factor of 2–4 was observed in MX-80 bentonite (**Tab. 5**).[42]

As already noted in sub-chapter 2.1.3, another important type of sorption mechanism is inner-sphere surface complexation, in which cations lose parts of their hydration shell and bind to surface hydroxyl groups at edge surfaces of the clay mineral layer. The most relevant determinant for inner-sphere surface complexation is pH, since it governs the protolysis of the amphoteric sites at the edge surfaces.[23] Molera *et al.* (2002)[42] investigated the pH-dependent sorption of mono and divalent cations in MX-80 bentonite at varying pH (4–10). K_d values of

Na^+ and Cs^+ were found to be constant in the investigated pH range, since the studied cations mainly undergo sorption via cationic exchange which is practically pH-independent. K_d values of Sr^{2+} and Co^{2+} were also constant for pH 4–7. However, for pH 9, K_d values of Sr^{2+} and Co^{2+} were elevated by a factor of approximately 2 and 20, respectively. The increase in K_d values was attributed to additional inner-sphere surface complexation. Cs^+ sorption is a more complex phenomenon, since it involves a further binding site. A widely accepted concept for Cs^+ sorption onto illite clay minerals involves three relevant binding sites. Depending on their sorption affinity, they are referred to as "high affinity" (i.e., frayed edge sites; see sub-chapter 2.1.3) and "low affinity" sites.[48] The Cs^+ uptake by frayed edge sites is not only depending on pH, but also on the equilibrium concentration of Cs^+ in the pore water. This causes Cs^+ sorption to be non-linear[49] and Cs^+ diffusion coefficients to be concentration-dependent.[27]

As already noted in sub-chapter 3.1, the diffusion of strongly sorbing nuclides is more appropriately described with D_a instead of D_e. For instance, Van Loon *et al.* (2004, 2014)[22,46] observed fairly comparable D_e values for the weakly sorbing Na^+ (7×10^{-11} m²/s)[22] and the strongly sorbing Cs^+ (2×10^{-10} m²/s)[46] in OPA. However, due to the more than two orders of magnitudes higher K_d of Cs^+, D_a of Cs^+ is, consequently, more than two orders of magnitudes lower. The varying sorption and diffusion properties of the described cations are reflected in their K_d, D_e, and D_a values (**Tab. 5)**.

Tab. 5 Parameter values for D_e, K_d, and D_a of selected mono- and divalent cations in clay materials, obtained from diffusion and/or batch sorption experiments.

Radionuclide / species	Concentration / (mol/L)	Clay type, bedding, ε_{eff} / –	Pore water pH, I / (mol/L)	D_e / ($\times 10^{-11}$ m^2/s)	K_d / (m^3/kg)	D_a / ($\times 10^{-11}$ m^2/s)	References
$^{22}Na^+$	(4.3–4.7) $\times 10^{-8}$ *	OPA, ∥, 0.15±0.02 **	7.6, 0.39	7.2±0.5	(1.0±0.2) $\times 10^{-4}$ #	18±2 ##	Van Loon *et al.* (2004)[22]
$^{22}Na^+$	2×10^{-9}	OPA, ⊥, 0.11±0.02	7.6, 0.39	1.4±0.1	(1.0±0.2) $\times 10^{-4}$	3.9±0.5 #	Van Loon *et al.* (2005)[43]
$^{22}Na^+$	$\approx 10^{-6}$	MX-80 bentonite, –, 0.32	≈ 7, 0.05 ≈ 7, 0.1 ≈ 7, 1.0	– – –	6×10^{-3} 2.8×10^{-3} 1.3×10^{-3}	– 3.8 –	Molera *et al.* (2002)[42]
$^{134}Cs^+$	$\approx 10^{-6}$	MX-80 bentonite, –, 0.32	≈ 7, 0.1	–	≈ 0.6	≈ 3.3	Molera *et al.* (2002)[42]
$^{134}Cs^+$	3.8×10^{-8}	OPA, ∥, 0.16	7.9, 0.39	18	≈ 0.6**	≈ 0.01 ⅀	Van Loon *et al.* (2014)[46]
$^{85}Sr^{2+}$	1.5×10^{-11}	OPA, ⊥, 0.11±0.02	7.6; 0.39	1.4±0.1	(7.0±1.4) $\times 10^{-4}$	0.75±0.08**	Van Loon *et al.* (2005)[43]
$^{85}Sr^{2+}$	$\approx 10^{-6}$	MX-80 bentonite, –, 0.32	≈ 7, 0.1 ≈ 9, 0.1	– –	≈ 0.04 ≈ 0.08	0.9 –	Molera *et al.* (2002)[42]
$^{60}Co^{2+}$	$\approx 10^{-6}$	MX-80 bentonite, –, 0.32	≈ 7, 0.1 ≈ 9, 0.1	– –	≈ 1.6 ≈ 32	10^{-3}	Molera *et al.* (2002)[42]
$^{60}Co^{2+}$	$\approx 10^{-13}$	OPA, ∥, 0.15	7.5, 0.3	6.0	0.09	0.03	Wersin *et al.* (2008)[47]

* concentration range indicates final and initial concentrations in high-concentration reservoir. ** indicated ε_{eff} is ε_{eff}(HTO). # taken from Van Loon *et al.* (2005).[43] ## calculated with reported D_e, K_d, ε_{eff}, and ρ_d in cited study. ⅀ calculated with reported D_e, ε_{eff}, and ρ_d in cited study, as well as K_d from Bradbury *et al.* (2003).[49]

All cations presented in **Tab. 5** are featured by a fairly simple aqueous chemistry, since they are usually present as aquo ions. For cations with higher electric charge (≥ +3), commonly lanthanides, actinides, and other transition metals, additionally, hydrolysis and the formation of complexes with inorganic (e.g., CO_3^{2-}, SO_4^{2-}, Cl^-) and organic ligands (e.g., humic[2,50] and fulvic acids[11]) present in the clay rock/pore water system, has to be taken into account. With increasing electric charge, actinide cations tend to undergo hydrolysis in aqueous solution, which leads to the formation of hydroxo complexes. Such especially pronounced hydroxo complexes of trivalent ($[Am(OH)]^{2+}$, $[Pu(OH)]^{2+}$)[51] and tetravalent actinides ($Th(OH)_4$ (aq.), $Pu(OH)_4$ (aq.))[51] are known to have strong affinities toward clay mineral surfaces and are

therefore considered strongly sorbing and consequently, slowly diffusing species. Depending on the aqueous HCO_3^-/CO_3^{2-} concentration, also carbonato complexes can be formed, such as $[Am(CO_3)]^+$.[51]

Despite their high oxidation states, penta- and hexavalent actinides, such as Np(V) and U(VI), are only moderately sorbing. This is due to the fact that such nuclides are not present as highly charged aquo cations, but as actinyl cations $An(V)O_2^+$ and $An(VI)O_2^{2+}$ which causes them to have considerably decreased effective charges (**Tab. 6**) and are, consequently, less prone to hydrolysis.

Tab. 6 Charge and effective charge of cationic actinide species.[52]

Actinide species	Charge	Effective Charge
$An(V)O_2^+$	+1	≈ +2.2
$An(VI)O_2^{2+}$	+2	≈ +3.3
An^{3+}	+3	+3
An^{4+}	+4	+4

The differing sorption affinities of the described actinide species are also reflected in their individual K_d values. In OPA, for U(VI) (≈ 0.025 m³/kg)[2,53] and Np(V) (≈ 0.10 m³/kg)[9] up to three orders of magnitude lower K_d values were reported compared to Am(III) (≈ 30 m³/kg), Th(IV) (≈ 29 m³/kg), and Pu(IV) (≈ 83 m³/kg) (**Tab. 7**).[51] Sawaguchi *et al.* (2013)[12] investigated sorption and diffusion of Am(III) and Np(IV) in a MX-80 bentonite/sand mixture and found apparent diffusivities which were similar or even higher, than those of Np(V) and U(VI), as shown in **Tab. 7**. However, in such study, carbonate ($[CO_3^{2-}]$ = 0.3 mol/L) was added as complexing agent, resulting in the formation of weakly sorbing, thus, rather mobile anionic species $[Am(CO_3)_3]^{2-}$ and $[Np(CO_3)_2(OH)_2]^{2-}$, while under natural pore water conditions in OPA ($[CO_3^{2-}] \approx 10^{-3}$ mol/L)[13] the less mobile cationic species $[Am(OH)]^{2+}$, $[Am(CO_3)]^+$, and NpO_2^+ are expected. With respect to diffusion coefficients, also the different ε_{eff} of bentonite and OPA must be considered. Yamaguchi *et al.* (2007)[11] reported ε_{eff} = 0.4 for a bentonite/sand mixture, while clay rocks, such as, OPA, usually have ε_{eff} of 0.05–0.16 (**Tab. 4, Tab. 5, Tab. 7**), depending on the charge of the diffusing species. Hence, elevated D_a values obtained for Am(III) and Np(IV) in bentonite, compared with those obtained for U(VI) and Np(V) in OPA, can partially also be attributed to the higher diffusion-accessible porosity of bentonite.

Anionic actinide species are, similar to simple halide anions, usually non- or weakly sorbing. Neutral and cationic actinide species undergo moderate or strong sorption via inner-sphere surface complexation, as reported by Turner *et al.* (1998)[54] for Np(V) sorption onto montmorillonite and by Glaus *et al.* (2020)[26] for Eu(III), which is considered as analog for the trivalent actinides Pu(III), Am(III), and Cm(III).

Tab. 7 Parameter values D_e, K_d, D_a of selected actinide nuclides in clay materials, obtained by diffusion and/or batch sorption experiments, and their corresponding dominant aqueous species (dominant species account for ≥ 50 % of all occurring species in the studied system).

Actinide nuclide	Clay type	pH	*I* / (mol/L)	Dominant aqueous species	K_d / (m^3/kg)	D_e / ($\times 10^{-12}$ m^2/s)	D_a / ($\times 10^{-14}$ m^2/s)	References
^{232}Th(IV)	OPA	7.6	0.4	$Th(OH)_4$ (aq.)	29±16	–	–	Amayri *et al.* (2016)[51]
^{233}U(VI)	OPA (ε_{eff} = 0.16)	8.7*	0.36	$Ca_2UO_2(CO_3)_3$ (aq.)	0.025±0.003	1.9±0.4	3.1±0.3**	Joseph *et al.* (2013)[2]
^{237}Np(IV)	Sand-bentonite mixture (ε_{eff} = 0.4)	≈ 9	≈ 0.8	$[Np(CO_3)_2(OH)_2]^{2-}$	0.032±0.007	90±41	170±60	Yamaguchi *et al.* (2007)[11]
^{237}Np(V)	OPA (ε_{eff} = 0.15±0.01)	7.6	0.39	NpO_2^+	0.10±0.01	6.9±1.1	≈ 2.9**	Wu *et al.* (2009)[9]
^{239}Pu(IV)	OPA	7.6	0.4	$Pu(OH)_4$ (aq.)	83±34	–	–	Amayri *et al.* (2016)[51]
^{241}Am(III)	OPA	7.6	0.4	$[Am(OH)]^{2+}$, $[Am(CO_3)]^+$	30±2	–	–	Amayri *et al.* (2016)[51]
^{241}Am(III)	Sand-bentonite mixture	8.8	–	$[Am(CO_3)_3]^{3-}$	–	–	≈ 1.7	Sawaguchi *et al.* (2013)[12]

*Initial pH was 7.6; 8.7±0.1 is average pH of two replicate diffusion cells, determined at the end of the experiment.**calculated with reported D_e, K_d, ρ_d, and ε_{eff} in cited study.

3.2.2 Influence of clay properties on diffusion

HLW repositories to be built in natural clay rock will be located several hundreds of meters below ground. For instance, the German site selection act requires a minimum depth of 300 m for the disposal rooms.[5] At such depth, the overburden can exert pressures of several MPa onto the subjacent clay layers. This overburden pressure, also called confining pressure, has an influence on several rock properties relevant for the diffusion behavior of radionuclides, such as degree of compaction, diffusion accessible porosity, and tortuosity. Van Loon *et al.* (2003)[44] studied the influence of confining pressure on the diffusion of anionic and neutral species through OPA perpendicular to the bedding. For confining pressures from 1 to 5 MPa, D_e values

of HTO, $^{36}Cl^-$, and $^{125}I^-$ decreased by approximately 17, 28, and 30 %, respectively. The more distinct decrease for $^{36}Cl^-$ and $^{125}I^-$ was attributed to anion exclusion.

As noted in sub-chapter 2.1, growing confining pressure by the host rock overburden causes increasing compaction of the clay (i.e., increasing dry density ρ_d) which, in turn, influences the geometrical properties of the porous clay structure and, ultimately, ε_{eff} of the clay material. Although more relevant for anionic species, clay compaction and the resulting ρ_d impacts the accessible porosity for neutral and cationic species, as well.[55] In general, for any type of nuclide, D_e tends to decrease with increasing ρ_d of the clay. In a long-term study (6 years experimental time) Joseph *et al*. (2017)[10] investigated the diffusion behavior of U(VI) in MX-80 bentonite as function of dry density. For dry densities 1.3, 1.6, and 1.9 g/cm³ final diffusion distances of U(VI) of 3, 1.5, and 1 mm, respectively, were observed. This decrease of diffusion distance and, consequently, of the D_e, is explained with a lower ε_{eff} and higher tortuosity with increasing bentonite density.

As explained in sub-chapter 2.1, during clay diagenesis the confining pressure increases with progressing clay rock sedimentation, which causes the clay mineral particles to arrange preferentially perpendicular relative to the direction of sedimentation. Such preferential orientation is called bedding. It is to be expected that geometric parameters, such as tortuosity, are different parallel and perpendicular to the bedding, thus, clay rock is considered anisotropic.[22] For instance, tortuosity in OPA was found to be up to 5 times higher perpendicular to the bedding.[28] The impact of such anisotropy on the diffusion of radionuclides was investigated by Van Loon *et al*. (2004).[22] It was found that diffusion of HTO, $^{22}Na^+$, $^{36}Cl^-$ parallel to the bedding is faster by a factor of about 4 to 6 compared to diffusion perpendicular to the bedding (**Tab. 5**). This phenomenon is explained by a smaller tortuosity (i.e., shorter path length for the diffusing species) and consequently, faster diffusive transport parallel to the bedding.

3.3 Comparison of diffusion setups

The choice of the setup and its components for a diffusion experiment in clay materials heavily depends on the kind of nuclide to be studied. Particularly relevant is the expected diffusion distance of the nuclide in the clay material which depends on both the kind of diffusing species and the properties of the clay material itself (see sub-chapter 3.2).

The following paragraphs will give an overview and comparison of experimental setups for the investigation of the diffusion of various radionuclides in different clay materials. The suitability

of each setup for the study of the diffusion of the moderately sorbing U(VI) (expected dominant species $Ca_2UO_2(CO_3)_3$ (aq.)) and the strongly sorbing Am(III) (expected dominant species $[Am(CO_3)]^+$) through the OPA rock / pore water system,[1] down to ultra-trace concentrations will be discussed.

3.3.1 Through-diffusion method

In a through-diffusion experiment, the clay sample is connected to two reservoirs containing the background electrolyte solution. One of which is spiked with the radionuclide tracer (source reservoir), while the other is initially free of tracer (receiving reservoir). In order to maintain a constant tracer concentration in the source reservoir, it is regularly replaced by a reservoir with freshly spiked pore water. Alternatively, the volume of the source reservoir solution is chosen to be significantly higher as the clay volume. Consequently, a decrease of the tracer will not change the tracer concentration in a definite uncertainty range. As shown in **Fig. 10**, a classical through-diffusion setup comprises a diffusion cell, containing the clay specimen, a peristaltic pump which moves the background electrolyte (e.g., synthetic pore water in this study, spiked with the diffusing tracer) from the source reservoir to the clay sample and back to the source reservoir. By monitoring the evolution of the tracer concentrations in both reservoirs, the mass transfer of tracer through the clay as a function of time and ultimately, a diffusion profile can be determined. If required, loads of several MPa can be applied to the diffusion cell, in order to simulate confining pressure.

Through-diffusion is usually the method of choice for non- and weakly sorbing tracers, such as HTO, Na^+, and Cl^-.[56] It was, however, also successfully applied for the study of the moderately sorbing $Ca_2UO_2(CO_3)_3$ (aq.) in OPA (**Fig. 10**).[2] The through-diffusion method is compelling, since both D_e and α are directly accessible from the same experiment. There is a transient phase, during which the diffusive flux J increases. Once J reaches a constant value, the diffusion experiment is in steady phase, in which the total diffused tracer mass ($n_{diff\text{-}tot}$ [mol]) increases linearly with time. Based on the diffusion profile obtained during the steady phase, D_e and α can be derived from the slope of the asymptote of $n_{diff\text{-}tot}$ and its intercept with the y-axis, respectively, as shown in **Fig. 11**.

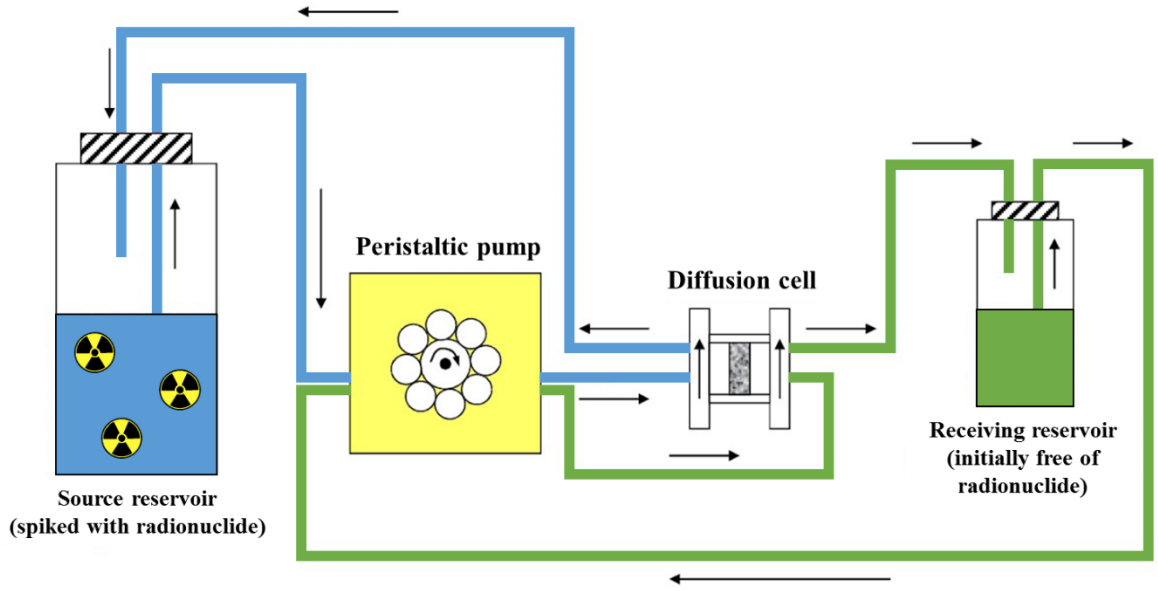

Fig. 10 Through-diffusion setup for the study of ^{233}U(VI) diffusion through OPA (adopted from Joseph *et al.* (2013)[2]).

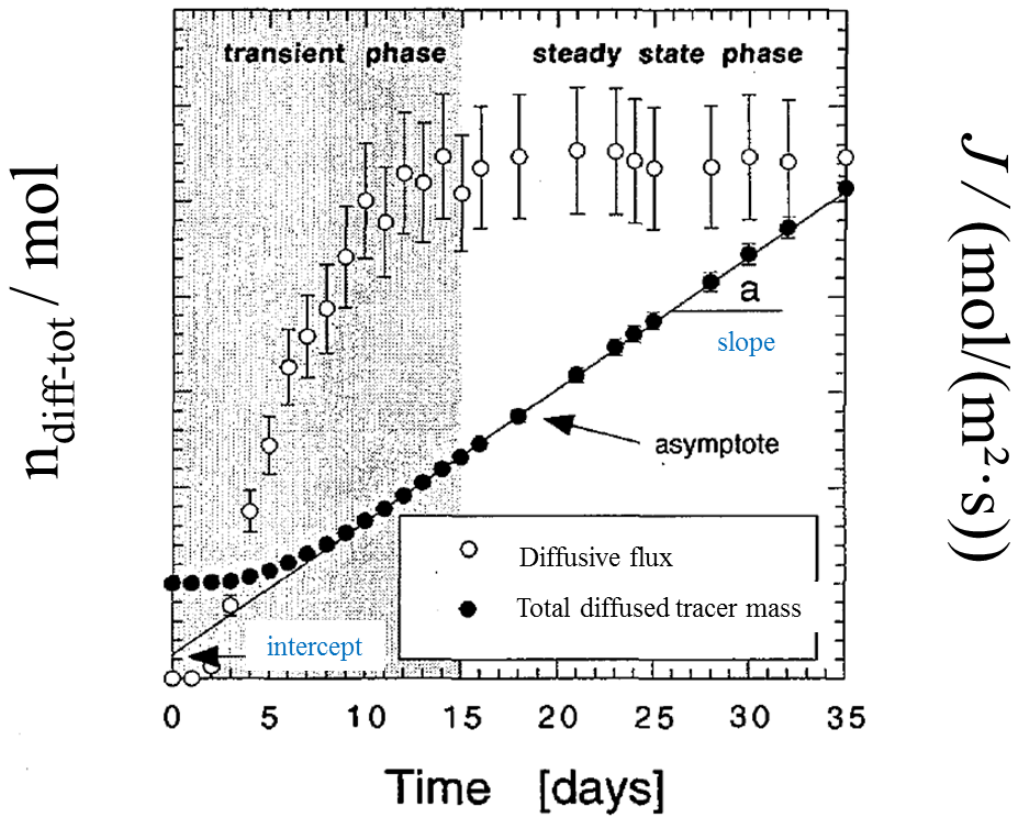

Fig. 11 Evolution of diffusive flux and total diffused tracer mass as function of time in the source reservoir of a through-diffusion experiment (adopted from Van Loon *et al.* (2004)[57]).

While the through-diffusion setup is applicable for the study of non-, weakly, and moderately sorbing species, it is not favored for strongly sorbing nuclides, such as Eu(III), Pu(IV), and Am(III). The slow mass transfer of the diffusing tracers through the clay material would result in very long experimental durations before a steady state is established. More importantly, the strong sorption to cell components would result in an extremely slow mass transfer through the clay sample. There are studies available in which strongly sorbing tracers were investigated using a through-diffusion setup.[11,12] In these studies, the speciation of the tracers changed due to applying an about 100 times higher carbonate concentration, leading to the formation of weakly sorbing, mobile anionic species, such as $[Am(CO_3)_3]^{3-}$,[12] (see sub-chapter 3.2.1).

3.3.2 Radial diffusion method

A variant of classical through-diffusion is the radial diffusion method. While originally developed for the determination of isotopic compositions of groundwater in aquitards,[58] the radial diffusion method has been adapted to the study of the diffusion of the halides Cl^- , Br^-,[59] and I^- [60] through clay rock samples from the Tournemire experimental facility, as well as to the investigation of $^{22}Na^+$ and $^{36}Cl^-$ diffusion through OPA under confining pressures of up to 14 MPa.[22] Although conceptually similar to through-diffusion, the radial diffusion method is favorable when studying diffusion parallel to the bedding, while applying pressure to the bedding.

This setup comprises a cylindrical sample of OPA, with a central hole drilled perpendicular to the bedding, serving as reservoir containing the pore water, spiked with the tracer. Two cylindrical stainless-steel filters (**Fig. 12**) surround the clay cylinder and ensure its integrity during the experiment. The overburden pressure present in the real host rock is simulated by applying a confining pressure perpendicular to the bedding. The diffusion profile is determined by monitoring the temporal change of the tracer concentrations in the source and receiving reservoirs.

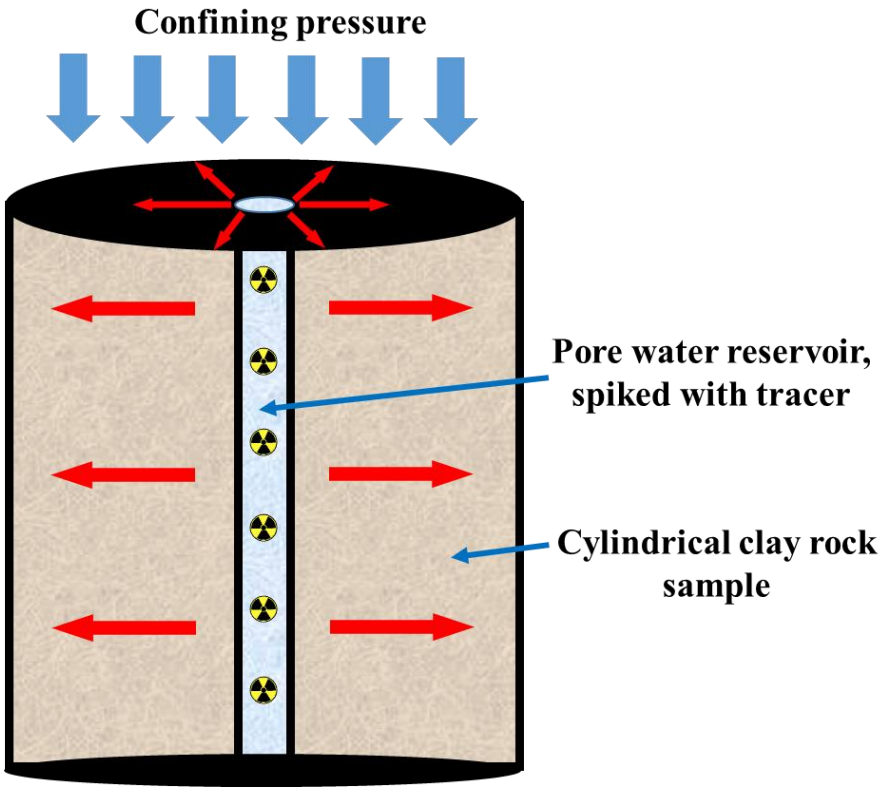

Fig. 12 Radial diffusion setup for the study of $^{22}Na^{+}$ and $^{36}Cl^{-}$ diffusion through OPA (adopted from Van Loon *et al*. (2004)[22]). Red arrows indicate the direction of diffusion, as well as the orientation of the bedding.

For the same reasons, as described for the through-diffusion setup, the radial diffusion method is generally not applicable for the investigation of strongly sorbing tracers.

3.3.3 Planar-source diffusion method

The planar-source diffusion method is a type of closed cell experiment, where a radionuclide source is placed between two saturated clay samples, enclosed in a diffusion cell. During the diffusion experiment no samplings (e.g., of pore water) are performed. Only after termination of the experiment, the diffusion cell is dismantled and the spatial distribution of the diffusing tracer in the clay samples is determined.

The feasibility of this kind of setup has already been demonstrated for the study of strongly sorbing $^{75}Se(IV)$ diffusion through unsaturated soil samples,[61] as well as for the diffusion of $^{60}Co(II)$ and $^{152}Eu(III)$ diffusion through saturated compacted FEBEX bentonite.[62] The setup used in the latter study is depicted in **Fig. 13**. A filter paper is impregnated with 0.1 mL of tracer solution ([Co] $\approx 10^{-6}$ mol/L; [Eu] $\approx 4 \times 10^{-6}$ mol/L) and placed between two plugs of saturated FEBEX bentonite clay. The clay plugs are held in place by two end-pieces of stainless-steel filters and are surrounded by a stainless-steel tube. At the end of the experiment, the cell is

disassembled and both clay plugs are sliced into thin layers. By examining the tracer content in each slice of the two clay plugs, a symmetrical diffusion profile is obtained (**Fig. 14**).

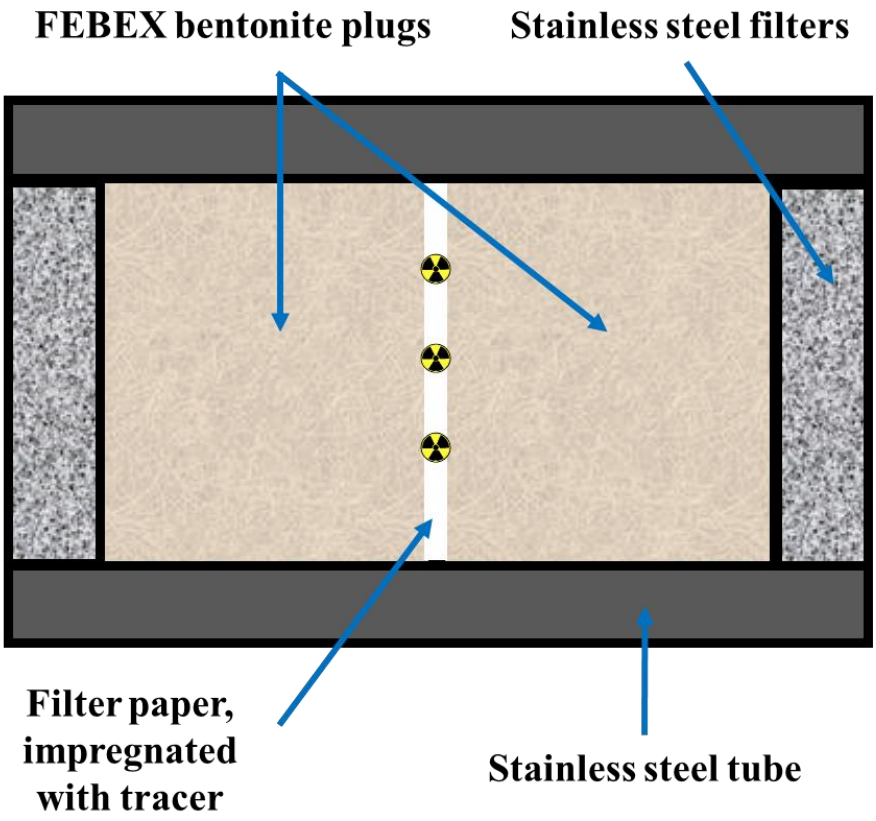

Fig. 13 Planar-source diffusion setup for the study of ^{60}Co(II) and ^{152}Eu(III) in FEBEX bentonite (adopted from García-Gutiérrez *et al.* (2011)[62]).

The planar-source method is beneficial when studying strongly sorbing nuclides, since no bulk pore water reservoirs are required. In this way, tracer loss due to sorption onto the walls of the reservoir is avoided. However, this kind of setup only gives information about the D_a. Due to the absence of solution, the temporal change in tracer concentration cannot be monitored, which is needed to determine D_e.

In the study of García-Gutiérrez *et al.* (2011),[62] the added amount of ^{152}Eu(III) was approximately 4×10^{-10} mol. It cannot be ruled out that for initial tracer concentrations several orders of magnitude lower (as investigated in the frame of this PhD study), a significant portion of the tracer would sorb onto the filter paper or undergo complexation by organic molecules (e.g., cellulose) present in the filter paper, thus, biasing the initial tracer concentration.

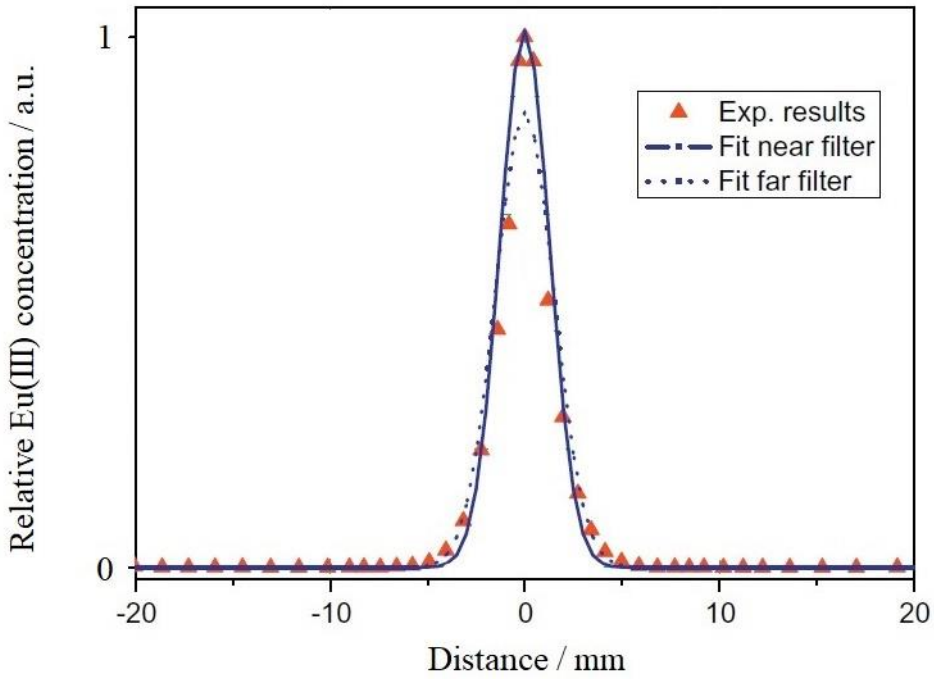

Fig. 14 Symmetrical diffusion profile of Eu(III) in FEBEX bentonite obtained via planar-source method. Positive and negative distances represent spatial Eu(III) distributions in the right and left clay tablet, respectively (adopted from García-Gutiérrez *et al.* (2011)[62]).

3.3.4 In-diffusion method

As noted in sub-chapter 3.3.1, strongly sorbing nuclides cannot be examined with a through-diffusion setup due to slow mass transfer through the clay sample. The mass transfer would be even further reduced by tracer sorption onto components commonly present in through-diffusion setups, such as tubings and filters. Hence, it is of utmost importance to avoid the use of such components, in particular the use of filters.

By utilizing a filter-free in-diffusion setup in combination with post-mortem profile analysis the aforementioned challenges can be overcome. A cylindrical clay rock sample is embedded into a PMMA (poly(methyl methacrylate)) sample holder with epoxy resin, while one end of the sample remains free of resin. This part of the sample is immersed into a pore water reservoir, spiked with the radionuclide tracer (**Fig. 15**). During the experiment the temporal evolution of the tracer concentration in the pore water reservoir is monitored. After termination of the experiment, the cylindrical clay sample is sliced in thin layers with layer thicknesses of approximately 100 µm.[46] The diffusion profile of the investigated nuclide is determined based on the tracer concentration´s evolution in the reservoir during the experiment and the post-mortem profile analysis.

Such kind of a setup was successfully applied for the study of $^{134}Cs^{+}$ diffusion through OPA[46] and is applied to study U(VI) and Am(III) diffusion through OPA in the frame of this PhD thesis. Based on the profile data, D_e, K_d, and D_a are determined using a finite element method by fitting a model profile curve based on Fick's law to the experimental profile data.

Although this setup does not contain filters and tubings, tracer sorption onto the walls of the pore water reservoir, as well as on the immersed part of the clay sample holder and on the resin will still occur. In a previous study it was shown for $^{244}Pu(IV)$ and $^{243}Am(III)$ in granitic groundwater (pH = 9.2) stored in polyethylene (PE) vials that after 20 d up to 90 % of the actinides are sorbed onto the PE surface.[63] This has to be considered by equilibrating the pore water reservoir with the tracer prior to the diffusion experiment. Only after reaching a constant aqueous tracer concentration, the diffusion sample is immersed into the reservoir solution and the diffusion experiment started. It shall be noted, that the absence of filters poses an additional challenge with respect to low cemented clay rocks, such as OPA. Without filters, the clay specimen is not confined and the build-up of swelling pressure inside the clay structure during pore water saturation results in the disintegration of the clay specimen. Such unwanted effect can be minimized by using only small clay cylinders with diameters in the mm range in combination with stabilization of the clay specimen by epoxy embedding, as reported by Van Loon *et al.* (2014)[46].

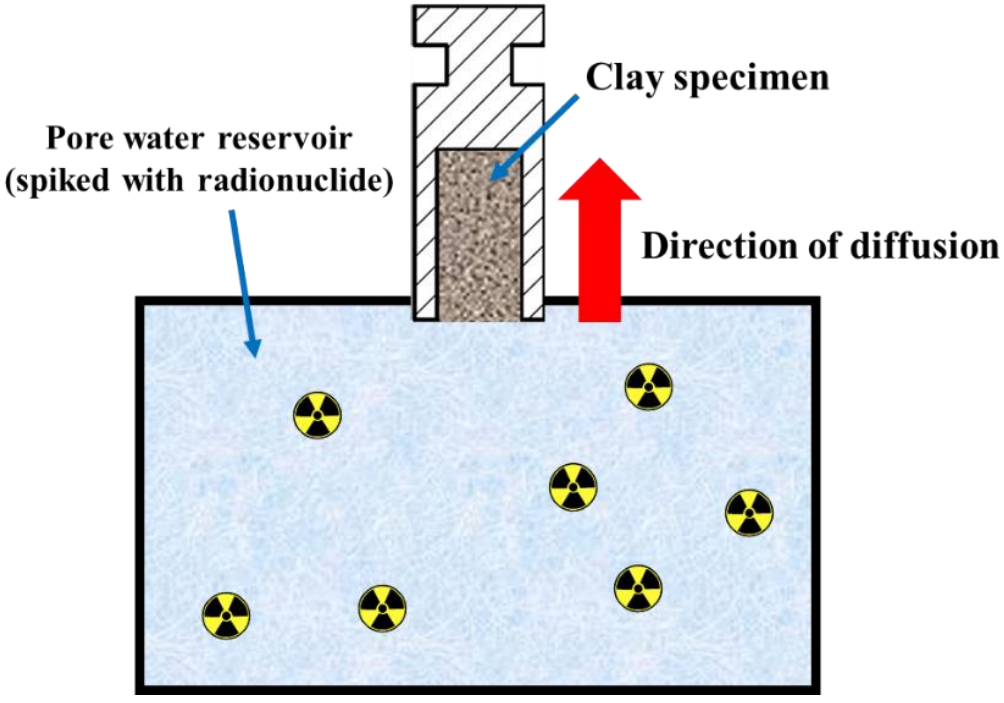

Fig. 15 Experimental setup for in-diffusion experiment (adopted from Van Loon *et al.* (2014)[46]).

3.3.5 Summary

Although somewhat challenging with regard to sample preparation, the in-diffusion method appears to be the most promising for the investigation of the diffusion of both the strongly sorbing cationic Am(III) species $[Am(CO_3)]^+$ and the moderately sorbing U(VI) species $Ca_2UO_2(CO_3)_3$ (aq.), involving trace to ultra-trace levels of such actinide nuclides. Unwanted tracer sorption onto components, as well as a lengthy equilibration time are minimized, while D_e, K_d, and D_a are still accessible from the same experiment. The actual design of the experimental setup in the frame of this PhD thesis will be described in detail in sub-chapter 5.6.

4 Accelerator Mass Spectrometry (AMS)

4.1 Introduction

The development of accelerator mass spectrometry (AMS) started in the 1970s with emphasis on the measurement of ^{14}C for radiocarbon dating in the field of archaeology.[64] In the subsequent years, the application of AMS was considerably extended to other research fields, like geology, astrophysics, and environmental sciences. Today, AMS is one of the most sensitive analytical techniques available for the determination of rare long-lived radionuclides in environmental samples, such as ^{36}Cl, ^{41}Ca, ^{99}Tc, ^{129}I, $^{233,236}U$, ^{237}Np, and $^{239–242}Pu$.[65–71]

The overall efficiency for the determination of actinides with AMS is approximately 10^{-4}, as reported by Winkler *et al.* (2015).[72] This means that, on average, out of 10^4 atoms in the analyte, one atom reaches the detector. The main determinants for such overall sensitivity are the ionization yield in the ion source, the stripping yield in the tandem accelerator, and the detection efficiency (see more in sub-chapter 4.2). Despite the rather low overall efficiency, AMS is an exceptionally sensitive technique for the determination of actinides, thanks to extremely low abundance sensitivities down to 10^{-14}, as reported by Steier *et al*. (2019)[73] for the determination of ^{236}U in the presence of the abundant isotope ^{238}U. Such sensitivity allows for the analysis of very small samples in the range of mg and in presence of naturally occurring ^{238}U.[74] AMS represents a powerful alternative to radioactive decay measuring techniques, since radionuclides with long half-lives (e.g., $t_{1/2}(^{236}U) = 2.34 \times 10^7$ a) have low specific activities, resulting in very few radioactive decays and, thus, low counting statistics. It also complements conventional mass spectrometric techniques, such as inductively coupled plasma–mass spectrometry (ICP–MS), where the attainable abundance sensitivity is many orders of magnitude higher ($^{236}U/^{238}U = 10^{-7}$).[75] The extremely high sensitivity of AMS is also achieved by the strong suppression of molecular isobars (see sub-chapter 5.7.1). The limit of detection (LOD) for the AMS determination of actinides can be as low as 2×10^{-20} mol per sample, as reported by Steier *et al*. (2009).[74] In the presence of clay matrix (OPA, COx), the actinides U, Np, Pu, Am, and Cm can be accurately determined down to approximately 10^{-11} mol/m³, as reported by Glückman *et al.* (2022).[16]

In a simplistic way, AMS can be described as two separate mass spectrometers for mass discrimination, which are connected by a tandem accelerator for the destruction of molecular isobars. At the beginning of the beamline, there is an ion-source, sputtering the analyte, while

at the end a particle detector performs nuclide quantification via ion counting. An in-depth explanation of the working principle of AMS is given in the next sub-chapter.

4.2 Working principle

All measurements in the frame of this PhD study were carried out at the Vienna Environmental Research Accelerator (VERA),[73] located at the Faculty of Physics of the University of Vienna, in Austria. Unless mentioned otherwise, all explanations in the upcoming paragraphs are given based on the AMS setup of VERA, which is depicted in **Fig. 16**.

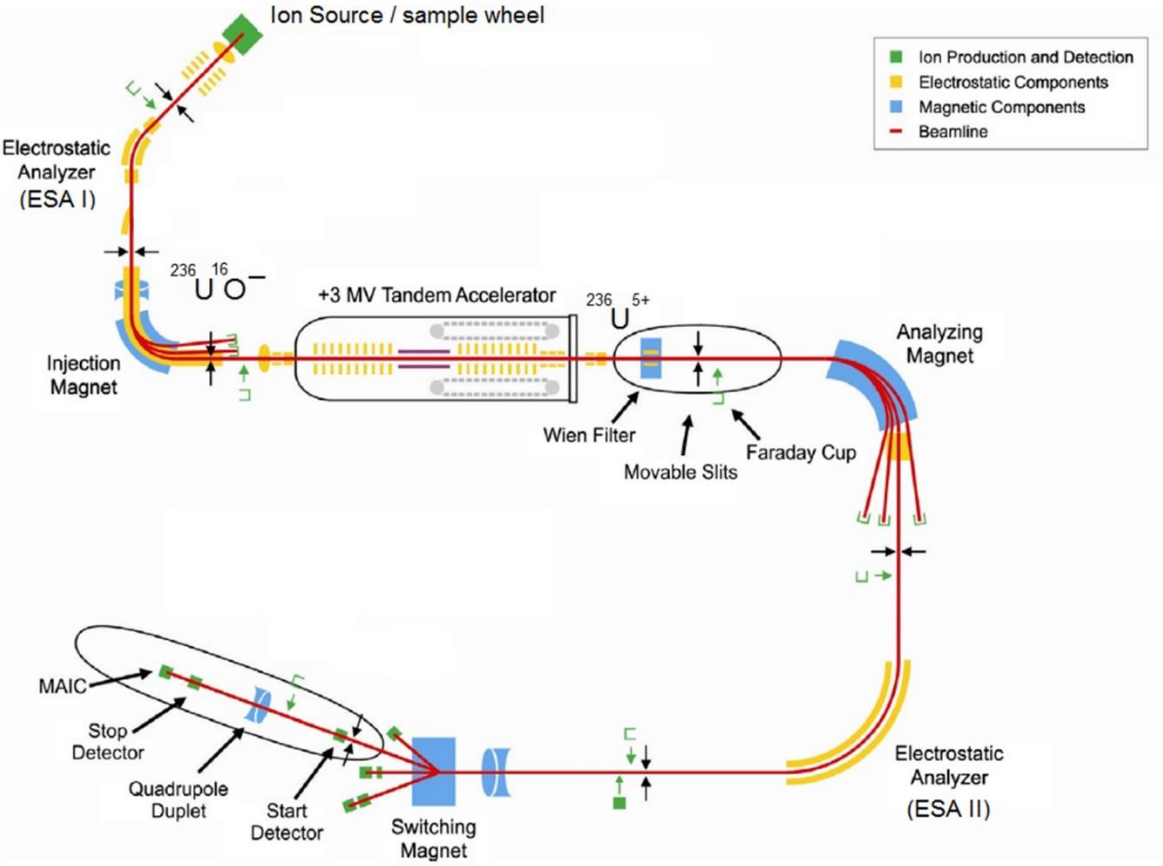

Fig. 16 Overview of the AMS beamline at VERA (adopted from Winkler *et al.* (2015)[72]).

4.2.1 Cs sputter negative ion source

The ion source contains the solid samples which are pressed into aluminum sample holders, called sample cathodes or AMS targets. Such cathodes are mounted on a sample wheel, which can accommodate up to 40 sample cathodes (**Fig. 17**). The ion source is equipped with a reservoir of elementary cesium which is heated up in order to produce cesium vapor which is ionized by means of a hot molybdenum or tantalum ionizer (≈ 1100 °C), yielding in Cs^+ ions and free electrons (**Fig. 18**).[76] Since the sample cathode is kept on a negative potential of 5–

15 kV relative to the ionizer, the Cs^+ cations are accelerated toward the sample, resulting in the sputtering of the analyte. During sputtering, a fraction of the analyte atoms is released from the sample matrix as negatively charged molecular anions. In the case of actinides, less than 1 % of the analyte is ionized, yielding in anionic species, usually of the form of mono-oxide anions AnO^- (e.g., $^{236}U^{16}O^-$). The sputtered molecular anions are repelled by the negative potential of the sample cathode and are accelerated towards an extraction hole. After exiting the ion source, further acceleration ("pre-acceleration") is performed through a potential of 75 kV before reaching the first electrostatic analyzer ESA I (**Fig. 16**). Typically, a sample can be sputtered for several hours, before the analyte is consumed.

Fig. 17 Pictures of aluminum sample cathode (left) and sample wheel holding up to 40 sample cathodes (right).

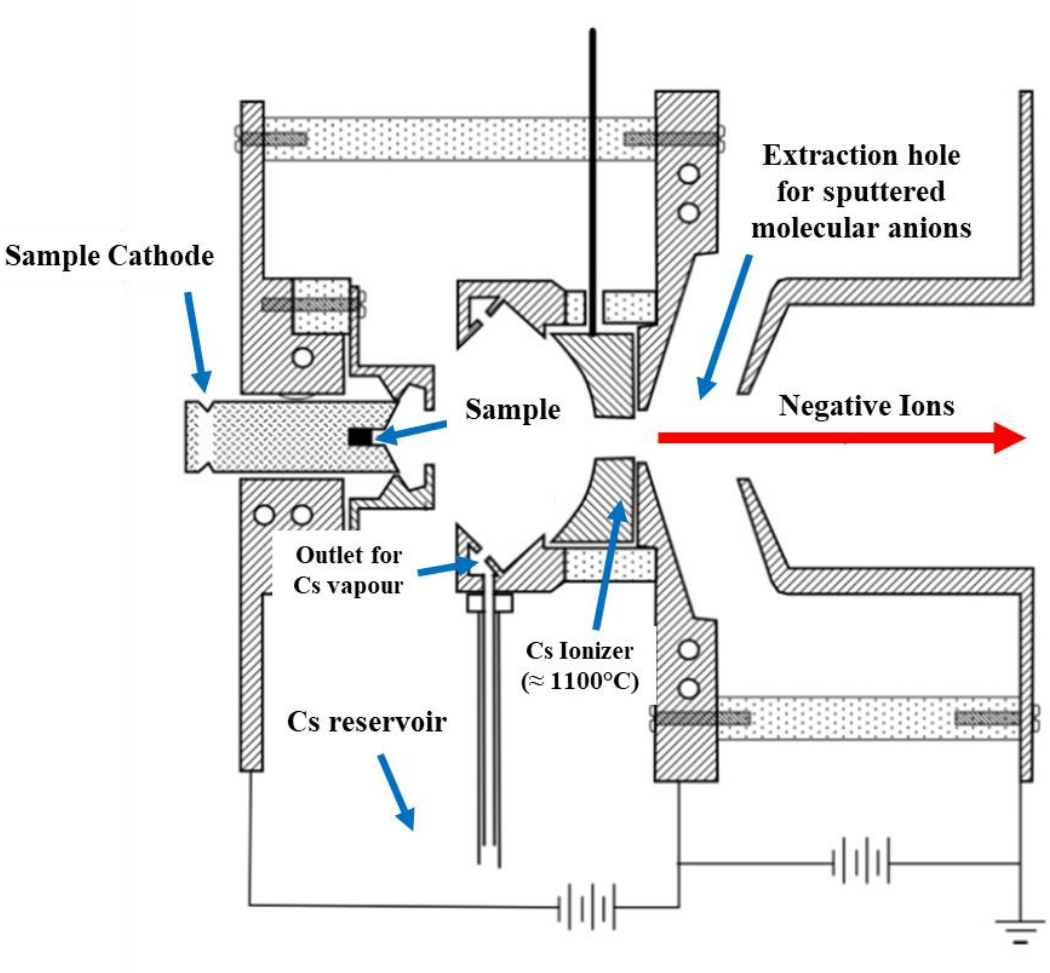

Fig. 18 Drawing of a Cs sputter negative ion source suitable for AMS (adopted from Vogel (2013)[77]).

4.2.2 Low-energy injection system

The first component of the low-energy side mass spectrometer is the electrostatic analyzer (ESA I) which provides a first selection of the anions based on their energy.

ESA I is featured by a pair of spherical electrodes, across which an electric field is applied (maximum electric field strength 6 kV/cm), deflecting incoming molecular anions by 45°.[78] The energy selection is based on the equilibrium between the electric force F_{el} and the centrifugal force F_{cf}, which can mathematically be described with **Eq. 11**:

$$F_{el} = F_{cf} = q \cdot \vec{E} = \frac{m \cdot v^2}{r} \qquad \textbf{Eq. 11}$$

where q [C] is the electric charge of the anion, $\vec{E}$ [kV/cm] is the electric field strength, m [kg] is the mass of the anion, v [m/s] is the velocity of the anion, and r [m] is the radius of ESA I.

For fixed $\vec{E}$ and r — as defined by ESA I — only anions with a distinct E/q ratio can pass the analyzer:

$$\vec{E} \cdot r = \frac{m \cdot v^2}{q} = \frac{2 \cdot E}{q} \qquad \textbf{Eq. 12}$$

where E [eV] is the energy of the anion.

Anions with the selected energy leave ESA I and enter the injection magnet which allows for further selection, based on the anion´s charge. The injection magnet bends the ion beam by 90°, which is only stable, if magnetic force F_B and centrifugal force F_{cf} are in equilibrium:

$$F_B = F_{cf} = q \cdot v \cdot \vec{B} = \frac{m \cdot v^2}{r} \qquad \textbf{Eq. 13}$$

where $\vec{B}$ [A/m] is the magnetic field strength. For fixed $\vec{B}$, only anions with a distinct m/q ratio are selected by the injection magnet.

4.2.3 Tandem accelerator

The injected anions enter the tandem accelerator which operates under SF_6 atmosphere with a pressure of approximately 6 bar.[78] Two charging chains generate a positive voltage of up to 3 MV, by which the anions are further accelerated. In the center of the tandem accelerator the anions reach a gas-filled stripper, in which the anions collide with Helium atoms, resulting in the loss of electrons. Once enough electrons are stripped of a molecular anion, the positively charged nuclei of the molecular anion start repelling each other, ultimately leading to the cleavage of the bond in a process known as coulomb explosion. In this way, all molecular anions are destroyed and converted into a wide range of highly charged mono atomic cations.[72] The positive voltage inside the tandem accelerator causes further acceleration of the atomic cations up to MeV energies. The exact energy of such cations can be calculated with **Eq. 14**:

$$E_+ = \left(E_{inj} + e \cdot U_T\right) \cdot \frac{M_+}{M_{inj}} + q \cdot e \cdot U_T \qquad \textbf{Eq. 14}$$

where E_+ [eV] is the energy of the cation obtained after stripping, E_{inj} [eV] is the energy of the injected anion, e [C] is the charge of the electron, U_T [V] is the terminal voltage of the tandem

accelerator, M_+ [u] is the atomic mass of the cation obtained after stripping, and M_{inj} [u] is the mass of the injected molecular anion.

In a routine protocol for actinide analysis a terminal voltage of +1.65 MV is applied and cations in the 3+ charge state are selected for further transmission through the beamline. Cations with q = 3+ are generated at fairly high yield (≈ 20 %) and assure the best possible detection efficicency.[72] Such combination of terminal voltage and cation charge state allows for an m/q ratio of the cation suitable for the high-energy analyzing system, which is described in the next sub-chapter.

4.2.4 High-energy analyzing system & particle detector

The high-energy side mass spectrometer has the purpose of selecting the incoming mono-atomic cations, similar as the low-energy side mass spectrometer for the anions. The first selection is performed by a 90° analyzing magnet, based on the cation´s m/q ratio. The second electrostatic analyzer (ESA II) performs the final selection based on the cation´s E/q ratio.

The selected cations are directed to a Bragg-type ionization chamber, installed as particle detector at the end of the beamline. It is filled with isobutane gas as counting gas at a pressure of approximately 70 mbar. The detector measures the energy of the cations as function of gas ionization. In detail, cation identification is performed by selecting energy signals with pulse width and height corresponding to the cation´s atomic mass and charge. The collected energy signals can be visualized in a pulse plot. Such pulse plot is shown in **Fig. 19** for the counting of $^{243}Am^{3+}$. The region of interest (ROI) is highlighted as a red box and contains signals corresponding to m = 243 u and q = 3+. Despite the filtering of species with wrong m/q ratios, nuclides with lower m and q, but correct m/q ratio can still reach the detector (events shown in orange box in **Fig. 19**). In rare cases, such nuclides can also contribute to so-called pile-up events. For example, when two nuclides with m = 162 u and q = 2+ are reaching the detector during a time interval, smaller than the dead time of the detector, an event of m = 243 u and q = 3+ will arise in the ROI, resulting in the overestimation of ^{243}Am.

In order to take into account the detector´s dead time, a pulser is regularly sending a digital signal at a specific frequency to the detector. Signals from the pulser arrive in the right part of the pulse plot (events shown in green box in **Fig. 19**).

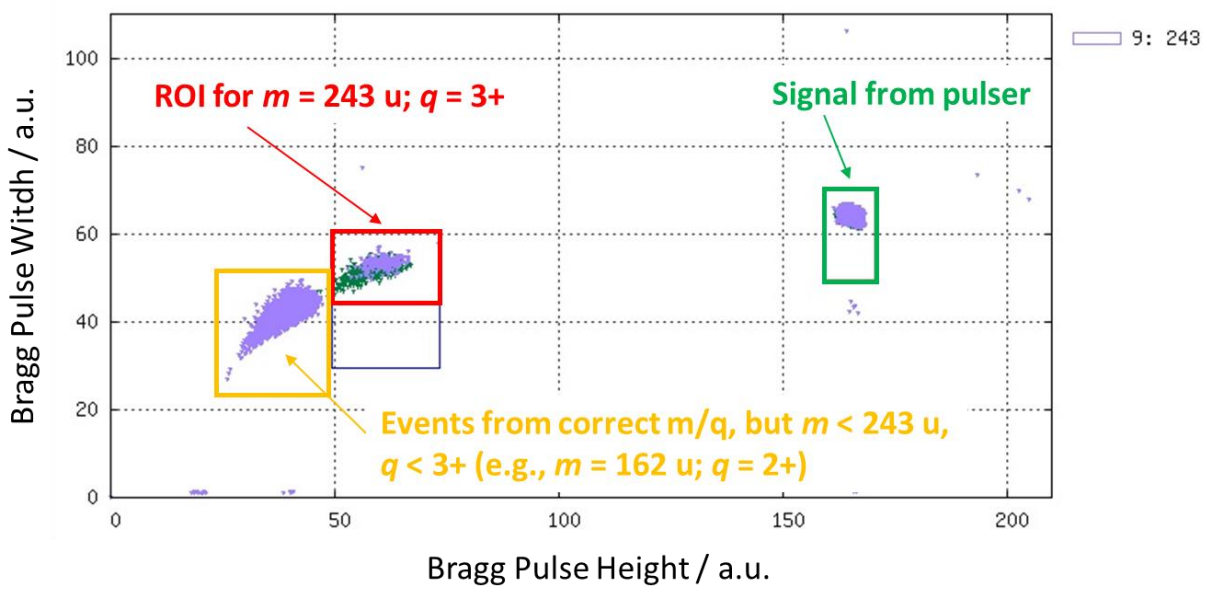

Fig. 19 Pulse plot for detection of energy signals for incoming $^{243}Am^{3+}$. Pulse width on the y-axis and pulse height on the x-axis. Signals of $^{243}Am^{3+}$ are shown in the red box, counting events rom cations with lower *m* and *q* in orange box, and signals from the pulser in the green box.

4.3 Principle of measurement and data evaluation

Since actinides are routinely measured at VERA, there are well established measurement analysis protocols available. In the following, the reader should be given a basic overview of the measurement process, data collection, and data evaluation.

4.3.1 Tuning and calibration of beam

In order to achieve the best possible sensitivity, the ion-optical components of the beamline need to be tuned for maximum ion transmission prior to the measurement of real samples. At VERA, this is usually done with tuning samples of the uranium containing in-house standard "Vienna-KkU", with a known $^{236}U/^{238}U$ ratio of $(6.98\pm0.32) \times 10^{-11}$.[79] Vienna-KkU is expected to be free of anthropogenic ^{236}U, since it originates from U_3O_8 which was mined at the uranium ore of Joachimsthal (today Czech Republic) in pre-nuclear times (between 1910 and 1918).

Due to its abundancy, ^{238}U cannot be analyzed by ion counting in the particle detector, since the incoming cations would cause saturation of the detector. Therefore, at the low-energy side, between injection magnet and tandem accelerator, the $^{238}U^{16}O^-$ anions generated during the sputtering step are directed to a first set of Faraday cups (**Fig. 16**), where the current induced by $^{238}U^{16}O^-$ is determined, which is usually in the range of nA. A second set of Faraday cups is located at the high-energy side, directly after the analyzing magnet, where the cationic species (i.e., $^{238}U^{3+}$) are detected. By comparing the current of $^{238}U^{16}O^-$ obtained at the low energy side

with that of $^{238}U^{3+}$obtained at the high energy side, nuclide transmission and stripping yields can be determined. Tuning samples are also measured periodically between regular samples in order to monitor the beamline performance.

In order to account for matrix-induced variations of analyte sputtering and ionization, usually also calibration samples are being measured. These are samples which contain the exact same matrix, as the real samples, spiked with a known amount of both the analyte nuclide and the nuclide used as internal standard.

4.3.2 Internal standardization

In order to quantify the content of the actinide nuclide of interest, the sample has to be spiked with a known amount of another actinide nuclide, acting as internal standard. In this way, all potential losses occurring over the entire course of the analytical procedure, both during chemical preparations and during AMS analysis, can be taken into account.

There are two types of internal standards used for AMS analysis, namely isotopic (e.g., quantification of ^{236}U with ^{233}U as internal standard)[80] and non-isotopic tracers. The use of the latter is necessary, when an isotopic tracer is not available, for instance, due to the lack of a sufficient degree of isotopic purity. Such choice of tracer is reported in a study from Quinto *et al*. (2015),[80] where ^{242}Pu was used as non-isotopic tracer for the determination of ^{237}Np.

When performing AMS analysis of a nuclide using an isotopic tracer, the ionization yields (i.e., fraction of a nuclide in the AMS target that is sputtered as negative ions in the ion source) of both analyte and tracer nuclide are the same. However, it was observed in previous studies[15,81,82] that different actinides do not exhibit the same ionization yield in the ion source. Generally, these studies revealed that the ionization yield increases with the atomic number of the actinide element. For the correction of such phenomenon, chemical-ionization-yield (CIY) factors have to be determined. Besides the ionization yield, the CIY factor also accounts for the chemical yield, indicating the fraction of a nuclide recovered after the several steps of chemical preparation, such as an $Fe(OH)_3$ co-precipitation. Since within an AMS measurement it is not possible to discriminate between ionization yield and chemical yield, the CIY factor is employed, representing the combination of both phenomena.

The CIY factor can be expressed with the formula in **Eq. 15**, shown for the example of ^{237}Np and ^{242}Pu:

$$\mathrm{CIY}\left(\frac{^{237}\mathrm{Np}}{^{242}\mathrm{Pu}}\right) = \frac{\mathrm{ctr}(^{237}\mathrm{Np})/\mathrm{ctr}(^{242}\mathrm{Pu})}{N(^{237}\mathrm{Np})/N(^{242}\mathrm{Pu})} \qquad \textbf{Eq. 15}$$

where ctr [s^{-1}] is the count rate (i.e., counting events per time) N [–] is the nominal number of atoms of the corresponding actinide nuclide. The ctrs of analyte and tracer nuclide are obtained from the analysis of calibration samples, described in sub-chapter 4.3.1.

4.3.3 Background

In the frame of every analytical technique it is indispensable to perform blank measurements, in order to account for potential background, biasing the quantification of the analyte. Sources of background can occur during sample preparation (e.g., chemicals, laboratory contamination) or during the AMS analysis itself, for example due to contamination of the ion source, which leads to cross-talk.

In order to minimize the risk of background during sample preparation, whenever possible, ultra-pure grade reagents shall be used. Furthermore, particular care has to be taken in using clean, pre-treated laboratory equipment, such as tubes and vessels. This is especially important, when it comes to the analysis of rare, long-lived actinides originating from global fallout, such as ^{236}U and ^{239}Pu.[71,83] A proper interpretation of background requires blank samples which are made of the same starting material, contain the same matrix and undergo the same chemical treatment, as the real samples. Such blank samples are called procedural blanks. At VERA, additionally, also instrumental blank samples are measured. These are samples containing an iron-graphite mixture, prepared in the VERA laboratories, which may be analyzed prior to the real samples for all masses of interest. In this way, potential background originating from the ion source can be identified separately from the background of the procedural blanks. In the present study, background levels were determined as average of three to five individual blank samples (see **Tab. 20** and **Appendix A**), with uncertainties given as 2 σ confidence intervals.

4.3.4 Measurement procedure

In the following, the basic procedure of an AMS measurement will be explained with the example of ^{236}U determination and the use of ^{233}U as isotopic tracer. After tuning of the beam, as described in sub-chapter 4.3.1, the analysis of real samples, blank samples, and calibration samples is initiated.

The complete measurement of all sample cathodes on the sample wheel is called a “turn”, i.e., one turn of the sample wheel. Each nuclide in a sample cathode is measured in a pre-defined order, which is called a “sequence”. The measurement time [s] for a specific nuclide within a sequence is called “cycles”, where, for instance, cycles = 30 represents a measurement time of 30 s. The number of repetitions of sequences is defined by the number of “runs per turn”. The total measurement time t_m [s] is obtained by multiplying the numbers of turns, runs per turn, sequences, and cycles. For instance, in the case of 10 turns, 2 runs per turn, 5 sequences, and 30 cycles, t_m is 10 × 2 × 5 × 30 s = 3000 s.

Depending on the nuclide content and the resulting counting statistics, t_m is adjusted during the measurement accordingly. Typical t_m are in the range of several minutes to an hour. It shall be noted that a longer t_m also results in a longer sputtering time, hence a more rapid consumption of the sample material. This can pose a limitation, when multiple nuclides must be sequentially determined from the same sample.[80]

In order to obtain a ctr, the number of counts (cts [–]) must be divided by t_m, as shown for the ctr of ^{236}U in **Eq. 16**:

$$\mathrm{ctr}\left(^{236}\mathrm{U}\right) = \frac{\mathrm{cts}\left(^{236}\mathrm{U}\right)}{t_\mathrm{m}} \qquad \textbf{Eq. 16}$$

The number of counts represents such counting events, which were collected in the ROI (see sub-chapter 4.2.4, **Fig. 19**). t_m is pre-selected according to the expected nuclide content of a sample, but can be adjusted during the beam time if necessary. The number of counts is subject to statistical uncertainty, which obeys the Poisson distribution and is, thus, called Poisson uncertainty of the number of counts (σ_{cts} [–]). It is estimated according to:

$$\sigma_\mathrm{cts} = \sqrt{\mathrm{cts}} \qquad \textbf{Eq. 17}$$

In order to determine the statistical uncertainty of the ctr (σ_{ctr}), the uncertainty of the number of counts (σ_{cts}) has to be divided by t_m:

$$\sigma_\mathrm{ctr} = \frac{\sigma_\mathrm{cts}}{t_\mathrm{m}} \qquad \textbf{Eq. 18}$$

The quantification of ^{236}U (i.e., the determination of the number of ^{236}U atoms in the sample) is done by normalization of ctr(^{236}U) to the ctr of the internal standard (ctr(^{233}U)), according to **Eq. 19**:

$$N\left(^{236}\mathrm{U}\right) = \frac{\mathrm{ctr}\left(^{236}\mathrm{U}\right)}{\mathrm{ctr}\left(^{233}\mathrm{U}\right)} \cdot N_0\left(^{233}\mathrm{U}\right) \qquad \textbf{Eq. 19}$$

where N(^{236}U) [–] is the number of ^{236}U and N_0(^{233}U) [–] is the known amount of the added internal standard ^{233}U.

5 Materials and methods

5.1 Chemicals and actinide tracers

All solutions used in the experiments as well as for the cleaning of vessels were prepared with ultra-pure water (MQ water) from a Milli-Q® Advantage A10 water purification system (18.2 MΩ·cm (22±1) °C; Merck Millipore, Darmstadt, Germany). An overview of the chemicals used in this work is given in **Tab. 8**.

Tab. 8 Chemicals used in this work.

Name	Chemical formula	Manufacturer	Grade
Ammonia (25 %)	NH_3	Merck, Darmstadt, Germany	Suprapur®
Calcium chloride dihydrate	$CaCl_2 \cdot 2\ H_2O$	Merck	a.g. (analytical grade)
Ethanol (≥ 99.8 %)	C_2H_6O	VWR International, Darmstadt, Germany	NORMAPUR®
Hydrochloric acid (34 %)	HCl (aq.)	Roth, Karlsruhe, Germany	Rotipuran® Ultra
Iron powder (99.99 %)	Fe	Alfa Aesar™, Fisher Scientific, Schwerte, Germany	a.g.
Magnesium chloride hexahydrate	$MgCl_2 \cdot 6\ H_2O$	Merck	a.g.
Nitric acid (69 %)	HNO_3	Roth	Rotipuran® Ultra
Potassium chloride	KCl	Merck	a.g.
Sodium azide	NaN_3	Merck	a.g.
Sodium bicarbonate	$NaHCO_3$	Merck	a.g.
Sodium chloride	NaCl	Merck	a.g.
Sodium hydroxide	NaOH	Merck	a.g.
Sodium sulfate	Na_2SO_4	Merck	a.g.
Strontium chloride hexahydrate	$SrCl_2 \cdot 2\ H_2O$	Merck	a.g.

For the diffusion experiments, ^{233}U(VI) and ^{243}Am(III) were utilized as diffusing tracers. ^{236}U and ^{248}Cm were used as internal tracers for AMS analysis. For this, stock solutions of ^{233}U

(reference material IRMM-040a), ^{236}U (reference material IRMM-3660a), and in-house solutions of ^{243}Am and ^{248}Cm, respectively, were diluted with 2 % HNO_3 as required. Detailed information about the actinide tracer stock solutions and their respective dilutions are given in **Appendix B**.

5.2 Opalinus Clay (BLT-14)

For the diffusion experiments, bore core pieces of OPA (shaly facies) from the Mont Terri URL were used. The bore core BLT-14, received in January 2007, was drilled parallel to the bedding. The bore hole is located near the northern end of Gallery 98 (**Fig. 20**).[84] The bore core pieces were stored under Ar atmosphere and further processed to diffusion sample size at KIT-INE. Small cylindrical OPA samples were prepared according to the following procedure: A piece of OPA bore core BLT-14 of approximately 100 × 50 mm (**Fig. 21**), stored under Ar atmosphere, was cut into smaller pieces by means of a stainless steel saw under aerobic conditions. These pieces were placed into a turning lathe and processed in the direction parallel to the clay rock´s bedding until the desired diffusion sample length of 10 mm and diameter of 6 mm was reached (**Fig. 23a**).

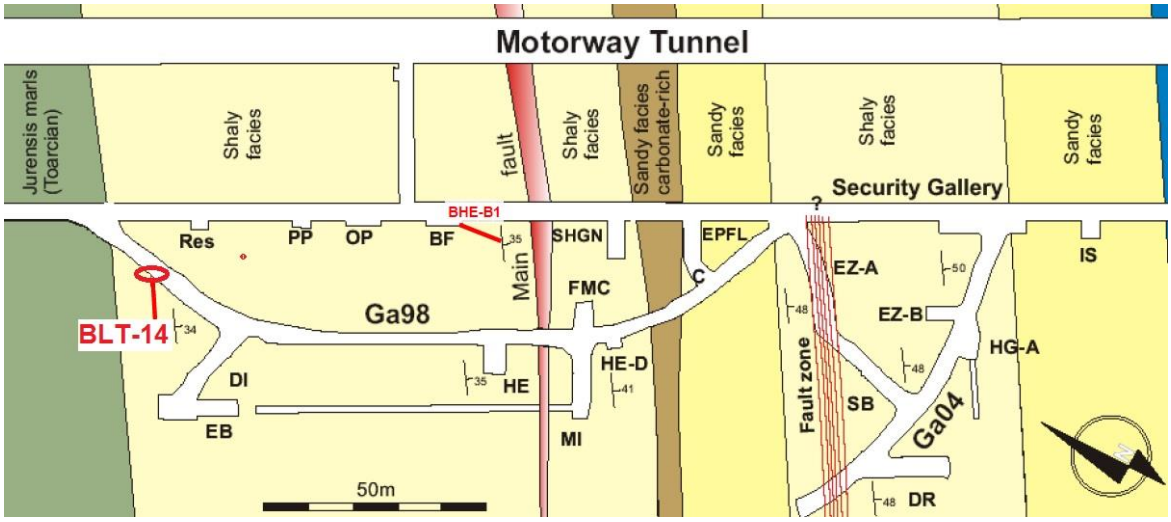

Fig. 20 Location of borehole BLT-14 at the Mont Terri URL (adopted from Gräsele and Plischke (2007)[84]).

Fig. 21 Piece of OPA bore core BLT-14, red arrow indicating the orientation of bedding.

5.3 Synthetic pore water

Synthetic OPA pore water was prepared according to the composition published in Gimmi *et al.* (2014)[1] (**Tab. 9**). The elemental composition of the pore water was confirmed with ICP–MS and ion chromatography (IC) prior to the diffusion experiments. In order to prevent bacterial growth, NaN_3 was added to the pore water resulting in a concentration of 1×10^{-3} mol/L.

Tab. 9 Composition, pH, and *I* of synthetic OPA pore water at 25 °C according to Gimmi *et al.* (2014).[1]

Ion	Concentration / (mol/L)
Na^+	1.48×10^{-1}
K^+	1.40×10^{-3}
Mg^{2+}	1.14×10^{-2}
Ca^{2+}	8.68×10^{-3}
Sr^{2+}	4.98×10^{-4}
SO_4^{2-}	8.80×10^{-3}
Cl^-	1.70×10^{-1}
CO_3^{2-}/HCO_3^-	2.72×10^{-3}
I	0.22
pH	7.24
θ / °C	25

5.4 pH measurements

pH values were determined with a laboratory pH meter (Orion™ 920A, Thermo Fisher Scientific, Schwerte, Germany) and a semi-micro pH electrode (Orion™ 8103BN ROSS™, Thermo Fisher Scientific, Schwerte, Germany). Calibration was performed at 25 °C with standard buffers (NIST standard, Merck, Darmstadt, Germany) at pH 4, 7, and 9.

5.5 E_h measurements

Redox potentials were measured using a combined Pt ring electrode with a Ag/AgCl reference electrode and KCl (3 mol/L) as electrolyte (Metrohm Schweiz AG, Zofingen, Switzerland).

5.6 Experimental details on diffusion experiments

5.6.1 Diffusion reservoir and diffusion sample holder

Due to the expected short diffusion distances of the actinide tracers, an in-diffusion-setup was chosen in this study. The design of the diffusion reservoir and its components was adopted from Dahler (2018)[85] and Zeisel (2018)[86] and is depicted in **Fig. 22a,b**. It consisted of a vessel (1), a

lid with two holes for pore water sampling and pH measurements (2), and a cross with rails (3) accommodating the sample holders (4). All parts were made of PMMA for better visibility. The vessel was designed for a pore water capacity of 420 mL. The sample holder (**Fig. 22c,d**) was designed for the insertion of a cylindrical clay sample with 10 mm length and 6 mm diameter. All cell components, including the sample holders, were cleaned thoroughly with dishwashing liquid, in order to remove oil and other organics originating from the manufacturing process. Afterwards, all parts were immersed in MQ water for 2 d. Finally, all parts were transferred to an glovebox (Ar atmosphere) and rinsed with synthetic OPA pore water (see sub-chapter 5.3).

The cylinders (**Fig. 23a**) were glued to caps of Zinsser vials (Polyvials®, HD-PE, Zinsser Analytics, Germany) with instant glue (LOCTITE 401, Henkel AG & Co. KGaA, Düsseldorf, Germany), as shown in **Fig. 23b**. After 1 h, the clay samples were embedded into the PMMA sample holders with epoxy resin (Epofix, Struers GmbH, Germany). Epoxy resin and hardener were gravimetrically mixed in a 25:3 ratio and stirred on a magnetic stirrer at 250 rpm for 5 min. The mixture was left for 20 min in order to yield a good separation from air bubbles. To each sample holder a few drops of epoxy resin were added. Immediately, the clay samples were gently combined with the sample holders (**Fig. 23c**). The Zinsser vial caps ensured that the clay samples were oriented plano-parallel inside the sample holder. Overflowing resin was quickly wiped off. Hardening time of the resin was 24 h. Subsequently, the Zinsser vial caps were removed by gently breaking them off. The clay samples were covered by a thin layer of resin and instant glue. This layer was abraded with abrasive paper of grit number P600 (Abrasive paper (SiC) waterproof Matador, P600, Hoffmann Supply Chain GmbH, Nürnberg, Germany) until the clay surface was exposed (**Fig. 23d**).

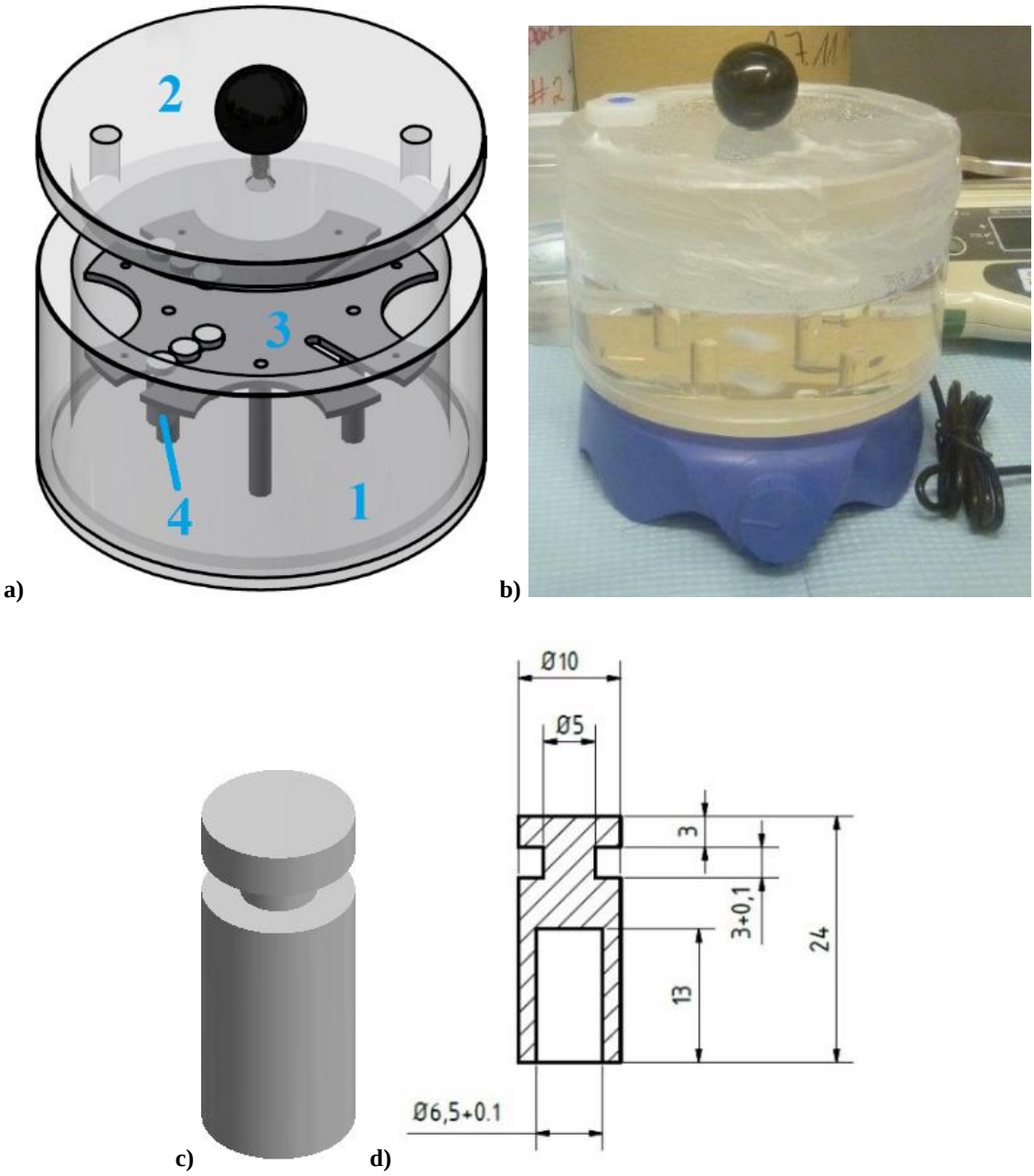

Fig. 22 **a)** Drawing of diffusion reservoir with components: vessel (1), lid (2), cross with rails (3), sample holder for cylindrical OPA samples (4), **b)** picture of diffusion reservoir, during the diffusion experiment, the lid was wrapped with parafilm for reduction of pore water loss, **c)** drawing of sample holder for cylindrical OPA samples, **d)** technical drawing of sample holder.

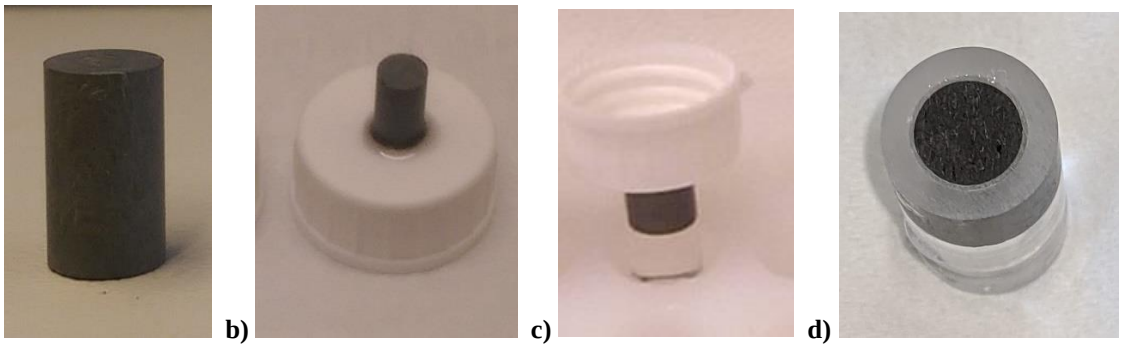

Fig. 23 **a)** Cylindrical OPA sample, **b)** sample glued to Zinsser vial cap, **c)** sample immersed into epoxy resin inside PMMA sample holder, **d)** embedded sample in PMMA sample holder.

5.6.2 Equipment sorption test

Four cylindrical vessels, made of PMMA, were cleaned with 10 % HCl, followed by rinsing with MQ water and OPA pore water. Subsequently, all vessels were filled with 40 mL of OPA pore water. Two of the vessel solutions were spiked with 2 µL of a 1.00×10^{-4} mol/L solution of ^{233}U(VI) and 31 µL of a 1.30×10^{-5} mol/L solution of ^{243}Am(III), resulting in initial concentrations of $(5.02 \pm 0.15) \times 10^{-9}$ mol/L and $(1.00 \pm 0.06) \times 10^{-8}$ mol/L of ^{233}U(VI) and ^{243}Am(III), respectively. The other two vessel solutions were not spiked and acted as blank samples. Finally, all vessel solutions were adjusted to a pH of 7.2±0.1 by the addition of 0.1 mol/L HCl.

The vessel solutions were sampled by taking 50 µL of pore water 2 h, 10 d, 17 d, 41 d, and 56 d after tracer addition and diluted 1:250 with 2 % HNO_3. Subsequently, the diluted solutions were analyzed for ^{233}U and ^{243}Am concentrations with SF–ICP–MS. pH values of all vessel solutions were checked after 2 h, 17 d, and 56 d.

5.6.3 Diffusion experiments

In total, four diffusion experiments were conducted with experimental times of 126 d (experiment I), 240 d (experiment II), 20 d (experiment III), and 36 d (experiment IV). Experiments I and II, as well as experiments III and IV, were carried out in a shared diffusion reservoir, respectively. All diffusion experiments were performed under Ar atmosphere. Oxygen concentrations were < 0.1 ppm during experiments I and II and 21–39 ppm during experiments III and IV.

The diffusion reservoir was conditioned for 56 d (experiments I and II) or 32 d (experiments III and IV) with 420 mL of pore water, spiked with 21 µL of a 1×10^{-4} mol/L solution of ^{233}U(VI) and 313 µL of a 1.3×10^{-5} mol/L solution of ^{243}Am(III). This resulted in reservoir solution concentrations of 5.02×10^{-9} mol/L of ^{233}U(VI) (experiments I and II) or $(4.35\pm0.30)\times10^{-11}$ mol/L of ^{233}U(VI) (experiments III and IV) and 1.01×10^{-8} mol/L of ^{243}Am(III) (experiments I and II) or $(1.78\pm0.14)\times10^{-11}$ mol/L of ^{243}Am(III) (experiments III and IV), respectively. The pH was re-adjusted to 7.3±0.1 by addition of 150 µL of 0.1 mol/L HCl. The pH was checked once more at the end of conditioning after 53 d (experiments I and II) or 32 d (experiments III and IV). The mixture was stirred at 250 rpm with a magnetic stirrer (COLOR SQUID IKAMAG, IKA-Werke GmbH & CO. KG, Staufen, Germany) during the entire experiment. In a separate centrifuge tube ("saturation vessel") (Sarstedt AG & Co. KG, Nümbrecht, Germany), four cylindrical OPA samples were saturated in 50 mL of synthetic pore water. Saturation was performed for 56 d (experiments I and II) or 60 d (experiments III and IV), ensuring a complete filling of the pore structure of the clay with pore water.[46] The pH of the saturation vessel solution was checked 2 h after contacting the clay samples with pore water and at the end of saturation (56 d or 60 d).

The diffusion experiment was initiated by immersing two of the four saturated clay samples 2 mm into the diffusion reservoir solution, as depicted in **Fig. 24**. In parallel, the remaining two clay samples were kept in the saturation vessel for the later use as procedural blanks and calibration samples. The diffusion reservoir solution was sampled after 2 h, 10 d, 17 d, 38 d, and 56 d of conditioning (experiments I and II) or after 2 h, 10 d, and 32 d of conditioning (experiments III and IV). Furthermore, the diffusion reservoir solution was sampled after 57 d, 71 d, and 126 d of diffusion (experiments I and II) or after 15 d, 20 d, and 36 d of diffusion (experiments III and IV). The saturation vessel solution was sampled directly before and 2 h, 56 d, and 126 d after contacting with the clay samples. Samplings were performed by taking 25 µL for tracer and cation analysis with ICP–MS and 500 µL for anion analysis with ion

chromatography (IC). In the case of diffusion experiments III and IV, dissolved inorganic carbon contents (DIC) (i.e., HCO_3^-/CO_3^{2-} concentrations) were determined in the respective saturation vessel solution by taking an aliquot of 7 mL. After each diffusion experiment, one of the clay diffusion samples from the diffusion reservoir and one of the procedural blank samples from the saturation vessel was removed and dried for 15 min under Ar atmosphere. Subsequently, the samples were processed for U and Am diffusion profile analysis.

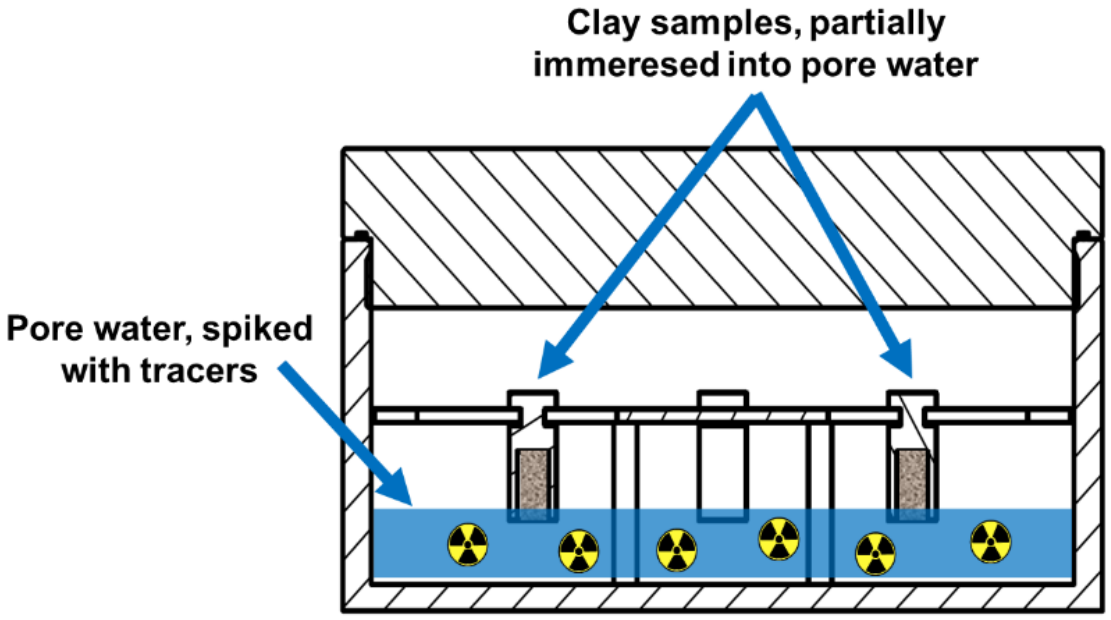

Fig. 24 Illustration of diffusion reservoir of experiments I (126 d) and II (240 d), with two clay samples partially immersed into the pore water solution, spiked with the diffusing tracers ^{233}U(VI) and ^{243}Am(III).

5.6.4 Abrasive peeling

For the determination of diffusion profiles in the clay samples, the technique of abrasive peeling was applied.[46,87] In order to minimize the risk of cross-contamination between abraded clay layers, it was decided to abrade the clay diffusion sample from the distal side (i.e., in the direction of increasing tracer concentration). For this, a PMMA cylinder (13 × 10 mm), serving as support during abrasive peeling, was glued to the proximal surface of the sample with instant glue, where the clay had been exposed to the diffusion reservoir solution (**Fig. 25a**). The same procedure was applied to the respective procedural blank samples. After 15 min of hardening both clay samples were placed into two separate plastic vials and transferred to an aerobic box for further processing. First processed was the clay blank sample following by the respective clay diffusion sample. In the case of the diffusion sample, the external surface of the sample

holder was cleaned with KODAN® tissues to remove potential surface contamination introduced upon contact with the spiked pore water of the diffusion reservoir. Each sample was fixed into a bench vise (Hand-Drilling-Machine-Vice 80 mm, Hoffmann Supply Chain GmbH, Nürnberg, Germany) and the groove at the rear part of the sample holder (**Fig. 25a**) was sawed off with a small handsaw (Mini bow saw Ergonomic handle, Hoffmann Supply Chain GmbH) closely to the clay sample, without compromising the embedded clay cylinder (**Fig. 25b**). The remaining PMMA was carefully abraded with abrasive paper (P600), until the distal side (i.e., the side which was not in direct contact with the diffusion reservoir solution) of the clay cylinder was exposed.

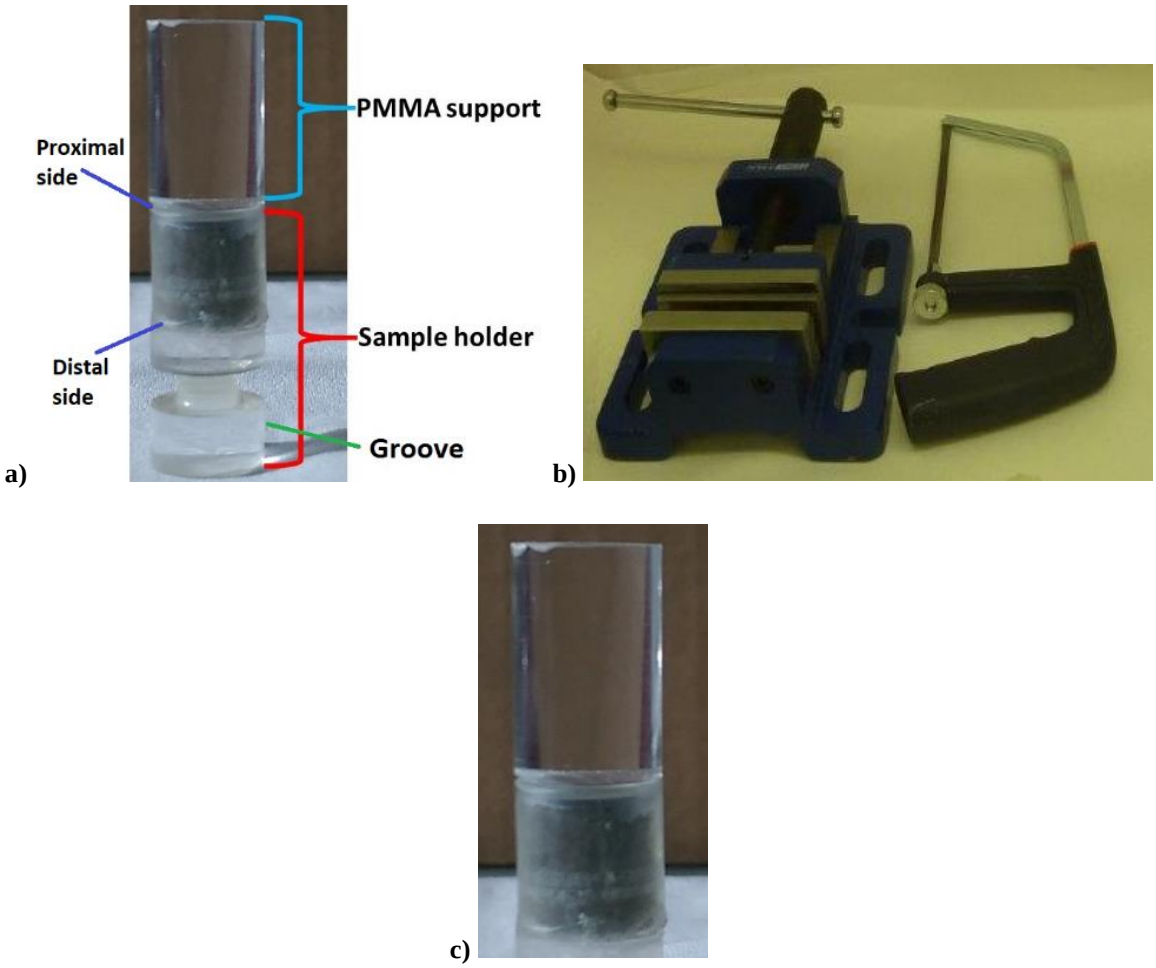

Fig. 25 **a)** PMMA sample holder with embedded OPA sample; PMMA cylinder was glued on top as support, **b)** bench vise and small handsaw, **c)** PMMA sample holder with embedded OPA sample after sawing.

Subsequently, the clay blank sample was submitted to abrasive peeling. The abrasive peeling setup (**Fig. 26**) comprised the following parts: Collet (ER mini collet holder cylindrical + ER collet ER 16, Hoffmann Supply Chain GmbH), for accommodation of the PMMA sample holder during abrasive peeling (1), stainless steel carriage, for fixing the collet and manually moving the clay sample back and forth (2), abrasive paper with grit numbers P150 to P1000

(Abrasive paper (SiC) waterproof Matador, Hoffmann Supply Chain GmbH) (3), support made of PTFE, acting as guide rail for the carriage (4), a pair of quick-releases, for fixing the abrasive paper (5), and a micrometer (Digital Disc Micrometer IP65, Mitutoyo Germany, Neuss, Germany), for length measurement of the clay sample after each abrasion step. Carriage and support were manufactured in-house (INE workshop), based on the technical drawing shown in **Fig. 27**.

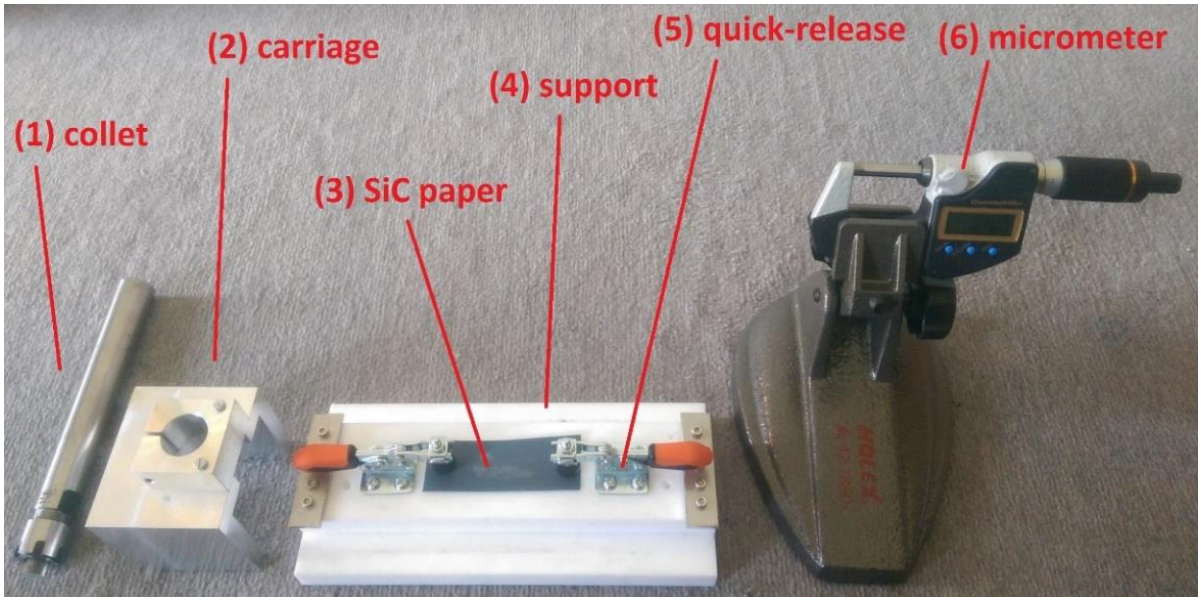

Fig. 26 Abrasive peeling setup with its components: collet (1), carriage (2), abrasive paper (3), support (4), quick-release (5), micrometer (6).

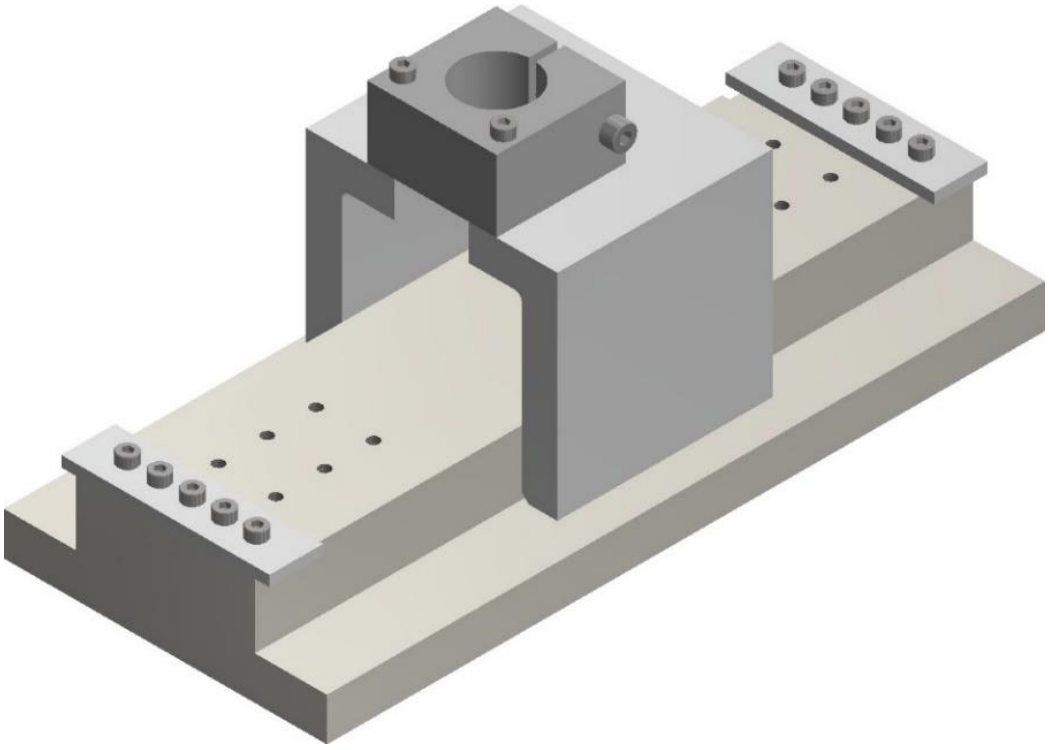

Fig. 27 Drawing of carriage and support of the abrasive peeling setup.

For abrasive peeling, each clay cylinder was mounted on the collet (**Fig. 26**) which was fixed to the carriage. A sheet of abrasive paper (P220) was fixed to the support. By moving the carriage back and forth 20 times, the remaining PMMA was removed, until the surface of the clay was exposed. Subsequently, procedural blank samples for AMS were prepared from the clay blank sample by abrading successive clay segments with layer thicknesses of several hundred microns (see chapter 6) from one clay sample. The layer thickness of each segment was determined by measuring the length of the clay sample before and after abrasive peeling with a micrometer. In order to minimize the uncertainty of the length measurement, each layer thickness was determined by five separate measurements. Before each measurement, the sample was rotated 60–70° around its main axis of rotation, ensuring a representative measurement. The uncertainty of the determined layer thickness is based on the standard deviation of the five individual measurements and was ≤ 5 µm. The abraded clay material of each segment, including the used abrasive paper, was transferred to a designated centrifuge tube (**Fig. 28**). The remaining clay blank sample also served for the preparation of calibration samples for AMS. Subsequently, the clay diffusion sample was completely abraded according to the same procedure as the clay blank sample.

In the case of diffusion experiment I (126 d) all samples were dried overnight by leaving the lids of the centrifuge tubes slightly open. In the subsequent experiments such drying step was skipped (see also sub-chapter 7.1.2).

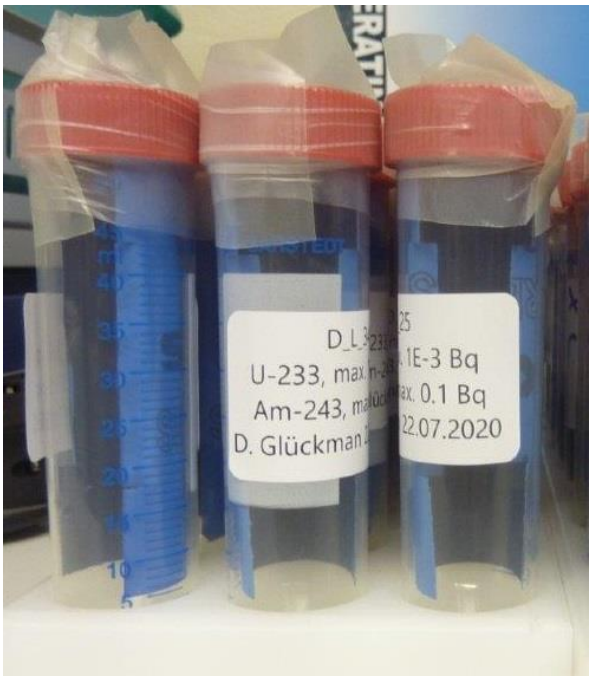

Fig. 28 SiC paper sheets and abraded clay powders stored in centrifuge tubes.

5.6.5 Desorption

To each of the dried samples, 100 µL of a 2.31×10^{-12} mol/L ^{248}Cm solution (see **Tab. B2**) was added gravimetrically, resulting in approximately 10^{-16} mol of ^{248}Cm per sample. Since a ^{236}U standard solution of high enough isotopic purity was not available at the time of sample preparation, ^{248}Cm served as internal standard for the AMS determination of both ^{233}U and ^{243}Am in the clay segments.

All samples were suspended in 30 mL of 4 mol/L HNO_3, respectively, and placed on a horizontal shaker (model RS-LS 20, Phoenix Instrument GmbH, Garbsen, Germany) for 48 h in order to allow for the desorption of ^{233}U and ^{243}Am from the clay. The suspensions were centrifuged and the supernatants containing the desorbed ^{233}U and ^{243}Am as well as the internal standard ^{248}Cm were subjected to AMS sample preparation (see sub-chapter 5.10).

5.7 Inductively coupled plasma–mass spectrometry (ICP–MS)

5.7.1 Basic principle

Different mass spectrometric techniques usually differ in their method of analyte injection, ion formation, and mass separation. In the following, one of the most common methods shall be described, namely ICP–MS. It is a robust and sensitive routine analytical technique, especially, when it comes to the determination of trace amounts of metals, such as actinides, in environmental samples. With respect to the determination of actinide nuclides, state of the art instruments are capable of reaching LODs as low as 1 ppq (≈ 1 pg/L)[88] and an abundance sensitivity of approximately 10^{-7}, as reported for the determination of ^{236}U along with the abundant ^{238}U.[75]

The term “inductively coupled plasma” refers to the type of ionization source. The mass separator usually is either a quadrupole (QP–ICP–MS) or a magnetic sector-field (SF–ICP–MS). The basic setup of a QP–ICP–MS instrument is depicted in **Fig. 29**. The liquid sample, usually diluted in nitric acid of high purity, is injected and dispersed into an aerosol by means of a nebulizer. Subsequently, the aerosol is introduced into the ICP for ionization. Here, an Ar plasma is generated by a high-voltage spark and stabilized by a magnetic field, which is generated and maintained by a radio frequency (RF) coil. Under such conditions, the analyte is ionized at temperatures of 8000–10000 °C.[89] Then, the ion beam is directed to the quadrupole mass analyzer. Here, the incoming ions are selected based on their mass to charge (m/q) ratio. The quadrupole consists of four metal rods, aligned in parallel to the ion beam. Opposite pairs

of rods are electrically connected and share a defined voltage. The chosen voltages for the two pairs of rods have to ensure that only ions with the desired m/q ratio have a stable trajectory through the quadrupole.

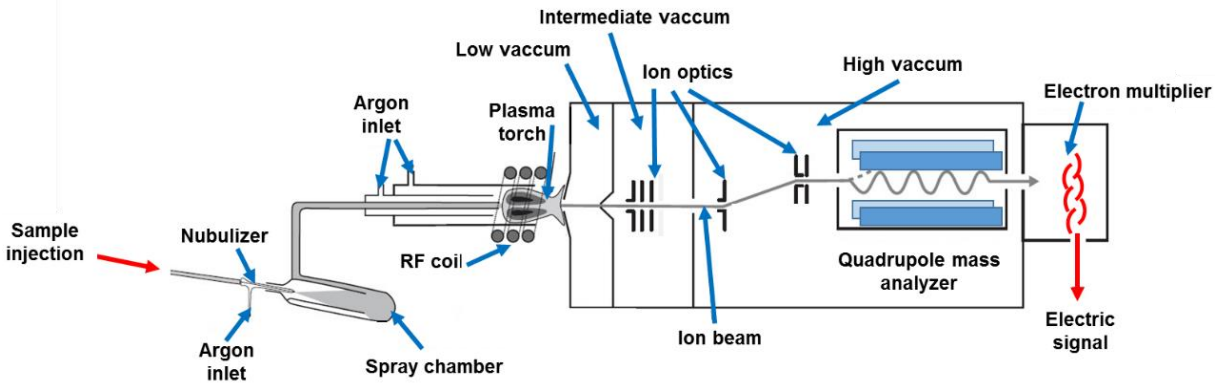

Fig. 29 Principle setup of a quadrupole ICP–MS device (adopted from Linge *et al.* (2009)[90]).

The individual ions exiting the mass analyzer hit the electron multiplier, releasing an avalanche of electrons, resulting in the amplification of the initial signal. Ultimately, the ions are counted by conversion into discrete electrical signals. In order to quantify the analyte´s absolute concentration in a real sample, its signal has to be compared with that from a calibration sample (see sub-chapter 5.7.2). Instead of a quadrupole, the mass analyzer of a SF–ICP–MS instrument is featured by a combination of an electromagnet and an electrostatic analyzer. In this way, the ion beam consisting of ions with the desired m/q ratio is double focused, resulting in a considerably improved mass resolution (up to $m/\Delta m = 10000$) compared to conventional QP–ICP–MS setups ($m/\Delta m \approx 300$).[89]

Regardless of the kind of ICP–MS setup, the sensitive determination of nuclides can be limited. One reason is the peak tailing of neighboring masses. For instance, when analyzing ^{233}U in the presence of abundant ^{232}Th, the peak of $m = 232$ u can interfere by partial overlap with the peak of $m = 233$ u.[91] The LOD is also influenced by the presence of isobaric interferences. For instance, during the determination of ^{233}U and ^{239}Pu, the formation of the cationic molecular species $[^{232}Th^{1}H]^{+}$ and $[^{238}U^{1}H]^{+}$, respectively, have always to be considered. In order to estimate the impact of such molecular isobars on the analysis of a certain nuclide, it is crucial, to determine the formation rate of the relevant molecular isobars during every beam time. A further process, impairing the theoretically achievable LOD, is sample dilution. Depending on the matrix of the analyte, dilution is necessary, in order not to exceed the instrument´s maximum allowed salt concentration.

5.7.2 ICP–MS analyses in this study

In the frame of this work, ICP–MS was employed for element quantification in the pore water solutions of the diffusion experiments. Prior to analysis, all pore water solution aliquots were diluted 1:250 with 2 % HNO_3. The analysis of ^{233}U and ^{243}Am was carried out with SF–ICP–MS (ELEMENT XR sector-field ICP–MS, Thermo Fisher Scientific, Schwerte, Germany) and QP–ICP–MS (iCAP™ RQ ICP–MS, Thermo Fisher Scientific). Further pore water constituents, such as Na^+, K^+, Mg^{2+}, Ca^{2+}, Sr^{2+} were determined with the ELAN6100 Quadrupole ICP–MS device (Thermo Fisher Scientific, Schwerte, Germany).

Nuclide quantification was based on external standard calibration and internal standardization. For instance, in the case of ^{233}U analysis, external calibration was performed with standard samples of Th with concentrations of 1 ppt, 2 ppt, 5 ppt, 10 ppt, 20 ppt, and 50 ppt. Additionally, the ICP–MS instruments were calibrated with the certified reference standard materials SPS-SW1 and SPS-SW2 (Spectrapure Standards as, P.O. Box 190 Manglerud, Oslo, Norway), containing 45 metal elements with concentrations ranging between 2.5 ng/mL and 10 µg/mL.

To each sample, calibration standard, and instrumental and procedural blank, a solution of ^{103}Rh was added, resulting in a ^{103}Rh concentration of 2 ppb in each sample. While the instrumental blank consisted solely of the diluting agent (i.e., ultra-pure 2 % HNO_3), the procedural blank contained additionally the matrix of the real sample. In order to obtain the absolute concentration of an element, ctrs of the element of interest and of the internal standard, as well as the external calibration curve had to be considered. The corresponding mathematical expression is shown in **Eq. 20** for the example of the determination of the ^{233}U concentration:[92]

$$c(^{233}\mathrm{U}) = \frac{\mathrm{ctr}(^{233}\mathrm{U})}{s} \cdot \frac{\mathrm{ctr}(^{103}\mathrm{Rh_{cal}})}{\mathrm{ctr}(^{103}\mathrm{Rh})} \qquad \textbf{Eq. 20}$$

where $c(^{233}U)$ [ppt] is the absolute concentration of ^{233}U, $\mathrm{ctr}(^{233}U)$ [s^{-1}] is the ctr of ^{233}U in the sample, s [ctr/ppt] is the slope of the calibration curve, $\mathrm{ctr}(^{103}Rh_{cal})$ [s^{-1}] is the average ctr of ^{103}Rh in the calibration samples, and $\mathrm{ctr}(^{103}Rh)$ is the ctr of the internal standard. The quotient $\mathrm{ctr}(^{233}U)/s$ represents the external standard calibration, while $\mathrm{ctr}(^{103}Rh_{cal})/\ \mathrm{ctr}(^{103}Rh)$ represents the internal standardization. With regard to external standard calibration it is mandatory that the y-axis intercept of the calibration curve is equal to zero.

5.8 Ion chromatography (IC)

Ion chromatography is a type of liquid chromatography and employed for the determination of anionic species, such as Cl^-, F^-, and SO_4^{2-}. The analyte solution (mobile phase) is injected into the device and passes a positively charged ion exchange column (stationary phase). Based on its affinity towards the ion exchange column, the analyte shows a characteristic distribution between the stationary and the mobile phase. After passing the column, the anions are detected, for instance, by a conductivity detector.

Within this study, an ICS-3000 ion chromatography system (Thermo Fisher Scientific, Schwerte, Germany), equipped with a Dionex IonPac AS9-HC column was used for Cl^- and SO_4^{2-} analysis. All samples were diluted with MQ water according to the measurement range of the device (0.1–10 ppm). The LOD of the device is 0.01 ppm with an overall uncertainty of ≤ 10 %.

5.9 Dissolved inorganic carbon determination (DIC)

Saturation vessel solutions were analyzed for their dissolved inorganic carbon content with a TOC-L Virtual Advisor device (Shimadzu, Duisburg, Germany). Calibration was performed with a stock solution of $NaHCO_3$ and Na_2CO_3, with a calibration range of 1–30 mg/L of carbon. All samples were diluted with MQ. The LOD of the device is approximately 0.05 mg/L.

5.10 AMS sample preparation

25 mL of each supernatant obtained after desorption were transferred to PTFE beakers. They were evaporated on a hotplate at 150 °C to an approximate volume of 5 mL. Subsequently, 15 mL of MQ water was added, resulting in 20 mL of a solution, containing HNO_3 at a concentration of approximately 1 mol/L.

Subsequently, the solutions were transferred to designated 50 mL centrifuge tubes. All PTFE beakers were rinsed twice with 5 mL of 1 mol/L HNO_3. The rinsing solutions were merged with the solutions in the corresponding centrifuge tubes. 250 µL of a 3.2 g/L $FeCl_3$ solution (prepared from iron powder, **Tab. 8**) was added to each sample, resulting in ≈ 40 mg/L Fe. Then, slowly a solution of 25 % NH_3 was added dropwise. The centrifuge tubes were shaken gently after each addition. Once a stable brownish precipitate of $Fe(OH)_3$ had formed, NH_3 addition was stopped. After 1 d, the suspensions were centrifuged at 4000 rpm for 10 min. Afterwards, the supernatants were discarded and the precipitates were washed twice with 5 mL

of 0.05 % NH_3 solution. Following, a few drops of 0.05 % NH_3 solution were added and the wet precipitates were transferred to Eppendorf tubes (Eppendorf Safe-Lock, 0.5 mL, Eppendorf GmbH, Germany). The samples were centrifuged at 4000 rpm for 5 min and the remaining supernatants were discarded. The $Fe(OH)_3$ precipitates were dried at 80 °C for 4 h. Subsequently, the dried precipitates were transferred into quartz crucibles and combusted in a furnace (Nabertherm P330, Nabertherm, Lilienthal, Germany) at 800 °C, yielding in iron oxide pins with a total mass of few milligrams and a diameter of approximately 1 mm.

The iron oxide pins were pressed into sample cathodes (see sub-chapter 4.2.1) with a sample press, provided by the VERA laboratory (**Fig. 30**). After each pressing, all parts of the sample press were cleaned with ethanol in order to minimize the risk of cross-contamination.

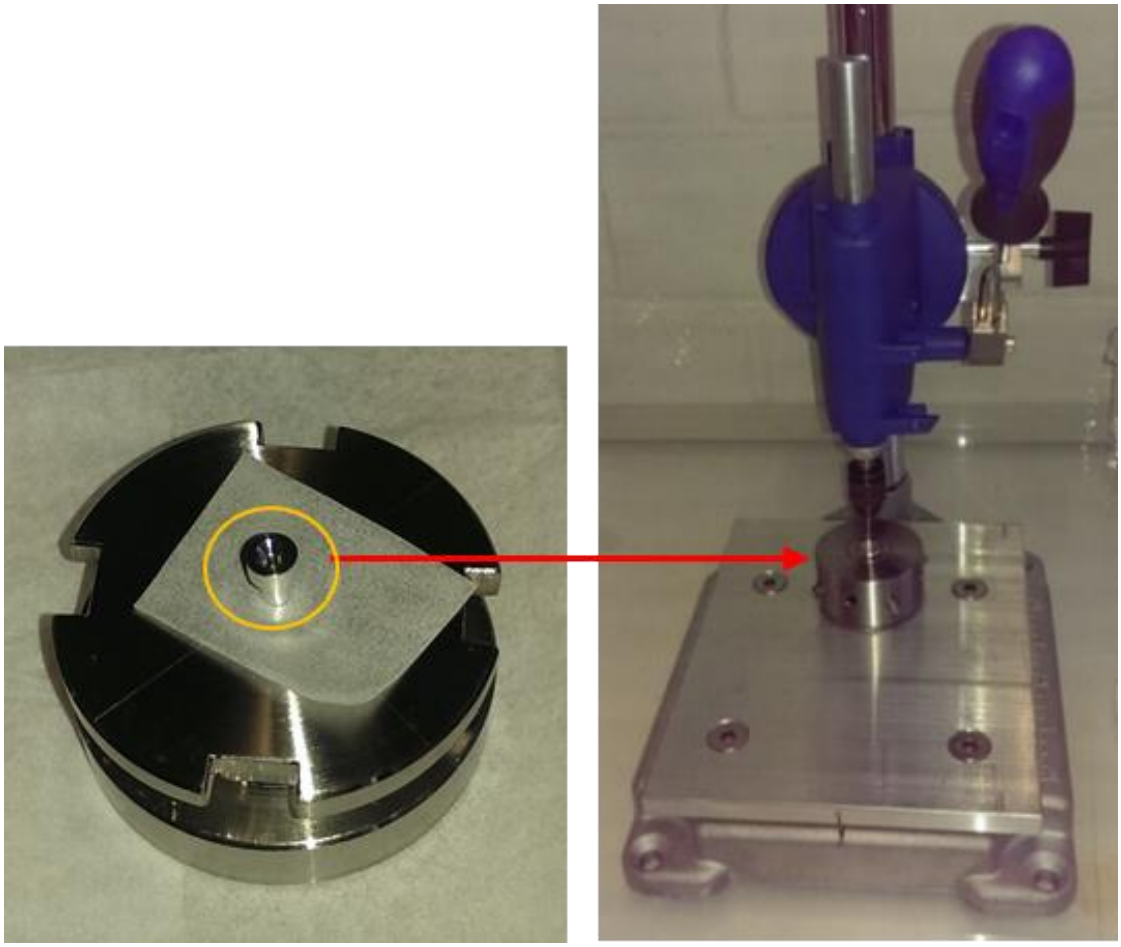

Fig. 30 AMS sample press with sample cathode (highlighted with orange circle).

5.11 X-ray microtomography (µCT)

In order to investigate the potential presence of micro-fractures, two samples of OPA were scanned with an X-ray microtomography (µCT) device. The µCT scans were conducted with an Xradia 520 Versa (Zeiss, Oberkochen, Germany) at a tube voltage of the X-ray source of

80 kV, an optical magnification of 0.4, and a spatial resolution of 10 µm. Segmentation of the obtained images was performed with GeoDict 2021®[93] and the included denoising and grey values correction filters.

5.12 Modeling software

5.12.1 Solubility and speciation calculations with PHREEQC

In order to choose an appropriate diffusion setup and suitable initial concentrations for the diffusing tracers ^{233}U and ^{243}Am, solubility limits and the dominant speciation of the diffusing tracers in OPA pore water needed to be estimated. Therefore, solubility and speciation calculations were carried out with PHREEQC v.3,[94] using the ThermoChimie v.10 database,[95] applying the specific ion interaction theory (SIT) approach for ionic strength corrections. The geochemical parameters of OPA pore water used for the calculations, such as elemental composition and pH, were based on the composition after Gimmi *et al.* (2014),[1] as shown in **Tab. 9** (see sub-chapter 5.3). Since the diffusion experiments were planned to be carried out under anaerobic conditions in a glovebox ($\theta = 25$°C) under Ar atmosphere (typically $[O_2] \leq 0.1$ ppt), an E_h of −60 mV (SHE (standard hydrogen electrode))[51] was assumed. The calculated dominant aquatic species of U and Am in pore water and their corresponding solid phases are shown in **Tab. 21** (see sub-chapter 7.2).

The aqueous speciation of U and Am in the actual diffusion reservoir solutions were calculated based on the experimentally determined pore water compositions (i.e., concentrations of cations, anions, DIC), aqueous actinide tracer concentrations, pH, and E_h. The true ionic strength (I_t [mol/L]) was re-calculated based on the actual pore water composition in the diffusion reservoir solution.

Since no E_h was measured during diffusion experiments I (126 d) and II (240 d), for such speciation and solubility calculations an E_h of −60 mV (SHE)[51] was used. DIC concentrations in the pore water solution were only measured during diffusion experiments III (20 d) and IV (36 d). As described in sub-chapter 7.5, there was a substantial decrease in CO_3^{2-}/HCO_3^- concentrations due to the degassing of CO_2 during reservoir equilibration. Since the experimentally obtained DIC concentrations during such experiments ranged between $(8.1\pm0.3) \times 10^{-5}$ mol/L and $(1.3\pm0.1) \times 10^{-4}$ mol/L, the mean value $CO_3^{2-}/HCO_3^- = 9.2 \times 10^{-5}$ mol/L was used as input parameter value for the U(VI) and Am(III) speciation calculations in all diffusion experiments.

5.12.2 Modelling of diffusion profiles with COMSOL Multiphysics®

For scoping calculations of the expected diffusion distances as well as for fitting of the experimental diffusion profiles of ^{233}U and ^{243}Am in OPA, a 1D pore diffusion model based on Fick´s laws in COMSOL Multiphysics® (version 5.6)[96] was used. The clay sample in the model was assumed to be cylindrical and to have a length of 10 mm and a diameter of 6 mm. K_d values of U(VI) and Am(III) as well as the D_e of U(VI), determined in OPA, were available from batch sorption and diffusion experiments in OPA, reported in previous studies (see **Tab. 7**).[2,51] Due to the unavailability of D_e(Am(III)) in OPA, the D_e value of the analogue lanthanide Eu(III), obtained in a diffusion experiment through OPA, was used.[3] Initial concentrations (c_0 / (mol/L)) of U(VI) and Am(III) were based on the equilibrium concentrations, determined during the equipment sorption test (see sub-chapter 7.4). A complete overview of the model parameter values can be found in **Tab. 10**. Diffusion times of 120 d, 240 d, and 480 d were simulated.

Tab. 10 Model parameters and corresponding values for the simulation of the diffusion of U(VI) and Am(III) through OPA using COMSOL Multiphysics® (version 5.6) with a 1D pore diffusion model.

Parameter	Value
Clay sample length / mm	10 [46]
Clay sample diameter / mm	6
ρ_d / (kg/m³)	2450 [*), 35]
ε_{eff} / –	0.16 [*), 35]
K_d (U(VI)) / (m³/kg)	0.025 [2]
K_d (Am(III)) / (m³/kg)	30 [51]
D_e (U(VI)) / (m²/s)	1.9×10^{-12} [2]
D_e (Am(III))[**)] / (m²/s)	5.0×10^{-11} [3]
c_0(U(VI)) / (mol/L)	3.2×10^{-9}
c_0(Am(III)) / (mol/L)	3.0×10^{-9}
t / d	120, 240, 480

[*)] Mean value. [**)] D_e of Eu(III) was used, which can be considered as an analog for Am(III).

For fitting the experimentally obtained diffusion profiles, in the case of U(VI) and the first profile part of Am(III), the actual clay cylinder length and diameter as well as ρ_d and ε_{eff} of OPA available from literature were used as input parameters (**Tab. 10**). ^{233}U and ^{243}Am

concentrations measured after equilibration with the diffusion reservoir components were used as initial tracer concentrations.

As discussed in sub-chapter 7.10, for the second part the of Am(III) profile (hereafter referred to as “fast-diffusing species profile”) a colloid-mediated transport along micro-fractures via water diffusion is hypothesized, with initial colloid-bound Am(III) present at concentrations approximately ten times lower than the aqueous species. Thus, the fast-diffusing species profile of Am(III), observed in diffusion experiments I (126 d) and II (240 d) were modelled in the following manner: µCT scans of OPA specimens (sub-chapter 7.9) showed a volume fraction of micro-fractures of up to 5 % v/v. Based on this, as a simple approximation, one single fracture with the dimension of 5 % v/v was assumed, which, given the clay sample´s length of 10 mm, corresponds to a fracture 670 µm long. As transport mode through the fracture water diffusion was assumed. Due to the absence of a porous structure, ε_{eff} of the clay was replaced by a porosity of 100 % in the model (**Tab. 11**).

Tab. 11 Input parameter values for the modelling of the experimentally obtained second part of the Am(III) profiles, assuming water diffusion of Am(III) through fractured OPA, using a 1D pore diffusion model in COMSOL Multiphysics® (version 5.6).

Parameter	Value
Clay sample length / mm	10
Clay fracture length / mm	0.670
ε_{eff} / –	1
$c_0(\mathrm{Am(III)})_{coll}$ / (mol/L)	3×10^{-10}
t / d	126, 240

6 Development of diffusion experiments at ultra-trace actinide levels

6.1 Estimation of laboratory background

During the preparation of samples for ultra-trace analysis of actinides, laboratory contamination and cross-contamination, caused by aerosols and other airborne particles may play a relevant role. Therefore laboratory background measurements were conducted in the locations foreseen for the diffusion experiment (i.e., glovebox) and the subsequent sample processing via abrasive peeling (i.e., preparatory box), comprising the analysis of ultra-trace contents of the actinide nuclides ^{233}U,^{237}Np, ^{243}Am, and ^{248}Cm. For this purpose, in the glovebox and the preparatory box 4 PTFE beakers (ISO LAB Laborgeräte GmbH, Wertheim, Germany) were set up, respectively, each containing 25 mL of 1 mol/L HNO_3, serving as collectors of potential airborne contamination. After 7 d, all solutions were transferred to centrifuge tubes and subjected to $Fe(OH)_3$ co-precipitation and the subsequent steps of AMS sample preparation, as described in sub-chapter 5.10.

6.2 Diffusion experiment I (126 d)

After termination of the diffusion experiment five separate procedural blank samples for AMS (Blank 1 to Blank 5) were prepared with layer thicknesses from 227 µm to 336 µm (**Tab. 12**). Subsequently, three calibration samples for AMS (Calibration 1 to Calibration 3) were prepared with layer thicknesses from 315 µm to 367 µm (**Tab. 12**).

The clay diffusion sample was completely abraded, resulting in 47 separate segments. Layer thicknesses ranged between approximately 20 µm at the proximal side and 380 µm at the distal side of the sample. 10 of the abraded clay segments were selected for AMS analysis (**Tab. 13**). The selection was based on the expected maximum diffusion distance of 4.9 mm after 120 d (see scoping calculations, sub-chapter 7.3). It was considered reasonable to only select two samples beyond the expected diffusion distance (i.e., samples 1 and 2, at 8908±190 µm and 5596±174 µm, respectively), while the other 8 sample positions were below the expected maximum diffusion distance.

The desorption solution of clay segment DS-10 was further diluted during AMS sample preparation (see sub-chapter 5.10), resulting in a total dilution of 1:1000. Such dilution was necessary, since clay segment DS-10 was in direct contact with the diffusion reservoir solution

during the diffusion experiment. Thus, an elevated ^{243}Am concentration in sample DS-10 was expected, potentially exceeding the measurement range of AMS. Since SF–ICP–MS was not available at the time of the experiment, dilution was performed as precautionary measure.

Tab. 12 Procedural blanks and calibration samples from diffusion experiment I (126 d) for AMS analysis; thickness of each layer Δx_i [µm]. All segments were abraded with abrasive paper P220.

Sample name	**Δx_i / µm**
Blank 1	336±1
Blank 2	302±1
Blank 3	355±1
Blank 4	334±1
Blank 5	227±1
Calibration 1	315±3
Calibration 2	367±2
Calibration 3	357±4

Tab. 13 Clay diffusion samples from diffusion experiment I (126 d), selected for AMS analysis: the distance within the cylindrical clay sample before ($x_{i,\ before}$) and after ($x_{i,\ after}$) the respective abrasion step [µm]; sample 1 (9088 µm) represents the distal side of the clay cylinder and sample 10 (0 µm) the proximal side which was immersed into the diffusion reservoir solution; thickness of each layer (Δx_i) [µm]; sample position is represented as ($x_{i,\ before} - 0.5\Delta x_i$)$\pm\Delta x_i$ [µm]; abrasive paper grit number used for abrasion of corresponding layer.

Sample number *i*	Sample name	Δx_i / µm	$x_{i,\ before}$ / µm	$x_{i,\ after}$ / µm	Sample position / µm	Abrasive paper grit number
1	DS-1	380±3	9088	8718	8908±190	P220
2	DS-2	347±3	5770	5422	5596±174	P220
3	DS-3	216±1	2672	2456	2564±108	P220
4	DS-4	118±1	1052	935	993±59	P220
5	DS-5	40±2	280	240	260±20	P600
6	DS-6	31±1	209	153	138±16	P600
7	DS-7	41±1	123	82	102±21	P600
8	DS-8	38±1	82	44	63±19	P600
9	DS-9	24±2	44	20	32±12	P1000
10	DS-10	20±1	20	0	10±10	P1000

6.3 Diffusion experiment II (240 d)

Diffusion experiment I (126 d) revealed a deeper penetration of the diffusing tracers ^{233}U and ^{243}Am into the clay than expected from scoping calculations (see sub-chapter 7.3). Additionally, fairly high blank levels were observed for both tracers. Laboratory background introduced by previous experiments conducted in the used glovebox was ruled out as source (see sub-chapter 7.1.1). The most likely sources of background and cross-contamination were assumed to be airborne contamination released during abrasive peeling and a potential contamination of the external surface of the clay diffusion sample holder. Besides the elevated background levels, further potential reasons for the diffusion profile tailings needed to be investigated. In the following sub-chapters, a description of the changed experimental procedures, addressing the potential sources of background, cross-contamination, and diffusion profile tailings, will be given.

6.3.1 Clean laboratory and glove bags

In order to minimize the risk of potential contamination originating from laboratory background, all steps of the sample processing were performed in a laboratory exhaust hood kept clean of high levels of radioactive tracers. It was considered clean, since none of the actinide nuclides, relevant for the conducted diffusion experiments, were handled in the exhaust hood prior to sample processing. As a further precaution against cross-contamination, every step of sample processing involving the release of airborne particles (i.e., sawing, drilling, abrasive peeling) was carried out in an individual, airtight glove bag (Aldrich® AtmosBag (size M), Merck, Darmstadt, Germany) as shown in **Fig. 31**.

Fig. 31 Glove bag, equipped with handsaw, vise, and KODAN ® tissues.

6.3.2 Removal of external surface of sample holder

The clay diffusion sample was introduced into a glove bag (**Fig. 31**) and fixed into a bench vise. The groove at the rear part of the sample holder was sawed off closely to the clay sample. The remaining PMMA was carefully abraded with abrasive paper (P600), until the distal side of the clay cylinder was exposed. Subsequently, the external surface of the sample holder was cleaned with KODAN® tissues, in order to remove PMMA swarf. Afterwards, the clay diffusion sample was transferred to a fresh glove bag. In order to prevent cross-contamination of the segmented clay layers by tracers sorbed on or incorporated into the PMMA sample holder, the external

surface of the sample holder was abraded with a nail file to a depth of approximately 100 µm, as confirmed with a micrometer. Such abrasion was performed between 0–2, 2–10, and 10–18 mm height, relative to the proximal side of the sample (**Fig. 32b**). After each abrasion step potentially contaminated PMMA swarf was removed from the sample holder with KODAN® tissues. The abraded PMMA material was collected in separate centrifuge tubes and subjected to desorption with 4 mol/L HNO_3 and further sample preparation for AMS analysis. Afterwards, the clay diffusion sample was transferred to a new glove bag for abrasive peeling.

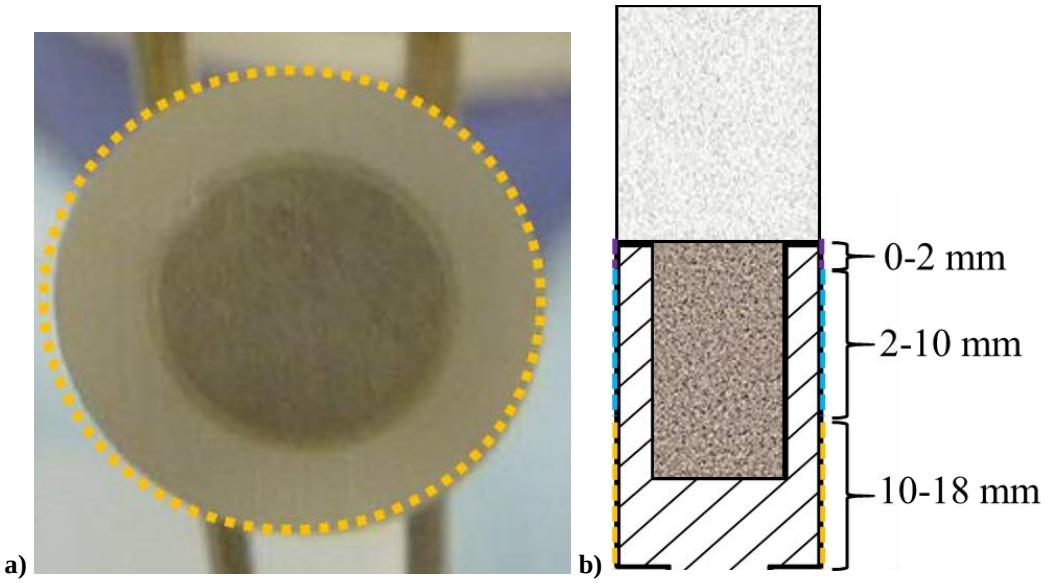

Fig. 32 **a)** Top view of the clay cylinder embedded into PMMA sample holder with external surface (orange dashed lines), **b)** illustration of PMMA sample holder; external surface was abraded to a depth of approximately 100 µm at three different heights relative to the proximal sample side: 0–2 mm (purple dashed lines); 2–8 mm (light blue dashed lines); 10–18 mm (orange dashed lines).

Four separate procedural blank samples for AMS (Blank 6 to Blank 9) were prepared with layer thicknesses from 101 µm to 165 µm, as well as three AMS calibration samples (Calibration 4 to Calibration 6) with layer thicknesses from 146 µm to 174 µm were abraded (**Tab. 14**).

Tab. 14 Procedural blanks and calibration samples from diffusion experiment II (240 d) for AMS analysis; thickness of each layer Δx_i [µm]. All segments were abraded with abrasive paper P220.

Sample name	Δx_i / µm
Blank 6	165±7
Blank 7	132±3
Blank 8	101±5
Blank 9	124±7
Calibration 4	154±4
Calibration 5	174±5
Calibration 6	146±5

6.3.3 Profile samples including the investigation of potential rim mobility

In order to explore potential preferential pathways along the rim between the clay sample, the epoxy resin, and the inner part of the sample holder, clay diffusion sample II was abraded according to the following procedure: First, three successive segments at the distal part of the sample were abraded, as illustrated in **Fig. 33a**. Second, a core segment was drilled with a diameter of approximately 4.2 mm and a depth of 2746±32 µm using a stainless-steel drill bit (indicated as red box in **Fig. 33b**). Subsequently, the corresponding rim region was abraded in five separate segments. Segments 1 and 3 were submitted to AMS analysis (indicated as purple boxes in **Fig. 33c**). Another core segment was drilled with a diameter of approximately 2.5 mm and a depth of 1866±40 µm (indicated as light blue box in **Fig. 33d**). The corresponding rim region was abraded in four separate segments. Segments 1 and 4 were submitted to AMS analysis (indicated as dark blue boxes in **Fig. 33e**). For the remaining sample (0–3823 µm) the full segments were abraded (**Fig. 33f**).

The drilling of the core regions accompanied by the abrasion of the corresponding rim regions allowed for the separate analysis of the two regions, and consequently, the investigation of potential differences in tracer mobilities through sample core and rim. **Fig. 34** and **Tab. 15** give an overview of the dimensions of the individual full, core, and rim segments.

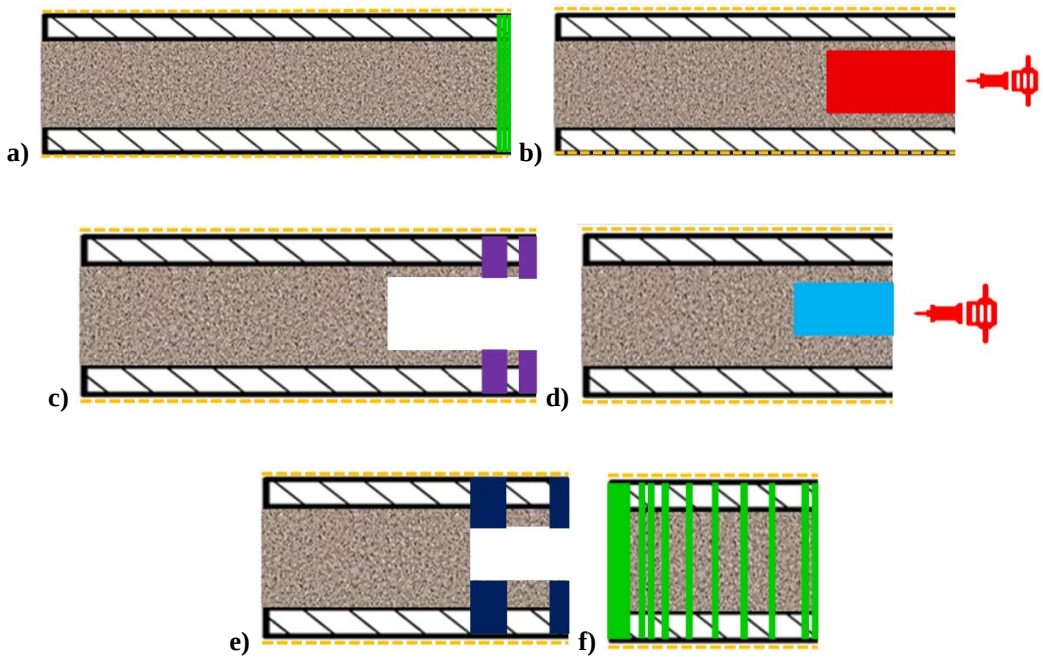

Fig. 33 Illustration of abrasion and drilling of clay diffusion sample II after removal of the external surface of the sample holder, shown as dashed orange lines; **a)** abrasion of three successive segments, **b)** drilling of clay cylinder core region (diameter: 4.2 mm, length: 1373 µm, red segment), **c)** abrasion of rim region in five separate segments; segments 1 and 3 indicated in purple, **d)** drilling of clay cylinder core region (diameter: 2.5 mm, length: 933 µm, light blue segment), **e)** abrasion of rim region in four separate segments; segments 1 and 4 indicated in purple, **f)** abrasion of the remaining sample.

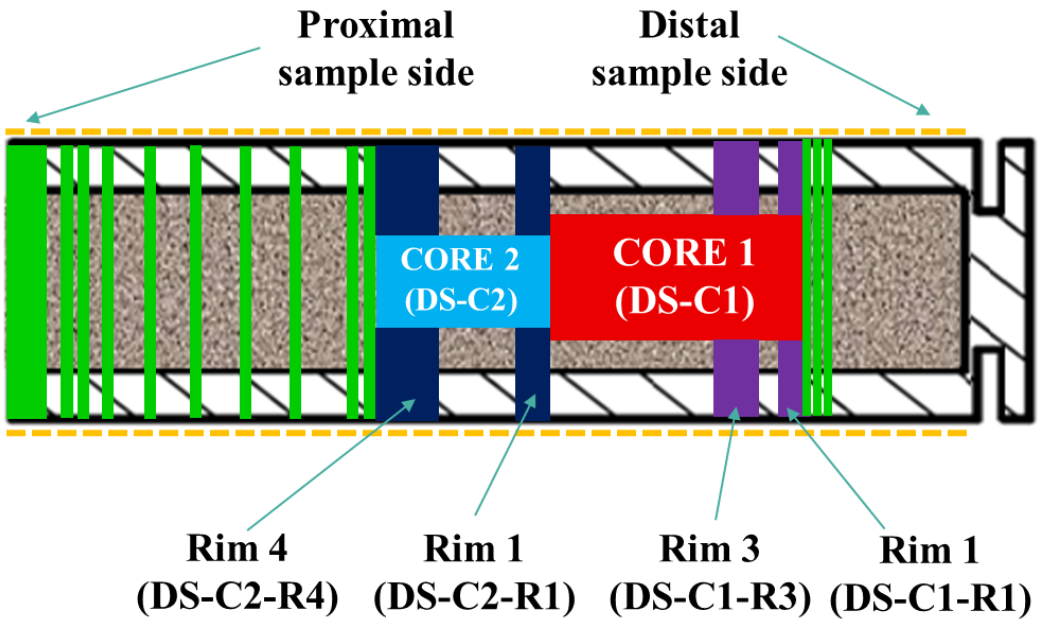

Fig. 34 Overview of sampling methods and positions in clay diffusion sample II; abraded full segments (green), drilled core segments (light blue & red), and abraded rim segments (dark blue and purple). External surface of sample holder, abraded prior to the segmentation of the clay diffusion sample is indicated as dashed orange lines.

Tab. 15 Clay diffusion samples from diffusion experiment II (240 d) selected for AMS analysis: thickness of each layer (Δx_i) [µm]; the distance within the cylindrical clay sample before ($x_{i,\ before}$) and after ($x_{i,\ after}$) the respective abrasion step [µm]; sample 11 represents the distal side of the clay cylinder and sample 30 represents the proximal side, which was immersed into the diffusion reservoir solution; sample position indicated as ($x_{i,\ before} - 0.5\Delta x_i$)$\pm\Delta x_i$ [µm].

Sample number *i*	**Sample name**	**Δx_i / µm**	**$x_{i,\ before}$ / µm**	**$x_{i,\ after}$ / µm**	**Sample position / µm**	**Abrasive paper grit number**
11	DS-11	50±3	8684	8634	8659±25	P1000
12	DS-12	106±9	8634	8528	8581±53	P220
13	DS-13	93±6	8528	8435	8482±47	P220
14	DS-C1	2746±32	8435	5689	7062±1373	–
15	DS-C1-R1	365±9	8435	8070	8253±183	P220
16	DS-C1-R3	483±2	7888	7405	7647±242	P220
17	DS-C2	1866±40	5689	3823	4756±933	–
18	DS-C2-R1	341±10	5689	5348	5519±171	P220
19	DS-C2-R4	645±10	4468	3823	4146±323	P220
20	DS-14	120±5	3823	3703	3763±60	P220
21	DS-15	130±4	3703	3068	3638±65	P220
22	DS-16	95±5	3068	2538	3021±48	–
23	DS-17	89±5	2538	2036	2494±45	P220
24	DS-18	105±12	2036	1558	1984±53	P220
25	DS-19	57±5	1558	1058	1530±29	P600
26	DS-20	56±4	1058	823	1030±28	–
27	DS-21	66±5	823	663	791±33	P600
28	DS-22	55±10	663	608	636±28	P600
29	DS-23	360±8	608	248	428±180	P220
30	DS-24	248±5	248	0	124±124	P600

6.4 Diffusion experiments III (20 d) and IV (36 d)

Similar to diffusion experiment I (126 d), a fast-diffusing species profile of Am(III) was also observed in diffusion experiment II (240 d). Hence, two short experiments (20 d and 36 d) were conducted with the aim of monitoring the time-dependent formation of the fast-diffusing species profile of Am(III).

After termination of the diffusion experiments two procedural blank samples were prepared for AMS analysis for diffusion experiment III (Blank 10 and 11) and diffusion experiment IV (Blank 12 and 13), respectively, with layer thicknesses from 137 µm to 374 µm. Furthermore, one calibration sample for AMS (Calibration 7) was prepared (**Tab. 16**). From the abraded clay diffusion samples from experiments III and IV, 7 and 8 segments were selected for AMS analysis, respectively (**Tab. 17**, **Tab. 18**).

Tab. 16 Procedural blanks and calibration samples from diffusion experiment III (20 d) & IV (36 d) for AMS analysis; thickness of each layer Δx_i [µm]. All segments were abraded with abrasive paper P220.

Sample name	Δx_i / µm
Blank 10	137±6
Blank 11	146±4
Blank 12	237±5
Blank 13	374±5
Calibration 7	180±4

Tab. 17 Clay diffusion samples from diffusion experiment III (20 d), selected for AMS analysis: thickness of each layer (Δx_i) [µm]; the distance within the cylindrical clay sample before ($x_{i,\ before}$) and after ($x_{i,\ after}$) the respective abrasion step [µm]; sample 31 represents the distal side of the clay cylinder and sample 37 represents the proximal side, which was immersed into the diffusion reservoir solution; sample position as ($x_{i,\ before} - 0.5\Delta x_i$)$\pm\Delta x_i$ [µm].

Sample number *i*	Sample name	Δx_i / µm	$x_{i,\ before}$ / µm	$x_{i,\ after}$ / µm	Sample position / µm	Abrasive paper grit number
31	DS-25	220±5	8404	8184	8294±110	P220
32	DS-26	225±6	5746	5251	5364±113	P220
33	DS-27	352±3	1426	1074	1250±176	P220
34	DS-28	99±4	608	509	559±50	P220
35	DS-29	60±5	250	190	220±30	P600
36	DS-30	71±4	130	60	95±35	P600
37	DS-31	58±4	60	0	30±30	P600

Tab. 18 Clay diffusion samples from diffusion experiment IV (36 d), selected for AMS analysis: thickness of each layer (Δx_i) [µm]; the distance within the cylindrical clay sample before ($x_{i,\ before}$) and after ($x_{i,\ after}$) the respective abrasion step [µm]; sample 38 represents the distal side of the clay cylinder and sample 45 represents the proximal side, which was immersed into the diffusion reservoir solution; sample position as ($x_{i,\ before} - 0.5\Delta x_i$)$\pm\Delta x_i$ [µm].

Sample number *i*	Sample name	Δx_i / µm	$x_{i,\ before}$ / µm	$x_{i,\ after}$ / µm	Sample position / µm	Abrasive paper grit number
38	DS-32	300±5	9144	8844	8994±150	P220
39	DS-33	293±8	6893	6600	6747±147	P220
40	DS-34	205±4	4629	4424	4527±103	P220
41	DS-35	199±6	1663	1464	1564±100	P220
42	DS-36	149±9	1149	1000	1075±75	P220
43	DS-37	84±5	307	223	265±41	P600
44	DS-38	27±4	27	0	14±14	P600
45	DS-39	96±4	0	−96 *)	95±35	P600

*) Segment DS-39 contained PMMA, which was abraded to ensure full recovery of tracer sorbed onto the proximal side of the clay sample.

7 Results and discussion

7.1 Results on minimization of cross-contamination effects and ultra-trace background corrections

As stated in sub-chapter 1.2, diffusion experiments involving ultra-trace concentration levels of actinide tracers required not only an extremely sensitive analytical technique for tracer quantification (i.e., AMS), but also the development of a diffusion setup and post-mortem segmentation method, which minimizes the risk of artefacts by cross-contamination or background effects. Sub-chapters 7.1.1 to 7.1.5 illustrate how the minimization of such effects was achieved.

7.1.1 Laboratory background prior to the experiment

Prior to diffusion experiment I (126 d) laboratory background measurements in the glovebox (i.e., location of diffusion experiment) and the preparatory box (i.e., location of abrasive peeling setup) were performed with AMS, as described in sub-chapter 6.1. It shall be pointed out that the goal of these analyses was to obtain an overview of the background of all nuclides of interest, i.e., the diffusing tracers ^{233}U and ^{243}Am, as well as the internal standard ^{248}Cm. Therefore, the samples were not spiked with an internal standard and, consequently, the ctrs shown in **Tab. 19** cannot be converted into a quantity (mol). However, they can be compared to ctrs of blank samples, prepared under clean laboratory conditions, as reported in a previous study,[16] as also shown in **Tab. 19**. For ^{243}Am and ^{248}Cm no counts were detected in any sample, thus, indicated as ctr = 0 cts/s. The ctrs of ^{233}U were very low and ranged between 10^{-4} and 10^{-3} cts/s.

Consequently, laboratory background prior to the conduction of the diffusion experiment and the abrasive peeling procedure can be excluded as source of increased background levels of ^{233}U and ^{243}Am. The laboratory background measurements also included the determination of ^{237}Np. The reason for investigating ^{237}Np was that this nuclide has been used in the diffusion experiment glovebox for several years in the frame of previous experiments, before the box was professionally decontaminated. Despite such decontamination, ^{237}Np was found in the glovebox background samples at levels of ≈ 1 count/s. This is more than three orders of magnitudes higher than under clean laboratory conditions, as reported by Glückman *et al.* (2022)[16] ($\approx 10^{-3}$ cts/s). Before analysis of the glovebox background samples, instrumental blank samples were measured, which have been prepared and used exclusively inside the VERA facility, giving

zero counts for ^{237}Np. Hence, it is evident that the ^{237}Np signals originate from the glovebox background samples.

Although the finding of background on ^{237}Np is not of direct relevance for the conducted diffusion experiments in the frame of this work, it turned out that even decontamination procedures are not necessarily sufficient in removing contamination to the extent of satisfying the requirements for laboratory-scale experiments involving ultra-trace levels of radionuclides.

Tab. 19 Count rates of ^{233}U, ^{237}Np, ^{243}Am, and ^{248}Cm [cts/s] in glovebox and preparatory box background samples. Each ctr was determined as average of four samples.

Sample	Ctr(^{233}U) / s^{-1}	Ctr(^{237}Np) / s^{-1}	Ctr(^{243}Am) / s^{-1}	Ctr(^{248}Cm) / s^{-1}
Glovebox background	$(1.9\pm1.9)\times10^{-4}$	$(9.3\pm1.3)\times10^{-1}$	0	0
Preparatory box background	$(6.8\pm3.0)\times10^{-4}$	$(2.0\pm0.2)\times10^{-2}$	0	0
Background reported by Glückman *et al.* (2022)[16]	$(1.7\pm3.4)\times10^{-4}$	$(5.4\pm5.9)\times10^{-4}$	–	–

7.1.2 Potential airborne contamination due to abrasive peeling

After removal of the clay blank and clay diffusion samples of diffusion experiment I (126 d) from the corresponding solutions, they were transferred to a separate preparatory box for processing via abrasive peeling. In order to minimize the risk of cross-contamination, the clay blank sample was processed before the clay diffusion sample. Furthermore, the clay diffusion sample was abraded from the distal sample side towards the proximal side, i.e., in the direction of increasing tracer concentrations. Nevertheless, abrasive peeling of the clay diffusion sample inevitably released airborne clay particles, along with attached actinide nuclides, presenting a likely source of background. This is particularly relevant, since the abraded clay segments were dried for 12 h in the same preparatory box, by slightly opening the lids of the centrifuge tubes.

The analysis of the procedural blank samples from diffusion experiment I (126 d) showed fairly high background levels of about 2×10^{-9} mol/m³ and 7×10^{-8} mol/m³ for ^{233}U and ^{243}Am, respectively (**Tab. 20**), given the capability of the AMS device at VERA to determine actinides in OPA down to $\approx 10^{-11}$ mol/m³.[16] Furthermore, much further penetration of the tracers into the OPA cylinder was observed than expected from scoping calculations (see sub-chapter 7.3).

Thus, as a preventive measure against potential cross-contamination by airborne particles, the drying step was skipped and the centrifuge tubes were kept closed in the following diffusion experiments. It shall be noted that skipping of the drying step had no impact on the reliable evaluation of the data, since it was decided to indicate the tracer contents in the clay segments as concentration (mol of tracer per m³ of clay) and not as mol of tracer per kg of clay. Thus, no weighing of the clay segments was required.

7.1.3 Contamination on external surface of sample holder

As already noted in sub-chapter 5.6.4, the external surfaces of clay blank and clay diffusions sample holders in diffusion experiment I (126 d) were cleaned with KODAN® tissues for removal of potential surface contamination prior to segmentation with abrasive peeling. Because of the high background levels of the diffusing tracers and the longer than expected diffusion distances, as described in sub-chapter 7.6.2, it was hypothesized that the cleaning procedure with KODAN® tissues might not be sufficient in completely removing surface attached contamination.

As a preventive measure, in diffusion experiment II (240 d) the external surface of the clay diffusion sample holder was removed to a depth of ≈ 100 µm prior to abrasive peeling (see sub-chapter 6.3.2). **Fig. 35** shows the tracer quantities recovered from the external surface of the sample holder of clay diffusion sample II at three different heights. Sampling positions were at 0–2, 2–10, and 10–18 mm, indicated as horizontal error bars. Vertical error bars represent the obtained tracer quantities per mm². All individual samples showed signals for ^{233}U (green) and ^{243}Am (red) which were significantly higher than the corresponding backgrounds.

For ^{243}Am decreasing quantities were observed in the direction of the distal part of the sample holder (approximately 1.7×10^{-13} to 1.3×10^{-15} mol/mm²). As expected, the proximal part of the sample holder, which was immersed into the pore water during the diffusion experiment showed the highest level. In the case of ^{233}U, the quantities in the respective positions were two to three orders of magnitudes lower than for ^{243}Am. This can be attributed to the less sorbing nature of U(VI) species compared to Am(III). Furthermore, the decrease in ^{233}U quantities was less distinct, with $\approx 1.4 \times 10^{-16}$ mol/mm² at the proximal side and $\approx 4.6 \times 10^{-17}$ mol/mm² at the distal side.

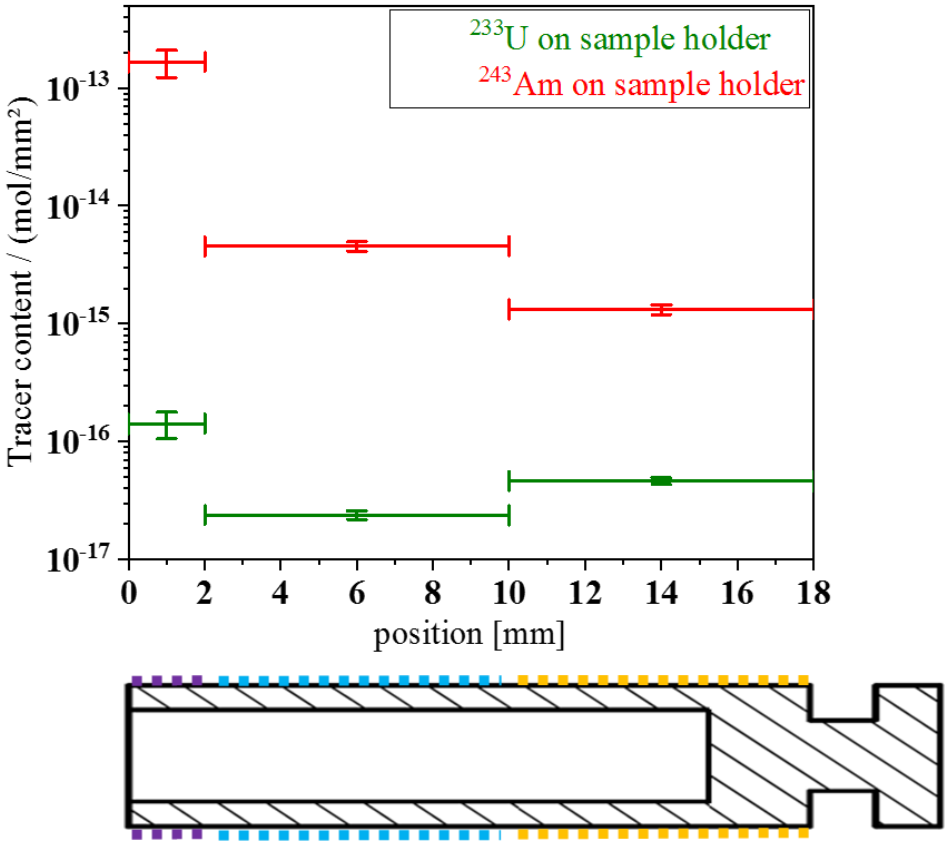

Fig. 35 ^{233}U and ^{243}Am recovered from external surface of diffusion sample holder at three different positions: sampling was performed at heights of 0–2, 2–10, and 10–18 mm, highlighted as purple, light blue, and orange dotted lines, respectively.

7.1.4 Discussion of sources of background and cross-contamination

Laboratory background introduced prior to the diffusion experiments was ruled out as source of high blank levels, as explained in sub-chapter 7.1.1. Preventive measures, such as skipping of the drying step and performing abrasive peeling in glove bags inside a clean exhaust hood (sub-chapter 6.3.1) showed minimal to no effect on the background levels: In case of ^{233}U, background levels decreased from $\approx 10^{-9}$ mol/m³ (diffusion experiment I (126 d)) to $\approx 10^{-10}$ mol/m³ (diffusion experiment II (240 d)), while for ^{243}Am the background was $\approx 10^{-7}$ mol/m³ in both experiments. During diffusion experiments III (20 d) and IV (36 d) background levels of $\approx 10^{-10}$ mol/m³ were found for both ^{233}U and ^{243}Am. It shall be stressed that the fairly low background of ^{243}Am in such experiments is most likely due to the almost three orders of magnitudes lower initial ^{243}Am concentrations in the diffusion reservoir solution compared to diffusion experiments I (126 d) & II (240 d) ($\approx 3 \times 10^{-9}$ mol/L vs. $\approx 1 \times 10^{-12}$ mol/L).

It is hypothesized that the most probable source of ^{233}U and ^{243}Am background is the release of the actinide tracers along with water vapor rising from the diffusion reservoir solution. This hypothesis is supported by the fact that significant amounts of the two tracers, in particular ^{243}Am, were detected also on parts of the PMMA surface which were not in direct contact with the pore water (**Fig. 35**).

Furthermore, it was shown that the external surface of the PMMA sample holder of the clay diffusion sample, having been in direct contact with the diffusion reservoir solution during the diffusion experiment, was a carrier of sorbed ^{233}U and ^{243}Am. During abrasive peeling such nuclides became part of the abraded clay segments, thus, causing an increase in the ^{233}U and ^{243}Am contents. Hence, the removal of the external surface of the sample holder prior to abrasive peeling is a necessary and effective preventive measure against cross-contamination.

7.1.5 Low AMS count rates of internal standards

The uncertainties of the determined tracer concentrations in the clay segments from diffusion experiment I (126 d) were relatively high. For instance, the determination of the tracers in sample DS-4 (993±59 µm) was associated with a relative uncertainty of 140 % (**Fig. 36**). Sample DS-4 was therefore excluded from further evaluation of the diffusion profile. Such high uncertainties were dominated by the uncertainty of the ctrs obtained for the internal standard ^{248}Cm (**Tab. 20**), caused by the reduction of the AMS ion source´s power output during the measurement of samples DS-4 to DS-10, resulting in a much lower sputtering rate of the analyte, than usual. The reduction in power was necessary due to very high signal intensities on masses 233 u and 243 u (up to 10^6 cts/s), endangering the integrity of the detector.

In the affected samples DS-4 to DS-10 the ctrs of ^{248}Cm were approximately 10^{-3} cts/s or lower, while under normal ion source conditions such ctrs were between 10^{-2} and 10^{-1} cts/s. In case of DS-4, only one count was obtained for ^{248}Cm, rendering internal standardization impossible. In case of DS-10, zero counts were observed for ^{248}Cm. Consequently, the ^{243}Am ctr in sample DS-10 could not be normalized to that of ^{248}Cm. Therefore, the ^{243}Am concentration in DS-10 (**Fig. 36**) was estimated by normalization to the ctr of ^{248}Cm in calibration sample Cal-3. (**Tab. 20**). For this, both Cal-3 and DS-10 were re-measured at normal ion source power output and the ctrs of ^{243}Am and ^{248}Cm were determined. For ^{233}U in sample DS-10 no tracer concentration can be given, since only one count for ^{233}U was obtained during the entire measurement time. This is due to the fact that sample DS-10 was diluted 1:1000 during sample preparation (see sub-chapter 5.10).

Tab. 20 Count rates of ^{233}U, ^{243}Am, and internal standard ^{248}Cm [cts/s] in blank samples (B-1 to B-5), diffusion samples (DS-1 to DS-10), and calibration samples (Cal-1 to Cal-3), and corresponding tracer concentrations [mol/m³]; indicated concentrations in diffusion and calibration samples are blank and CIY corrected and normalized to count rates of internal tracer ^{248}Cm.

Sample name	**Ctr(^{233}U) / s^{-1}**	**^{233}U concentration in sample / (mol/m³)**	**Ctr(^{243}Am) / s^{-1}**	**^{243}Am concentration in sample / (mol/m³)**	**Ctr(^{248}Cm) / s^{-1}**
B-1	$(3.5\pm0.5)\times10^{-2}$	$(2.0\pm0.3)\times10^{-9}$	3.7 ± 0.1	$(1.8\pm0.2)\times10^{-7}$	$(3.0\pm0.3)\times10^{-1}$
B-2	$(1.0\pm0.3)\times10^{-2}$	$(2.8\pm0.9)\times10^{-9}$	$(1.8\pm0.1)\times10^{-1}$	$(3.9\pm0.7)\times10^{-8}$	$(7.5\pm1.3)\times10^{-2}$
B-3	$(1.5\pm0.3)\times10^{-2}$	$(2.1\pm0.4)\times10^{-9}$	$(2.9\pm0.1)\times10^{-1}$	$(3.1\pm0.3)\times10^{-8}$	$(1.3\pm0.1)\times10^{-1}$
B-4	$(4.1\pm1.8)\times10^{-3}$	$(5.1\pm2.3)\times10^{-10}$	$(2.4\pm0.1)\times10^{-1}$	$(2.5\pm0.3)\times10^{-8}$	$(1.4\pm0.2)\times10^{-1}$
B-5	$(1.5\pm0.1)\times10^{-1}$	$(2.6\pm0.3)\times10^{-10}$	$(4.2\pm0.2)\times10^{-1}$	$(3.8\pm0.4)\times10^{-8}$	$(2.4\pm0.2)\times10^{-1}$
Mean of Blanks	$(4.2\pm5.3)\times10^{-2}$	$(1.5\pm1.0)\times10^{-9}$	$(1.0\pm1.4)\times10^{-1}$	$(6.2\pm2.7)\times10^{-8}$	$(1.8\pm0.8)\times10^{-1}$
DS-1	$(9.9\pm1.1)\times10^{-2}$	$(2.3\pm0.6)\times10^{-8}$	6.2 ± 0.1	$(1.3\pm0.3)\times10^{-6}$	$(6.2\pm1.5)\times10^{-2}$
DS-2	$(3.6\pm0.2)\times10^{-1}$	$(6.2\pm0.8)\times10^{-8}$	$(7.8\pm0.1)\times10^{1}$	$(8.8\pm1.5)\times10^{-6}$	$(1.3\pm0.2)\times10^{-1}$
DS-3	$(1.4\pm0.1)\times10^{1}$	$(8.7\pm1.7)\times10^{-6}$	$(1.4\pm0.1)\times10^{2}$	$(5.3\pm1.3)\times10^{-5}$	$(6.2\pm1.5)\times10^{-2}$
DS-4	$(4.8\pm0.1)\times10^{1}$	$(7.5\pm8.1)\times10^{-4}$	$(5.7\pm0.1)\times10^{0}$	$(3.8\pm4.0)\times10^{-5}$	$(4.3\pm6.1)\times10^{-4}$
DS-5	$(2.8\pm0.1)\times10^{1}$	$(4.2\pm2.1)\times10^{-4}$	$(2.6\pm0.1)\times10^{0}$	$(5.6\pm7.9)\times10^{-4}$	$(1.4\pm0.9)\times10^{-3}$
DS-6	$(2.8\pm0.1)\times10^{1}$	$(8.4\pm5.5)\times10^{-4}$	$(2.8\pm0.1)\times10^{1}$	$(2.4\pm1.6)\times10^{-4}$	$(8.8\pm7.6)\times10^{-4}$
DS-7	$(3.3\pm0.1)\times10^{1}$	$(7.1\pm4.7)\times10^{-4}$	$(1.5\pm0.1)\times10^{2}$	$(5.2\pm4.5)\times10^{-3}$	$(9.0\pm7.8)\times10^{-4}$
DS-8	$(1.9\pm0.1)\times10^{1}$	$(1.5\pm0.6)\times10^{-4}$	$(4.0\pm0.1)\times10^{2}$	$(2.1\pm1.8)\times10^{-2}$	$(2.7\pm1.5)\times10^{-3}$
DS-9	$(8.6\pm0.3)\times10^{-1}$	$(1.1\pm0.4)\times10^{-4}$	$(3.9\pm0.1)\times10^{2}$	$(3.0\pm1.3)\times10^{-2}$	$(2.7\pm1.2)\times10^{-3}$
DS-10	$(1.1\pm1.5)\times10^{-3}$	– *)	1.0 ± 0.1 **)	$(6.3\pm0.6)\times10^{-2}$	– *)
Cal-1	$(5.7\pm0.3)\times10^{-1}$	***)	–	***)	–
Cal-2	$(2.9\pm0.2)\times10^{-1}$		–		–
Cal-3	$(3.5\pm0.3)\times10^{-1}$		–		–
Cal-3 (re) **)	–		$(1.7\pm0.1)\times10^{-1}$		$(4.5\pm0.4)\times10^{-2}$

*) No tracer concentration can be given, since only one count of mass 233 u and zero counts of 243 u was registered. **) Ctr of ^{243}Am was obtained during re-measurement of DS-10 at normal ion source power output. Ctr was still low due to 1:1000 dilution of analyte (see sub-chapter 5.10). Cal-3 (re): Indicated ctrs were determined during re-measurement of Cal-3 at normal ion source power output and used for normalization of ^{243}Am in DS-10. ***) Each calibration sample nominally contained $\approx 10^{-16}$ mol of ^{233}U, ^{243}Am, and ^{248}Cm.

7.1.6 Concentration corrections in diffusion experiment I (126 d)

As described in sub-chapter 7.1.3, the examination of the sample holder´s external surface from diffusion experiment II (240 d) revealed that a significant amount of the tracers was sorbed onto the sample holder. Since the clay diffusion sample from experiment I (126 d) was abraded without prior removal of the sample holder´s external surface, an overestimation of the tracer concentrations in the abraded clay segments, especially in the case of strongly sorbing ^{243}Am(III) species, was concluded. In order to correct for the excess tracer contents in the abraded segments, the sample holder associated tracer quantities obtained from diffusion experiment II (240 d) (see sub-chapter 7.1.3) were subtracted from the tracer quantities in the clay segments obtained from diffusion experiment I (126 d). After correction, tracer concentrations in segment DS-1 (8908±190 µm) of ^{233}U and ^{243}Am were consistent with the background (**Fig. 36**). Corrected tracer concentrations in segment DS-2 (5596±174 µm) were lower by a factor of 2 to 10. Between segment DS-3 and DS-10 (approximately 2972 µm to 0 µm) corrected and non-corrected concentrations were practically identical.

Hence, the performed corrections were especially relevant for segments located at the distal side of the clay cylinder, i.e., low tracer concentrations, while for higher tracer concentrations towards the proximal sample side the relative contribution of sample holder contamination was negligible.

The corrected concentrations profiles of ^{233}U(IV) and ^{243}Am(III) will be further discussed in sub-chapter 7.6.2.

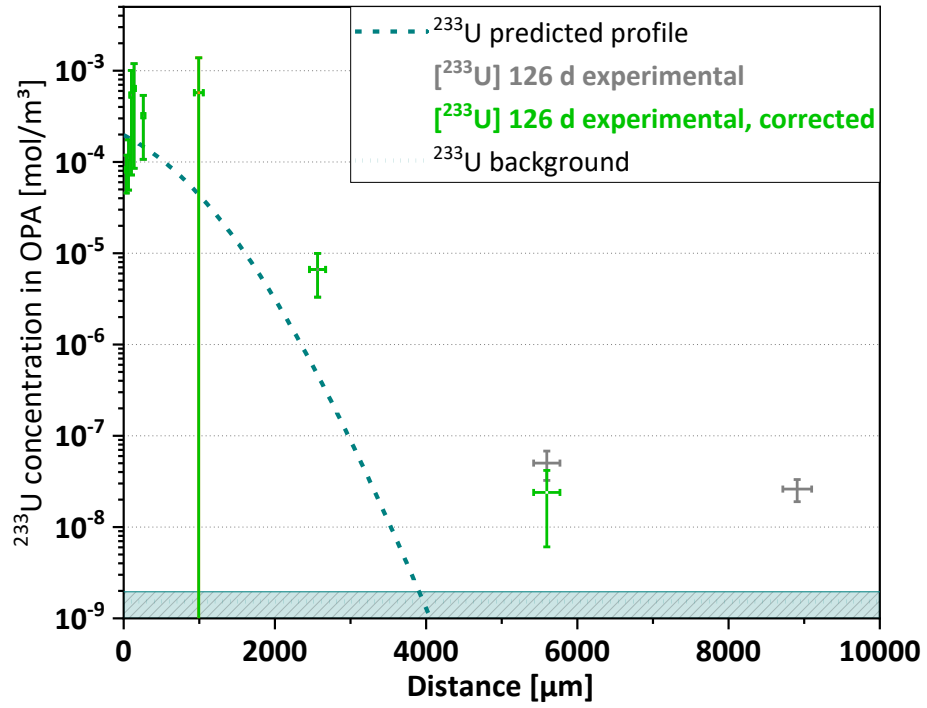

a)

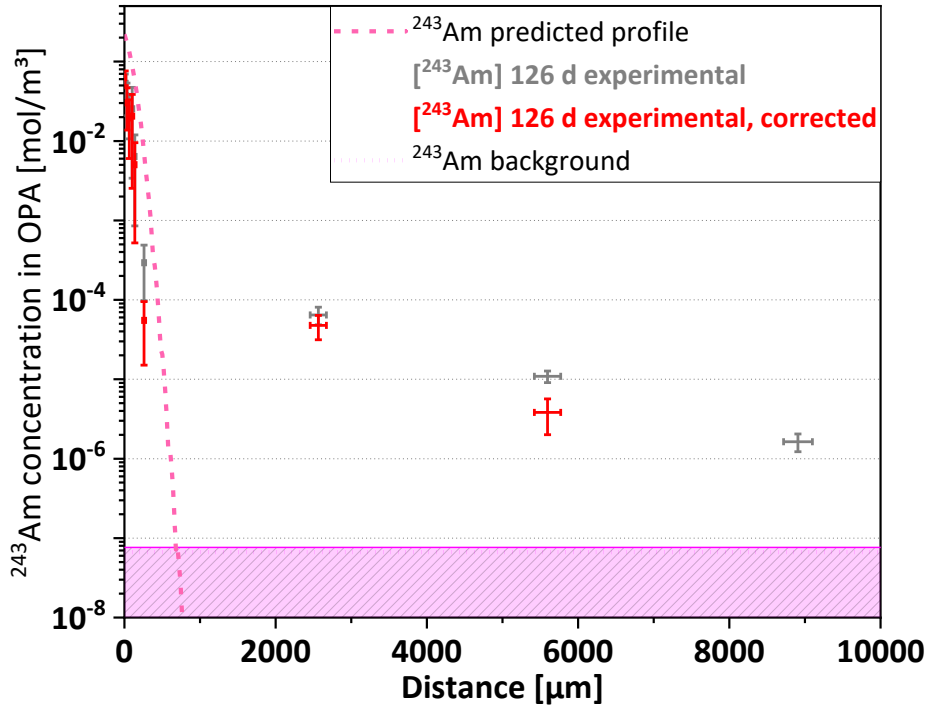

b)

Fig. 36 Diffusion profiles of **a)** ^{233}U and **b)** ^{243}Am in OPA after 126 d of diffusion. Predicted profiles are shown as dashed lines, experimentally obtained data points as grey error bars. Green and red error bars represent the profiles of ^{233}U and ^{243}Am, respectively, after correction for excess tracer previously sorbed onto the external surface of the sample holder.

7.2 Speciation of U(VI) and Am(III) in OPA pore water

The results of the predictive speciation calculations will be commented in terms of the speciation of U and Am under the foreseen experimental conditions and the concentrations of the several actinide species (**Tab. 21**). For U, the dominating oxidation state was +VI, with a total solubility of $(6.90\pm0.7) \times 10^{-4}$ mol/L. The presence of U(IV) species was found to be negligible under the given redox conditions ($E_h = -60$ mV (SHE)) with a total solubility of 3.2×10^{-9} mol/L. Due to the presence of Ca^{2+} and CO_3^{2-} in the pore water, the formation of U(VI) carbonato complexes with stoichiometries $Ca_{2-x}UO_2(CO_3)_3^{-2x}$ ($0 \leq x \leq 1$) is favored at pH = 7.24, as shown in **Fig. 37**. For higher pH values, U(VI) calcium carbonate complexes become less dominant due to the precipitation of calcite, while $[(UO_2)_2(CO_3)(OH)_3]^-$ becomes increasingly dominant.

In case of Am, the only relevant oxidation state was +III, with a total solubility concentration of $(6.16\pm0.6) \times 10^{-6}$ mol/L (**Tab. 21**). For Am also a carbonato complex ($[Am(CO_3)]^+$) is the dominant aquatic species at pH = 7.24 (**Fig. 38**). To a lesser extent (21 %), the aquo ion Am^{3+} (aq.) is present. With increasing pH, also for Am(III) the carbonato complex decreases in dominance, while the cationic hydroxo complex $[Am(OH)_2]^+$ becomes more dominant .

Tab. 21 Calculated solubilities, dominant aquatic species of U(VI) and Am(III) and their respective fractions in OPA pore water in equilibrium with their respective solid phases.

Actinide tracer	Solubility concentration / (mol/L)	Dominant aquatic species	Fraction / %	Solid phase
U(VI)	$(6.90\pm0.7) \times 10^{-4}$	$Ca_2UO_2(CO_3)_3$ (aq.)	57	$UO_2 \cdot 2H_2O$ (am.)
		$[CaUO_2(CO_3)_3]^{2-}$	30	
Am(III)	$(6.16\pm0.6) \times 10^{-6}$	$[Am(CO_3)]^+$	58	$Am(CO_3)(OH)$ (am.)
		Am^{3+} (aq.)	21	

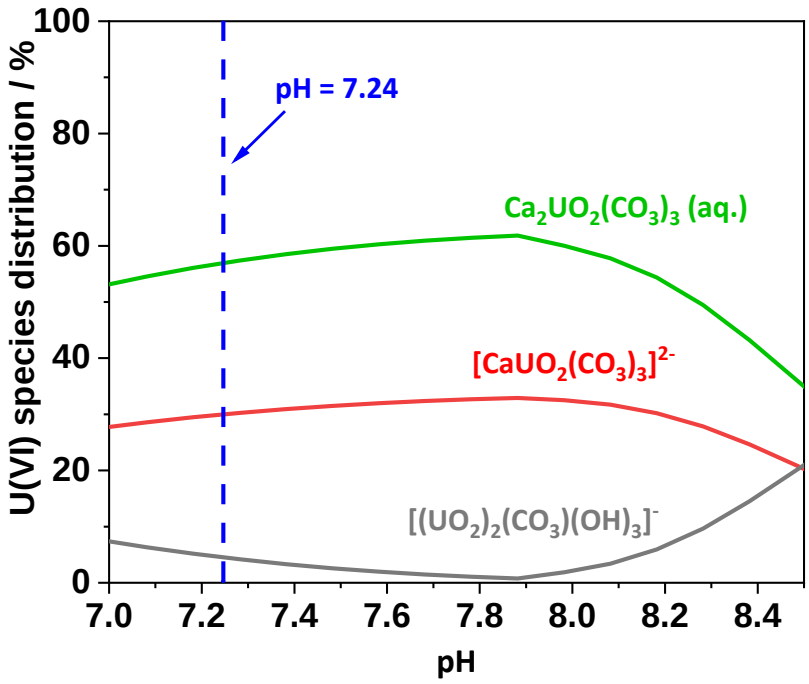

Fig. 37 Calculated speciation of U(VI) as function of pH in synthetic OPA pore water (Tab. 9). Only species > 5 % are shown. For pH 7–8, DIC concentrations were assumed to be constant. For pH ≥ 8, depletion of CO_3^{2-} due to the precipitation of calcite was taken into account.

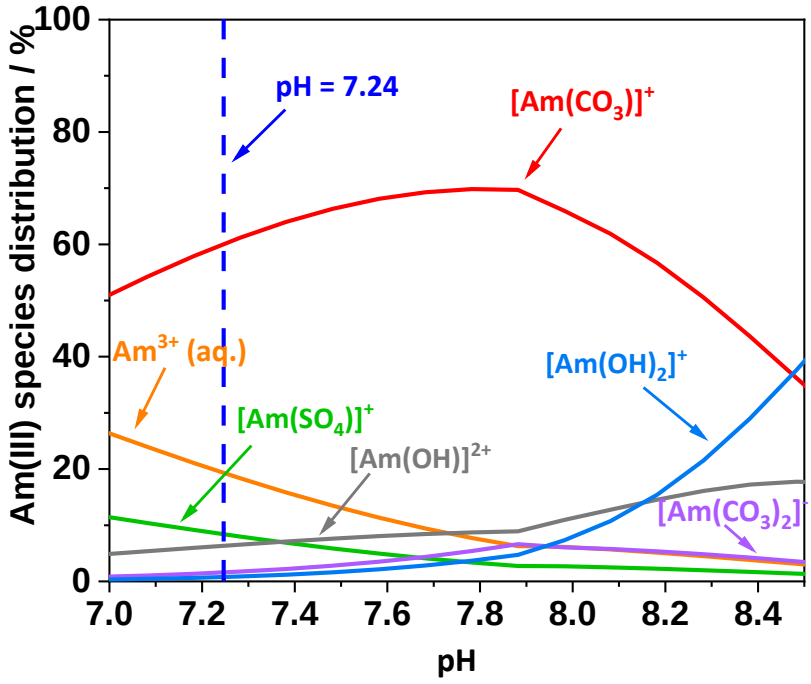

Fig. 38 Calculated speciation of Am(III) as function of pH in synthetic OPA pore water (**Tab. 9**). Only species > 5 % are shown.

7.3 Scoping calculations of U(VI) and Am(III) diffusion profiles in OPA

In order to estimate, at which maximum diffusion distances the diffusing tracers would be still detectable with SF–ICP–MS and AMS, LODs for actinide determination were estimated. In a previous study, exploring the concurrent analysis of ultra-trace levels of actinides, such as U and Am,[16] the AMS determination of such nuclides was possible down to approximately 10^{-18} mol per 0.1 g of OPA (i.e., 10^{-17} mol/g). Applying an OPA density of 2450 kg/m³, the LOD for AMS determination of the actinide tracers is approximately 3×10^{-11} mol/m³ OPA. The SF–ICP–MS device employed in this study typically allows for actinide determination down to $\approx 10^{-13}$ mol/L. Taking into account the necessary dilution of sample solutions,[16] an LOD of approximately 5×10^{-6} mol/m³ OPA is to be expected for ICP–MS determination of the actinide tracers.

The simulated diffusion profiles of U(VI) and Am(III) and the expected maximum diffusion distances after 120, 240, and 480 d of diffusion are shown in **Fig. 39**. Data for D_e and K_d were taken from the literature (see **Tab. 10**). The calculated diffusion profiles of U(VI) start at a concentration of approximately 2×10^{-4} mol/m³ of OPA, while the Am(III) profiles start at 2×10^{-1} mol/m³. This is three orders of magnitudes higher compared to U(VI) and can be explained with the much higher K_d value for the Am(III) species sorption onto OPA.

As to be expected, the diffusion distance increases with increasing experimental time and as a consequence, the profiles become flatter. For a given experimental time, the Am(III) profile is steeper, due to the strongly sorbing nature of cationic Am(III) species and, consequently, the D_a is lower compared to that of neutral or anionic U(VI) species.

The model suggested that U(VI) should be detectable with AMS up to 4.9 mm, 6.9 mm, and 10 mm (i.e., the complete sample length) for diffusion times of 120, 240, and 480 d, respectively. For the mentioned diffusion times, Am(III) is expected to be detectable with AMS up to 1.0, 1.3, and 1.7 mm, respectively. Based on the modeling results, it was decided that the first laboratory-scale diffusion experiment in the frame of this study should be run for approximately 120 d.

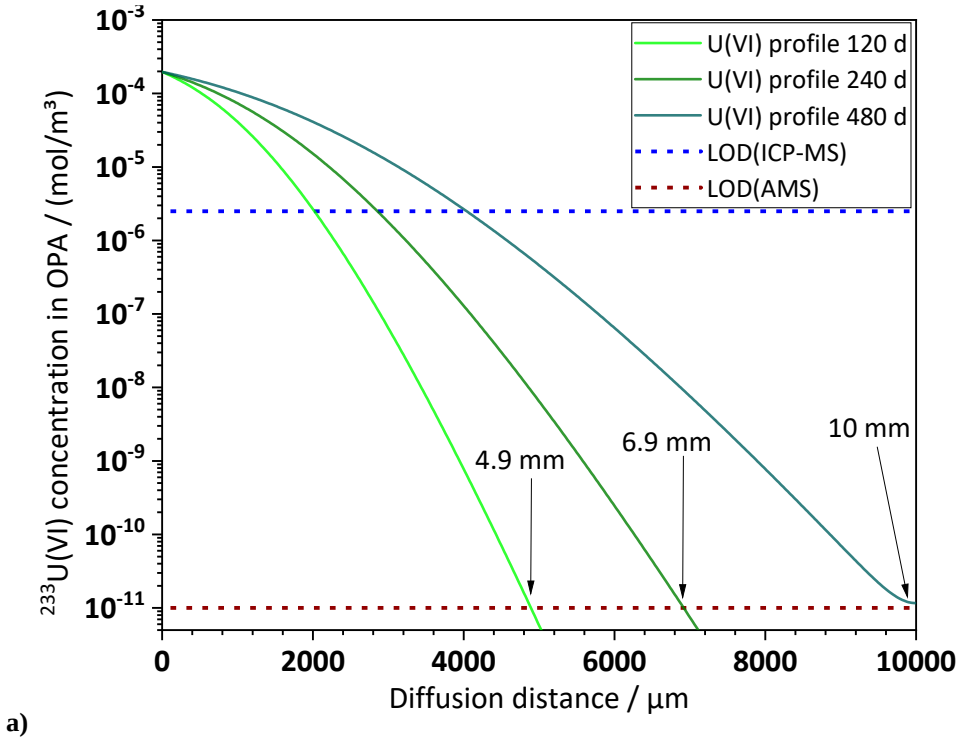

a)

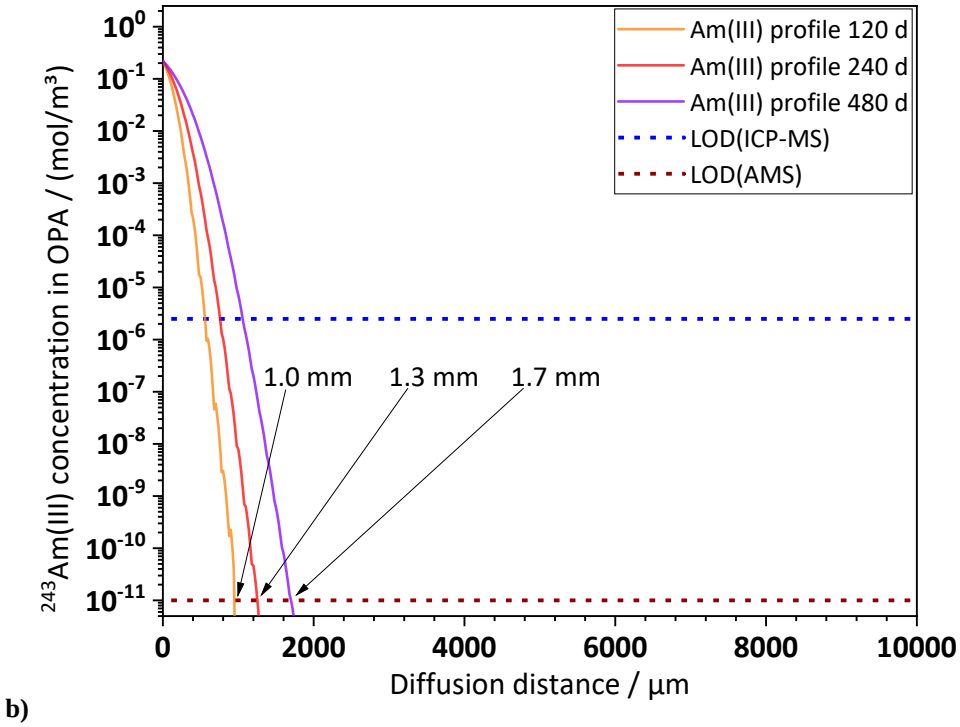

b)

Fig. 39 Simulated diffusion profiles of **a)** U(VI) and **b)** Am(III) in cylindrical OPA sample with a diameter of 6 mm, after 120, 240, and 480 d of diffusion. LODs of ICP–MS and AMS are indicated with blue and brown dashed lines, respectively.

7.4 Determination of tracer sorption onto equipment components

Before reaching equilibrium after approximately 17 d, ^{233}U(VI) and ^{243}Am(III) concentrations in the diffusion reservoir decreased by approximately 10 % and 59 %, respectively (**Fig. 40**). Equilibrium concentrations after 53 d amounted to (4.50±0.23) × 10^{-9} mol/L for ^{233}U(VI) and (3.96±0.32) × 10^{-9} mol/L for ^{243}Am(III), due to sorption to the surfaces of the reservoir cell. Within 53 d, the pH increased from initially 7.2±0.1 to 8.2±0.1.

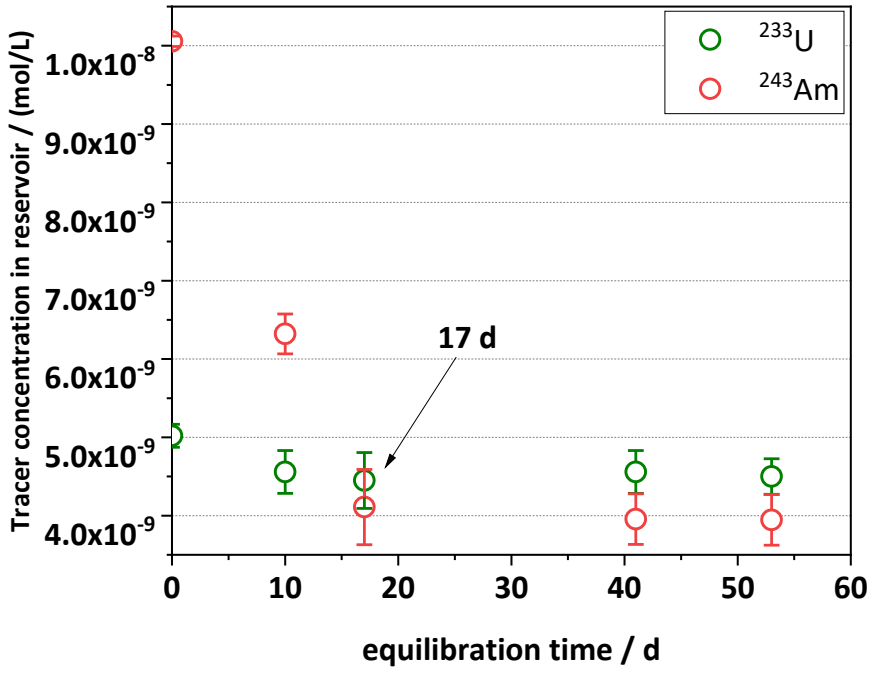

Fig. 40 Evolution of ^{233}U and ^{243}Am concentrations in PMMA reservoir containing OPA pore water.

7.5 Decreased dissolved inorganic carbon inventory due to degassing of CO_2

Similarly to the pH shift during the equipment sorption test, a considerable increase in pH from initially 7.2±0.1 to 8.4±0.1 and 8.3±0.1 was observed during equilibration of the diffusion reservoirs water of experiments I/II and III/IV, respectively (see sub-chapters 7.6.1 and 7.8.1). This can be attributed to the gradual degassing of CO_2, since the experiments were not performed under constant CO_2 partial pressure. DIC analysis of the reservoir solution of diffusion experiments III/IV confirmed a substantial decrease in CO_3^{2-}/HCO_3^- concentrations from initially (2.7±0.1) × 10^{-3} mol/L to as low as (8.1±0.3) × 10^{-5} mol/L (**Tab. 22**). During 36 d of diffusion the DIC concentration remained practically constant at ≈ 10^{-4} mol/L. Such decreased DIC concentrations had an effect on the aqueous speciation of the diffusing tracers

during the diffusion experiments as it will be discussed in the corresponding sub-chapters 7.6 to 7.8.

Tab. 22 DIC concentrations in diffusion reservoir solution of diffusion experiments III (20 d) & IV (36 d) during conditioning (Pore $water_{cond}$ / (mol/L)) and during diffusion experiment (Pore $water_{diff}$ / (mol/L)).

	Pore $water_{cond=2h}$ / (mol/L)	**Pore $water_{diff=0d}$ / (mol/L)**	**Pore $water_{diff=15d}$ / (mol/L)**	**Pore $water_{diff=20d}$ / (mol/L)**	**Pore $water_{diff=36d}$ / (mol/L)**
CO_3^{2-}/HCO_3^- / (mol/L)	$(2.7\pm0.1) \times 10^{-4}$	$(8.1\pm0.3) \times 10^{-5}$	$(1.1\pm0.2) \times 10^{-4}$	$(1.2\pm0.2) \times 10^{-4}$	$(1.3\pm0.1) \times 10^{-4}$

7.6 U(VI) and Am(III) diffusion profiles after 126 d (experiment I)

7.6.1 Characterization of the reservoir solution

After conditioning for 56 d, the reservoir solution concentrations of $^{233}U(VI)$ and $^{243}Am(III)$ decreased to $(3.22\pm0.13) \times 10^{-9}$ mol/L and $(3.03\pm0.10) \times 10^{-9}$ mol/L, respectively, due to sorption onto the diffusion reservoir wall and setup components. The measured concentrations are quite comparable to those measured in the equipment sorption test (see sub-chapter 7.4). The concentrations of alkaline and earth alkaline cations in the saturation vessel remained practically constant during 126 d. The same was true for Cl^- and SO_4^{2-} concentrations. The pH increased slightly from 7.2±0.1 to 7.8±0.1 after 56 d. After 126 d a pH of 7.6±0.1 was determined.

In the diffusion reservoir solution, the concentrations of the pore water matrix cations, as well as of Cl^- and SO_4^{2-} were steady. The strong increase of the pH from initially 7.3±0.1 to 8.4±0.1 after 56 d resulted in a decrease of the concentration of inorganic carbon (**Tab. 23**). Such shift in pH is explained by degassing of CO_2 (see sub-chapter 7.5). However, after insertion of the two OPA specimens into the diffusion reservoir solution after 56 d, the pH dropped and stabilized at 7.8±0.1, which can be attributed to buffering of the CO_3^{2-}/HCO_3^- system due to dissolution of carbonate bearing minerals in OPA such as calcite, dolomite, and siderite.

In order to assess potential changes in the radionuclide tracers´ speciation due to the increase of pH and the resulting change in CO_3^{2-} concentration, speciation calculations were performed with PHREEQC, based on the experimentally observed pore water chemistry. The calculations suggested that the speciation of U(VI) and Am(III) has not significantly changed during the diffusion experiment. The dominant aquatic U species were the neutral $Ca_2UO_2(CO_3)_3$ (aq.) and

the anionic $[Ca(UO_2)(CO_3)_3]^{2-}$ (**Tab. 24**). In case of Am, the cationic $[Am(CO_3)]^+$ and the Am^{3+} aquo ion were predominant. However, after 56 d of conditioning (i.e., 0 d of diffusion: shortly before immersion of the OPA specimens into the diffusion reservoir solution), the pH was fairly high (8.4±0.1), favoring the formation of the hydroxo complex $[Am(OH)_2]^+$ over the Am^{3+} aquo ion.

Tab. 23 Diffusion experiment I (126 d): pore water composition in diffusion reservoir solution, I_t and pH during conditioning (Pore water$_{cond}$ / (mol/L)) and diffusion experiment (Pore water$_{diff}$ / (mol/L)).

Ion	**Pore water$_{cond=2h}$ / (mol/L)**	**Pore water$_{cond=56d}$ / (mol/L)**	**Pore water$_{diff=71d}$ / (mol/L)**	**Pore water$_{diff=126d}$ / (mol/L)**
Na^+	$(1.52\pm0.01) \times 10^{-1}$	$(7.35\pm0.02) \times 10^{-2}$	$(1.22\pm0.03) \times 10^{-1}$	$(1.07\pm0.01) \times 10^{-1}$
K^+	$(8.70\pm0.30) \times 10^{-4}$	$(6.93\pm0.28) \times 10^{-4}$	$(1.21\pm0.06) \times 10^{-3}$	$(1.01\pm0.02) \times 10^{-3}$
Mg^{2+}	$(2.19\pm0.01) \times 10^{-2}$	$(1.12\pm0.08) \times 10^{-2}$	$(1.04\pm0.02) \times 10^{-2}$	$(9.37\pm0.06) \times 10^{-3}$
Ca^{2+}	$(8.42\pm0.10) \times 10^{-3}$	$(8.39\pm0.09) \times 10^{-3}$	$(1.57\pm0.03) \times 10^{-2}$	$(1.38\pm0.07) \times 10^{-2}$
Sr^{2+}	$(4.51\pm0.01) \times 10^{-4}$	$(5.01\pm0.04) \times 10^{-4}$	$(4.62\pm0.04) \times 10^{-4}$	$(4.10\pm0.03) \times 10^{-4}$
SO_4^{2-}	$(9.3\pm1.9) \times 10^{-3}$	$(9.5\pm1.4) \times 10^{-3}$	$(9.6\pm1.8) \times 10^{-3}$	$(9.6\pm1.4) \times 10^{-3}$
Cl^-	$(1.8\pm0.3) \times 10^{-1}$	$(1.5\pm0.3) \times 10^{-1}$	$(1.7\pm0.4) \times 10^{-1}$	$(1.8\pm0.4) \times 10^{-1}$
I_t	0.23±0.03	0.20±0.02	0.21±0.02	0.20±0.02
pH	7.3±0.1	8.4±0.1	7.8±0.1	7.8±0.1

Tab. 24 Dominant aquatic species of U(VI) and Am(III) in OPA pore water during diffusion experiment I (126 d) at the time of sampling.

Actinide tracer	**Pore water$_{diff=0d}$ / (mol/L)**	**Pore water$_{diff=71d}$ / (mol/L)**	**Pore water$_{diff=126d}$ / (mol/L)**
U(VI)	$Ca_2UO_2(CO_3)_3$ (aq.) $[Ca(UO_2)(CO_3)_3]^{2-}$	Unchanged	Unchanged
Am(III)	$[Am(CO_3)]^+$ $[Am(OH)_2]^+$	$[Am(CO_3)]^+$ Am^{3+} (aq.)	$[Am(CO_3)]^+$ Am^{3+} (aq.)

7.6.2 Discussion of the U(VI) and Am(III) diffusion profile

In **Fig. 41** the experimentally determined ^{233}U(VI) and ^{243}Am(III) diffusion profiles are shown after 126 d. Note that the experimental data has been corrected for cross-contamination effects

as described and discussed in sub-chapter 7.1.6. The corresponding background levels are given as 2 σ confidence intervals. Background levels of $(1.5\pm2.0) \times 10^{-9}$ mol/m³ and $(6.7\pm7.7) \times 10^{-8}$ mol/m³ were obtained for ^{233}U and ^{243}Am, respectively, and are illustrated as shaded areas. Vertical error bars, also given as 2 σ confidence intervals, indicate the propagated uncertainty of the tracer concentration. Such propagated uncertainty was mainly influenced by the uncertainty of the corresponding AMS measurement, in particular the uncertainty of the ctrs of the internal standard ^{248}Cm. Horizontal error bars indicate the thickness of an abraded segment (20–380 µm), in which the nuclide content was analyzed, including a relative uncertainty of up to 2 %, caused by the micrometer used for layer thickness determinations. The position of a data point z is given by the following formula:

$$z = x_{i,\text{before}} - 0.5\Delta x_i \pm \Delta x_i \qquad \textbf{Eq. 21}$$

where $x_{i,\text{ before}}$ [µm] is the sample position before abrasion and Δx_i is the thickness of the abraded segment i.

Both ^{233}U(VI) and ^{243}Am(III) were detectable down to about 5770 µm at levels significantly higher than background. A much further penetration of both tracers into the clay was observed, than expected from scoping calculations (see sub-chapter 7.3), as shown in **Fig. 41**.

The diffusion profile of ^{233}U(VI) was determined down to concentration levels of approximately 5×10^{-8} mol/m³ (**Fig. 41a**). ^{233}U(VI) concentrations were practically constant over the first 280 µm, ranging between 10^{-3} mol/m³ and 10^{-4} mol/m³. A strong decrease of the ^{233}U(VI) concentration followed between 2456 µm and 5770 µm. The determined D_e value was higher by approximately a factor of four compared to the value reported by Joseph *et al.* (2013),[2] which can be attributed to the differences in bedding direction and confining pressure. As explained in sub-chapter 3.2.2, diffusion parallel to the bedding is known to be more rapid than perpendicular to the bedding. Furthermore, the absence of confining pressure could have caused a higher diffusion-accessible porosity, resulting in a higher D_e. The determined K_d value of ≈ 0.05 m³/kg was higher by a factor of two compared to the literature data (**Tab. 25**),[2] but also afflicted with a relatively high uncertainty. However, a difference by a factor of two can be considered a good agreement, given the high sensitivity of U(VI) sorption towards slight pH changes in the circumneutral to alkaline range.[97]

The diffusion profile of ^{243}Am(III) was featured by two different sections (**Fig. 41b**). The first section (hereafter referred to as slow-diffusing species profile) exhibited a steep decrease in

^{243}Am(III) concentration from about 5×10^{-2} mol/m³ to 10^{-4} mol/m³ up to approximately 280 µm. The second section of the profile (hereafter referred to as fast-diffusing species profile) showed a much less distinct decrease in concentration, from approximately 10^{-4} mol/m³ to 2×10^{-6} mol/m³ toward the distal side of the sample (up to 5770 µm).

Such profile tailing was not expected from the scoping calculations. Such tailing was also observed in some cases for Cs(I) and Eu(III) diffusion in illite.[26] A previous study reported a similar behavior of the diffusion profile after an in-diffusion experiment with Eu(III) ($c_0 = 10^{-5}$ mol/m³) through OPA.[3] An initial strong decrease in Eu(III) concentration from around 5×10^{-1} mol/m³ to around 10^{-4} mol/m³ over the first 500 µm was followed by a practically steady profile tailing, fluctuating around 10^{-4} mol/m³ to 10^{-5} mol/m³ (**Fig. 42**). Furthermore, an almost complete depletion of Eu(III) in the diffusion reservoir was reported, indicating the presence of a yet unknown sink for Eu(III). It has not been elucidated yet whether the traces of Eu(III) found for distances > 500 µm represent an artefact or originate from an actual transport process.

The fitting of the slow-diffusing Am(III) species profile amounted to $K_d = 20\pm5$ m³/kg which is in good agreement to the K_d determined by means of a batch sorption experiment with Am(III) and OPA (**Tab. 25**).[51] For the slow-diffusing species profile, a D_a of $(0.22\pm0.05) \times 10^{-16}$ m²/s was found, which is in fairly good agreement with $D_a \approx 0.7 \times 10^{-16}$ m²/s, determined in a diffusion experiment with Eu(III) in OPA.[3] It can be considered a fairly good agreement, since OPA is a natural material with variations in its composition depending on the batch used in the experiments. In addition, differences in specific surface accessibility between compact material and powder clay can also have an impact on the K_d and, consequently, the D_a.[98] D_e and K_d values from fitting the fast-diffusing species profile of Am yielded ≈ 0.20 m^2/s and ≈ 0.15 m^3/kg, respectively.

It shall be pointed out that the presented K_d and D_e values for Am(III) and U(VI) are only indicative. The overall uncertainties of the tracer concentrations determined with AMS were high. Additionally, the corrections for excess tracer originating from the sample holder were based on estimates from diffusion experiment II (240 d), since the actual surface holder contamination from diffusion experiment I (126 d) is unknown, introducing a further source of uncertainty. Furthermore, the number of experimental data points was limited. For instance, between 240 µm and 5770 µm the modelled profile is based on only three data points.

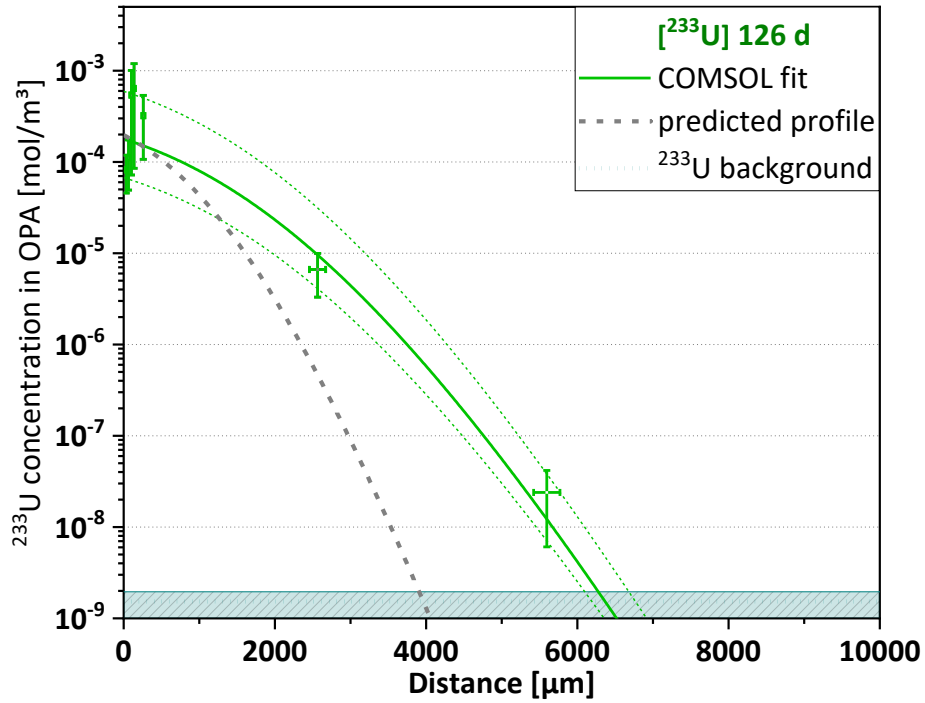

a)

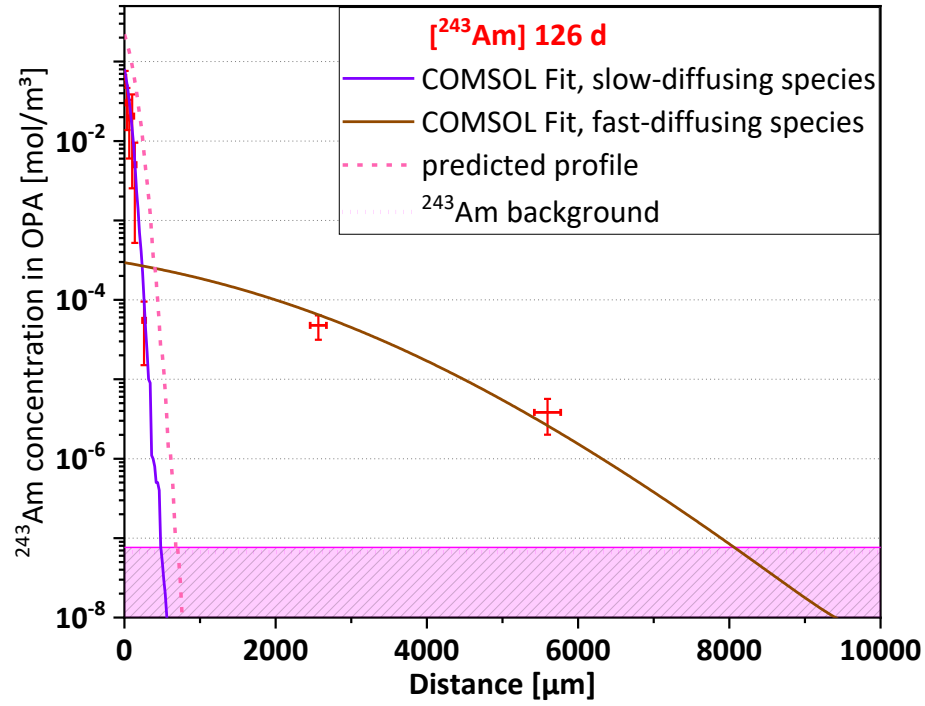

b)

Fig. 41 Tracer concentrations in clay layers in mol of tracer per m³ of OPA after 126 d of diffusion, determined with AMS as function of distance; corresponding background levels are indicated as shaded dark cyan and purple areas. Predicted, experimentally obtained, and modelled diffusion profiles of **a)** ^{233}U and **b)** ^{243}Am.

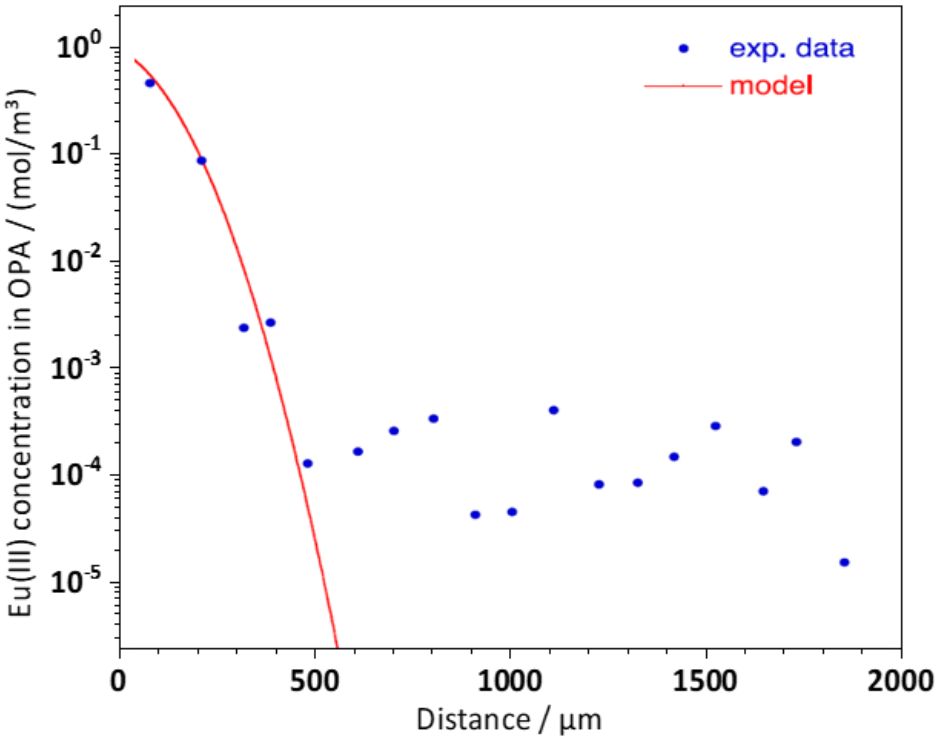

Fig. 42 Experimental and modelled diffusion profiles of Eu(III) in OPA after 200 d of diffusion (adopted from PSI progress report 2019).[3]

Tab. 25 Parameter values for D_e and K_d for ^{233}U and ^{243}Am obtained from diffusion experiment I (126 d); comparison with parameters available from literature.

Parameter	^{233}U(VI) (126 d)	U(VI), literature [2]	^{243}Am(III), slow-diffusing species (126 d)	Slow-diffusing species, literature *)	^{243}Am(III), fast-diffusing species (126 d)
D_e / (× 10^{-10} m²/s)	0.08(+0.04/−0.06)	0.019±0.004	0.11±0.04	≈ 0.15	≈ 0.20
D_a / (× 10^{-16} m²/s)			0.22±0.05	≈ 0.7	
K_d / (m³/kg)	0.05(+0.06/−0.04)	0.025±0.003	20±5	30±2	≈ 0.15

*) D_e from diffusion experiment with Eu(III) in OPA for 200 d.[3] K_d from batch sorption experiment with Am(III) and OPA.[51]

7.7 U(VI) and Am(III) diffusion profiles after 240 d (experiment II)

7.7.1 Characterization of the reservoir solution

As shown in **Tab. 26**, the concentrations of the pore water constituting ions, as well as the pH did not change significantly between the termination of diffusion experiment I (126 d) and experiment II (240 d). Consequently, no considerable changes in the aqueous speciation of

U(VI) and Am(III) were expected, as shown by the corresponding speciation calculations (**Tab. 27**).

Tab. 26 Diffusion experiment II (240 d): pore water composition in diffusion reservoir solution, I_t and pH during diffusion experiment (Pore water$_{diff}$ / (mol/L)).

Ion	**Pore water$_{diff=240d}$ / (mol/L)**
Na^+	$(1.21\pm0.03) \times 10^{-1}$
K^+	$(1.04\pm0.04) \times 10^{-3}$
Mg^{2+}	$(9.87\pm0.09) \times 10^{-3}$
Ca^{2+}	$(1.42\pm0.05) \times 10^{-2}$
Sr^{2+}	$(4.13\pm0.04) \times 10^{-4}$
SO_4^{2-}	$(9.8\pm1.1) \times 10^{-3}$
Cl^-	$(1.9\pm0.3) \times 10^{-1}$
I_t	0.22±0.02
pH	7.9±0.1

Tab. 27 Dominant aquatic species of U(VI) and Am(III) in OPA pore water during diffusion experiment II (240 d) at the time of sampling. For comparability, also compositions, aqueous speciations after 0 d and 126 d of diffusion are also shown.

Actinide tracer	**Pore water $_{diff=0d}$ / (mol/L)**	**Pore water$_{diff=126d}$ / (mol/L)**	**Pore water$_{diff=240d}$ / (mol/L)**
U(VI)	$Ca_2UO_2(CO_3)_3$ (aq.) $[Ca(UO_2)(CO_3)_3]^{2-}$	Unchanged	Unchanged
Am(III)	$[Am(CO_3)]^+$ $[Am(OH)_2]^+$	$[Am(CO_3)]^+$ Am^{3+} (aq.)	$[Am(CO_3)]^+$ Am^{3+} (aq.)

7.7.2 Discussion of the U(VI) and Am(III) diffusion profile

The presented data was obtained from diffusion II (240 d) experiment, in which preventive measures have been taken in order to minimize cross-contamination effects and background, as described in sub-chapter 7.1.

^{233}U(VI) was detectable along the complete clay diffusion sample (8684 µm) down to ultra-trace concentration levels of 10^{-9} mol/m³. The diffusion profile of ^{233}U(VI) is shown in **Fig. 43**.

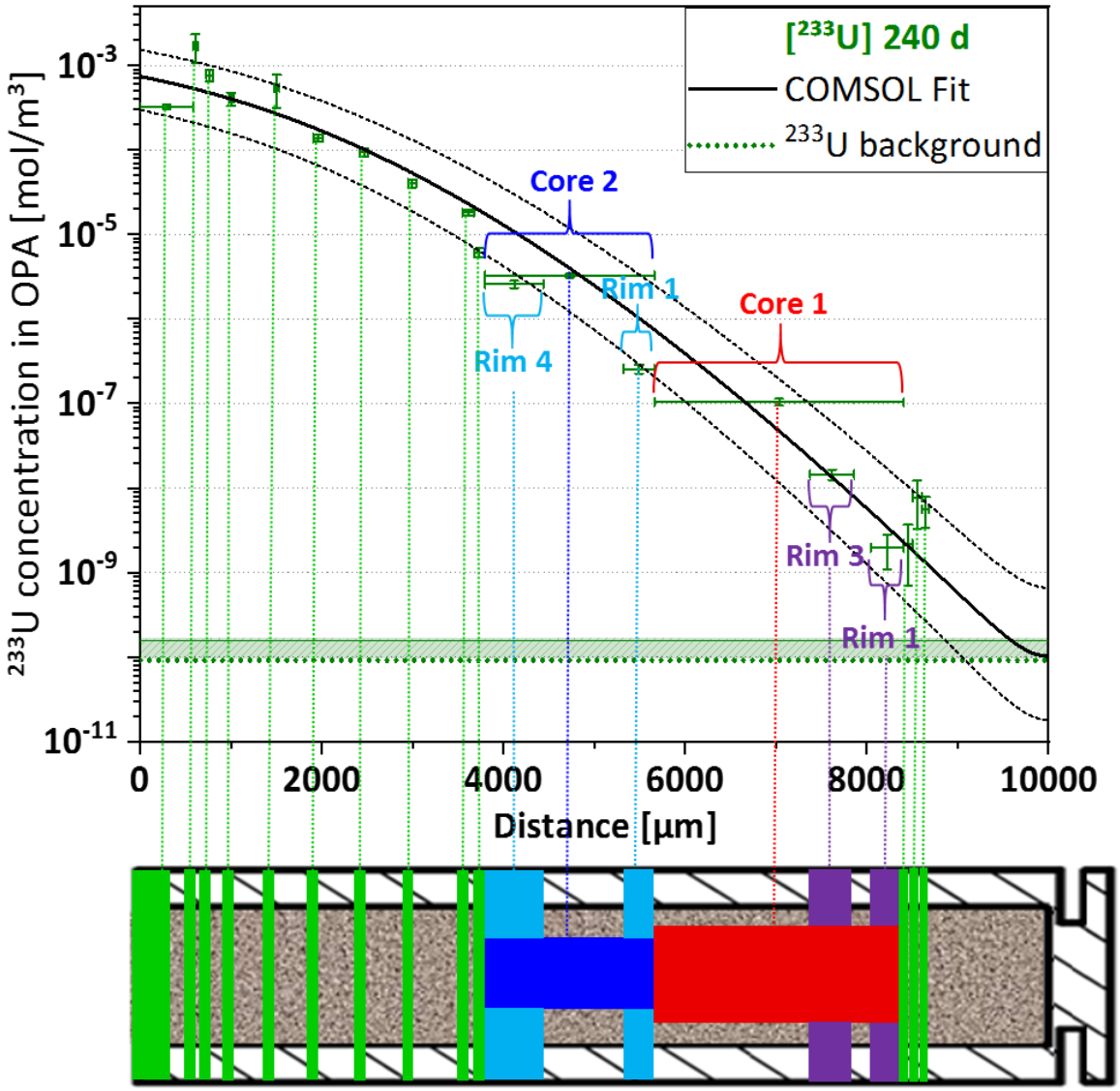

Fig. 43 Diffusion profile of ^{233}U in OPA after 240 d of diffusion (represented as green error bars).

Core and rim segments (see sub-chapter 6.3.3) followed the general trend of decreasing ^{233}U concentrations with diffusion distance in the fully abraded segments, suggesting that no preferential pathways along the rim of the clay diffusion sample occurred. The D_e value of ^{233}U(VI) amounted to $0.16(+0.18/-0.11) \times 10^{-10}$ m²/s (**Tab. 28**) and was higher by approximately one order of magnitude compared to the literature data.[2] As already mentioned for the 126 d experiment, such elevated D_e value of ^{233}U(VI) can be explained by differences in bedding direction and confining pressure between the actual study and the cited study. The determined K_d value of ^{233}U(VI) amounted to 0.10(+0.09/−0.06) m³/kg and was higher by about a factor of four in comparison to the literature data. Taking the uncertainty of the value into

account and considering the already mentioned sensitivity of U(VI) sorption towards slight changes in pH, this value is slightly higher but still in fair agreement with literature data (0.025±0.003 m^3/kg).[2]

For ^{243}Am(III), the diffusion profile was determined down to approximately 10^{-6} mol/m³ and a distance of 4468 µm (**Fig. 44**). For approximately 5690 µm and longer distances the concentrations were consistent with the background (≈ 8×10^{-8} mol/m³). As also observed for diffusion experiment I (126 d), the diffusion profile of ^{243}Am(III) was featured by a slow-diffusing and a fast-diffusing species profile. The slow-diffusing species profile was featured by a rapid decrease in concentration up to approximately 1000 µm, from about 6×10^{-2} mol/m³ to 10^{-5} mol/m³.

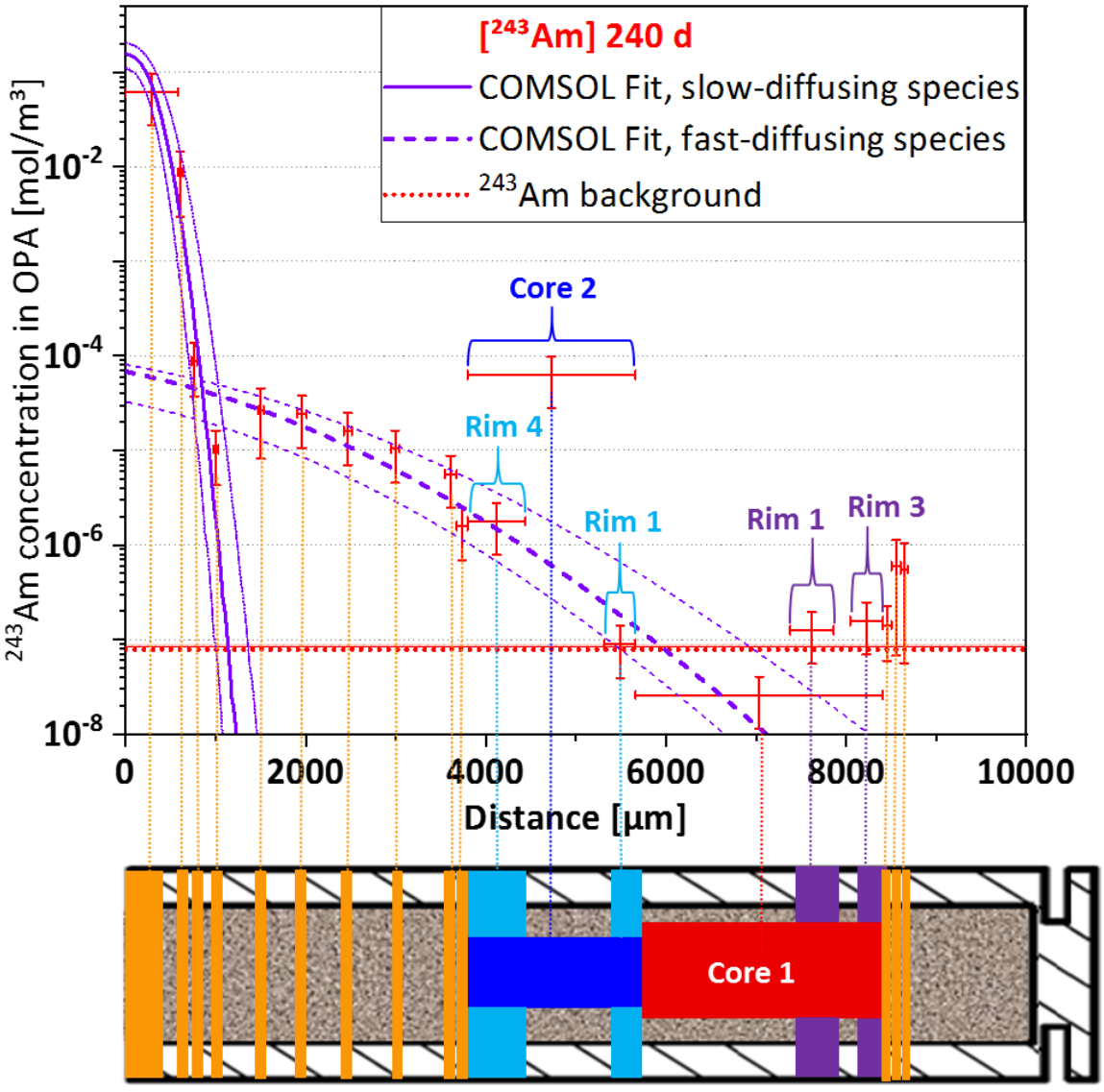

Fig. 44 Diffusion profile of ^{243}Am in OPA after 240 d of diffusion (represented as red error bars).

The fast-diffusing species profile exhibited a much smaller decrease in concentration, from approximately 10^{-5} mol/m³ (≈ 1000 µm) to 10^{-6} mol/m³ (4146 µm). While rim segment 4 of drilled core 2 follows the fast-diffusing species profile´s trend of decreasing ^{243}Am concentrations, for core segment 2 (4756±933 µm), a 40 times higher concentration was observed. There is currently no explanation available for the relatively high Am concentration in core segment 2. For distances longer than 5689 µm the concentrations were consistent with the background.

The fitting of the slow-diffusing Am species profile amounted to K_d = 60±20 m³/kg, which is about a factor of 2 higher compared to the one reported by Amayri *et al.* (2016)[51] obtained by batch sorption experiments. This constitutes a fairly good agreement, since batch-dependent variations in the composition of OPA can have an effect on K_d determination. The D_a of the slow-diffusing species profile amounted to $1.0(+1.5/-0.5) \times 10^{-15}$ m²/s. Within the fit´s uncertainty, this is in agreement with the D_a observed in a diffusion experiment with Eu(III) in OPA.[3] D_e and K_d values obtained from fitting the fast-diffusing species profile of Am(III) amounted to $0.19(+0.16/-0.14) \times 10^{-10}$ m²/s and 0.20(+0.04/−0.11) m³/kg, respectively, and will be discussed in sub-chapter 7.10.

Tab. 28 Parameter values for D_e and K_d for ^{233}U(VI) and ^{243}Am(III) obtained from diffusion experiment II (240 d) of diffusion; comparison with parameters available from literature.

Parameter	**^{233}U(VI) (240 d)**	**U(VI), literature** [2]	**^{243}Am(III), slow-diffusing species (240 d)**	**Slow-diffusing species, literature** *)	**^{243}Am(III), fast-diffusing species (240 d)**
D_e / ($\times 10^{-10}$ m²/s)	0.16(+0.18/−0.11)	0.019±0.004	1.5(+1.0/−0.6)	≈ 0.15	0.19(+0.16/−0.14)
D_a / ($\times 10^{-15}$ m²/s)			1.0(+1.5/−0.5)	≈ 0.7	
K_d / (m³/kg)	0.10(+0.09/−0.06)	0.025±0.003	60±20	30±2	0.20(+0.04/−0.11)

*) D_e and D_a from diffusion experiment with Eu(III) in OPA for 200 d.[3] K_d from batch sorption experiment with Am(III) and OPA.[51]

7.8 U(VI) an Am(III) diffusion profiles after 20 d and 36 d (experiments III and IV)

7.8.1 Characterization of the reservoir solution

Two short term experiments were carried out in order to study the evolution of diffusion profiles over time and to examine the outcome of the longer diffusion experiments. In such short term experiments the concentration of the pore water constituting cations and anions were practically stable during the entire experiment (**Tab. 29**). Due to degassing of CO_2, the pH increased during conditioning from 7.3±0.1 to 8.3±0.1. After insertion of the OPA cylinders, the pH gradually dropped to 8.2±0.1 after 20 d of diffusion (experiment III) and 8.0±0.1 after 36 d of diffusion (experiment IV). Redox potentials of the reservoir solution decreased from +392(±50) mV at the time of initiation of the diffusion experiment to +234(±50) mV after termination (36 d).

Tab. 29 Diffusion experiments III (20 d) & IV (36 d): pore water composition in diffusion reservoir solution, I_t, pH, E_h, and oxygen concentration ([O_2]/ ppm) in glovebox during conditioning (Pore water$_{cond}$ / (mol/L)) and diffusion experiment (Pore water$_{diff}$ / (mol/L)).

Ion	Pore water$_{cond=2h}$ / (mol/L)	Pore water$_{diff=0d}$ / (mol/L)	Pore water$_{diff=15d}$ / (mol/L)	Pore water$_{diff=20d}$ / (mol/L)	Pore water$_{diff=36d}$ / (mol/L)
Na^+	$(1.25\pm0.03) \times 10^{-1}$	$(1.77\pm0.02) \times 10^{-1}$	$(1.11\pm0.02) \times 10^{-1}$	$(1.17\pm0.03) \times 10^{-1}$	$(1.13\pm0.04) \times 10^{-1}$
K^+	$(7.81\pm0.28) \times 10^{-4}$	$(6.92\pm0.21) \times 10^{-4}$	$(2.12\pm0.05) \times 10^{-3}$	$(3.01\pm0.03) \times 10^{-3}$	$(2.51\pm0.02) \times 10^{-3}$
Mg^{2+}	$(2.09\pm0.01) \times 10^{-2}$	$(1.04\pm0.08) \times 10^{-2}$	$(1.01\pm0.04) \times 10^{-2}$	$(9.84\pm0.04) \times 10^{-3}$	$(9.21\pm0.09) \times 10^{-3}$
Ca^{2+}	$(8.31\pm0.11) \times 10^{-3}$	$(8.39\pm0.19) \times 10^{-3}$	$(1.74\pm0.04) \times 10^{-2}$	$(1.39\pm0.05) \times 10^{-2}$	$(1.67\pm0.08) \times 10^{-2}$
Sr^{2+}	$(4.01\pm0.04) \times 10^{-4}$	$(4.45\pm0.03) \times 10^{-4}$	$(4.63\pm0.04) \times 10^{-4}$	$(4.00\pm0.04) \times 10^{-4}$	$(4.21\pm0.07) \times 10^{-4}$
SO_4^{2-}	$(9.0\pm1.7) \times 10^{-3}$	$(9.4\pm1.1) \times 10^{-3}$	$(9.6\pm1.7) \times 10^{-3}$	$(9.7\pm1.3) \times 10^{-3}$	$(9.7\pm1.5) \times 10^{-3}$
Cl^-	$(1.7\pm0.4) \times 10^{-1}$	$(1.6\pm0.3) \times 10^{-1}$	$(1.7\pm0.4) \times 10^{-1}$	$(1.8\pm0.2) \times 10^{-1}$	$(1.7\pm0.3) \times 10^{-1}$
I_t	0.21±0.02	0.22±0.02	0.20±0.02	0.20±0.02	0.20±0.02
E_h (SHE) / mV *)	n.d.	+392	+315	+262	+234
[O_2] / ppm **)	39	25	21	31	21
pH	7.3±0.1	8.3±0.1	8.2±0.1	8.2±0.1	8.0±0.1

n.d.: not determined *) Uncertainty: ±50 mV. **) Uncertainty: ±5 ppm.

Speciation calculations showed consistent with previously described results that the shift in pH during the conditioning and the diffusion experiments had no significant impact on the speciation of U(VI). The dominant species were $Ca_2UO_2(CO_3)_3$ (aq.) and $[CaUO_2(CO_3)_3]^{2-}$. In the case of Am(III), the two dominant species were Am^{3+} (aq.) and the hydroxo complex $[Am(OH)]^{2+}$ (**Tab. 30**). The presence of such complex can be explained with the overall high pH values (8.0–8.3) throughout experiments III and IV.

Tab. 30 Dominant aquatic species of U(VI) and Am(III) in OPA pore water during diffusion experiments III (20 d) and IV (36 d) at the time of sampling.

Actinide tracer	**Pore water$_{diff=0d,\ 20d,\ 36\ d}$ / (mol/L)**
U(VI)	$Ca_2UO_2(CO_3)_3$ (aq.)
	$[CaUO_2(CO_3)_3]^{2-}$
Am(III)	$[Am(CO_3)]^+$
	$[Am(OH)]^{2+}$

7.8.2 Discussion of the U(VI) and Am(III) diffusion profiles

^{233}U(VI) was detectable from $\approx 10^{-5}$ mol/m³ down to $\approx 5 \times 10^{-9}$ mol/m³ and distances of 1426 µm and 1663 µm after 20 d and 36 d, respectively (**Fig. 45a,b**). ^{233}U concentrations in clay segments at longer distances were consistent with background ($\approx 8 \times 10^{-11}$ mol/m³). The diffusion profiles of ^{233}U(VI) showed a steady decrease in tracer concentration after both 20 d and 36 d of diffusion. D_e and K_d values, obtained by fitting the experimental diffusion profiles are listed in **Tab. 31**. D_e values of ^{233}U(VI) from the 20 d and 36 d experiments amounted to $(0.07\pm0.04)\times 10^{-10}$ m²/s and $0.12(+0.06/-0.05)\times 10^{-10}$ m²/s, respectively and were, within the respective uncertainties, equal to those obtained from diffusion experiment I (126 d), yet, lower than observed in experiment II (240 d). The K_d values after 20 d and 36 d (0.07±0.05 and 0.17±0.05 m³/kg) were identical within experimental uncertainties and comparable with the outcome of the two long experiments (running for 126 and 240 d).

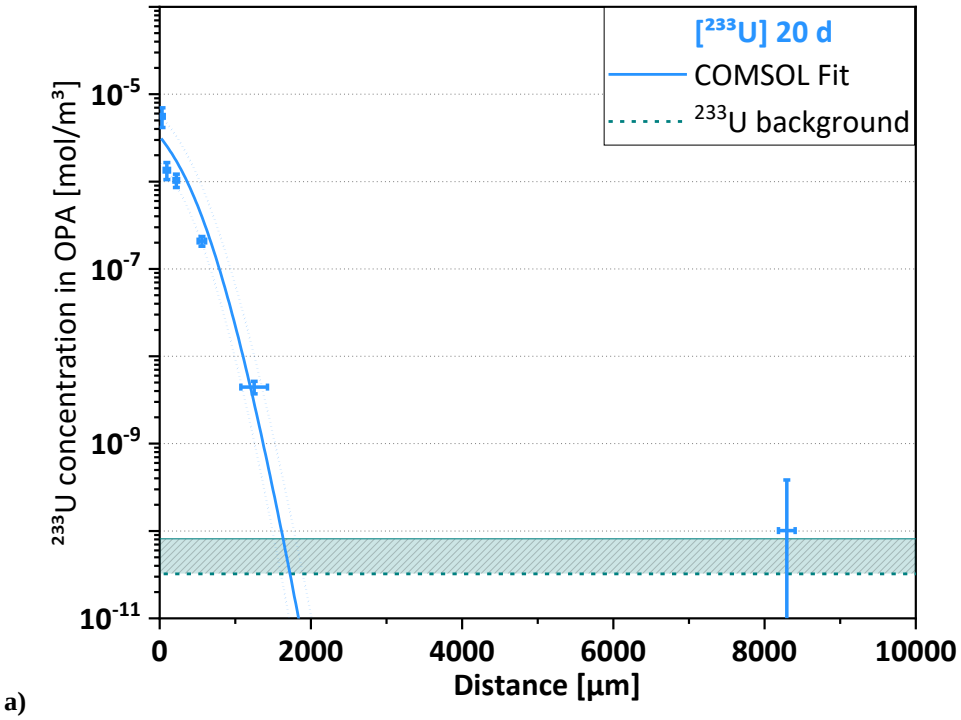

a)

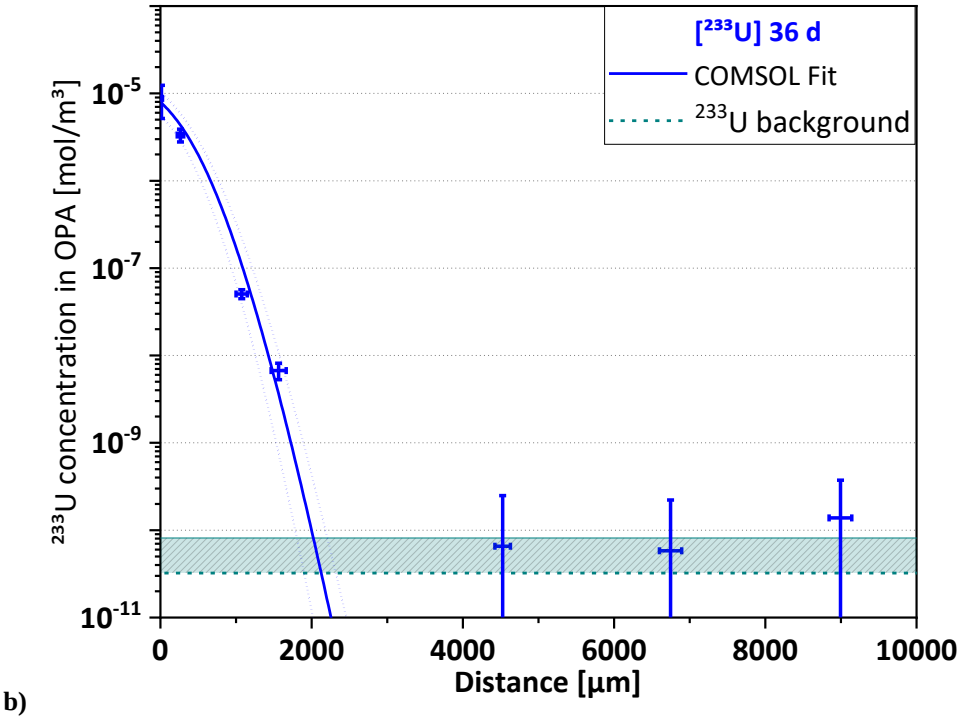

b)

Fig. 45 Experimentally obtained diffusion profiles of ^{233}U after **a)** 20 d and **b)** after 36 d.

Tab. 31 Parameter values for D_e and K_d for ^{233}U(VI) and ^{243}Am(III) obtained from diffusion experiments III & IV after 20 & 36 d of diffusion, respectively.

Parameter	^{233}U(VI) (20 d)	^{233}U(VI) (36 d)	^{243}Am(III), slow-diffusing species (20 d)	^{243}Am(III), slow-diffusing species (36 d)	^{243}Am(III), fast-diffusing species (36 d)
D_e / ($\times 10^{-10}$ m²/s)	0.07±0.04	0.12(+0.06/−0.05)	n.d.	1.4(+1.1/−0.9)	n.d.
D_a / ($\times 10^{-15}$ m²/s)	–	–	n.d.	3.8(+2.3/−1.8)	n.d.
K_d / (m³/kg)	0.07(+0.05/−0.03)	0.17±0.05	n.d.	15±5	n.d.

n.d.: not determined.

After 20 d of diffusion, only a slow-diffusing species profile was observed for ^{243}Am(III), extending to ≈ 250 µm with concentrations ranging between 2×10^{-6} mol/m³ and 10^{-8} mol/m³ (**Fig. 46a**). ^{243}Am concentrations in the clay segment at 559±50 µm, as well as in clay segments at longer distances were consistent with background.

After 36 d of diffusion, ^{243}Am(III) showed a two-part profile, comprising a slow-diffusing and a fast-diffusing species profile, similar to the ones in the previous two diffusion experiments. The slow-diffusing species profile exhibited a rapid decrease in ^{243}Am(III) concentration up to ≈ 1000 µm, from ≈ 7×10^{-6} mol/m³ to ≈ 8×10^{-10} mol/m³ (**Fig. 46b**). The fast-diffusing species profile was observed up to a distance of 4629 µm and was featured by a tailing of practically steady concentration, ranging between 2×10^{-10} mol/m³ and 10^{-9} mol/m³. The ^{243}Am concentration in the adjacent clay segment (6893±147 µm) was consistent with background (≈ 10^{-10} mol/m³).

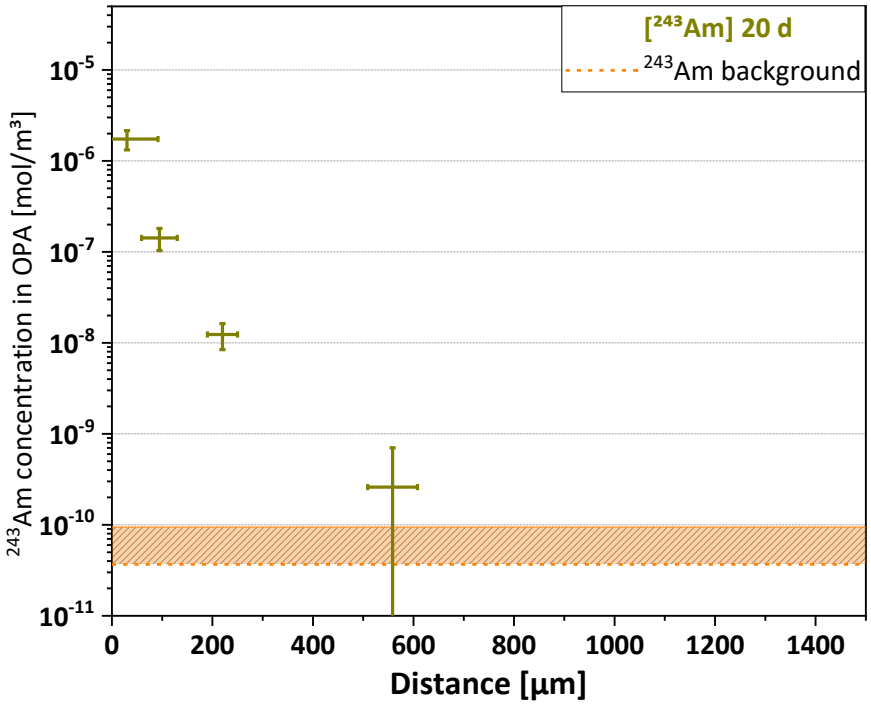

a)

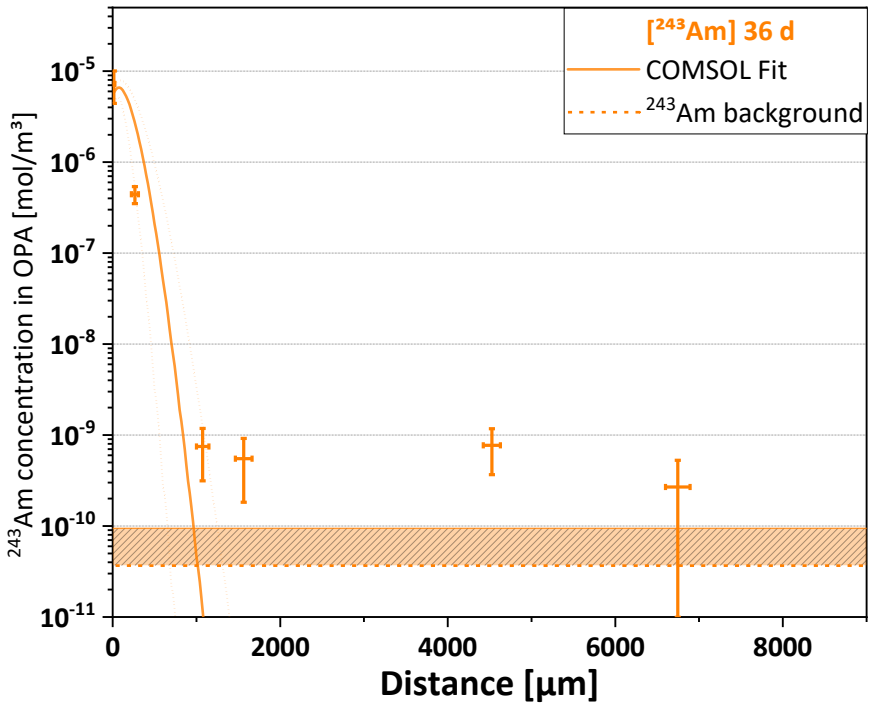

b)

Fig. 46 Experimentally obtained diffusion profiles of ^{243}Am after **a)** 20 d and **b)** after 36 d.

Due to the fact that only three data points of the slow-diffusing Am species profile after 20 d of diffusion were available, a profile fitting was not carried out and consequently, no D_e and K_d values were given. Fitting of the slow-diffusing species profile of Am(III) obtained after 36 d of diffusion resulted in K_d = 15±5 m³/kg, being in fairly good agreement with the K_d determined in a batch sorption experiment.[51] The D_a of the slow-diffusing species profile amounted to

3.8(+2.3/−1.8) × 10^{-15} m²/s and is significantly higher, than such obtained after 126 d of diffusion, whereas it equals, within its uncertainties, the D_a value derived from the 240 d diffusion experiment. However, the fitted profile is based only on three data points, thus, its uncertainty was fairly high, making the inter-comparison of the D_a values challenging.

The profile of the fast-diffusing Am species after 36 d of diffusion consisted of a tailing with practically constant ^{243}Am. Hence, D_e and K_d values could not be determined. Yet, for comparison, the fast-diffusing species profile after 36 d of diffusion was fitted with the D_e and K_d values of the fast-diffusing species profile obtained after 240 d of diffusion. As shown in **Fig. 47**, such fit follows the profile between approximately 1000 µm and 2000 µm, but considerably underestimates the profile for distances ≥ 2500 µm, indicating a potential difference in the transport mode of the fast-diffusing Am(III) species at higher (i.e., 10^{-5}–10^{-6} mol/m³) and lower concentrations (i.e., ≈ 10^{-9} mol/m³). There is currently no explanation available for such difference. A possible explanation for the origin of the fast-diffusing Am(III) fraction will be discussed below.

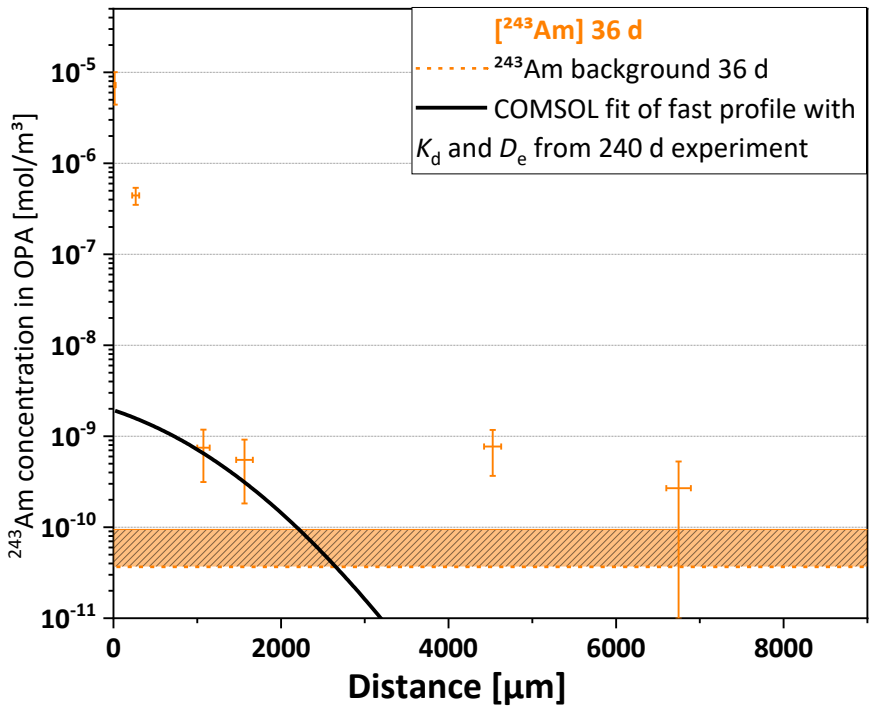

Fig. 47 Experimentally obtained diffusion profiles of ^{243}Am after 36 d. The fast-diffusing species profile was fitted with K_d = 0.2 m³/kg and D_e = 2 × 10^{-11} m²/s, obtained after 240 d of diffusion. The fit is shown as black line.

7.9 Hypothesis for the development of an Am(III) fast-diffusing species profile

With respect to the unexpectedly long diffusion distances of ^{243}Am ("profile tailing"), there were no indications for airborne and sample holder contamination as potential or actual sources of increased background and cross-contamination despite an extensive testing program (see sub-chapter 7.1). A more rapid tracer transport along the interface between the OPA cylinder rim and epoxy resin (e.g., due to fractures) was investigated and ruled out as well (see sub-chapter 0).

It was hypothesized, that apart from pore diffusion through the porous clay structure, there may was an additional transport path via water diffusion through micro-fractures in the OPA sample. In order to investigate the potential presence of such micro-fractures, two OPA specimens were scanned with µCT.

The first specimen was an OPA cylinder of the type as it was used in the diffusion experiments (**Fig. 48a**). It was contacted with synthetic OPA pore water for 300 d, which is approximately the same duration, as for clay diffusion sample II (i.e., 56 d of saturation and 240 d of diffusion).

The µCT scan revealed micro-fractures in the entire sample, approximately 40–80 µm wide. It is noteworthy, that the average diameter and the average volume fraction of such fractures increased from the distal side of the sample (≈ 1 % v/v) to the proximal side (≈ 5 % v/v), as it is shown in the 3D rendered structure in **Fig. 48b**. This can be explained with the decrease of confining pressure from the distal to the open proximal side which makes fracture formation at the proximal side more likely.

The second specimen was an unsaturated, raw piece of an OPA bore core, approximately 30×25 mm in dimension. The goal of the investigation was to elucidate, whether micro-fractures are already present in bore cores due to bore core drilling and evaporation of pore water or whether they are more likely to form upon the mechanical stress during machining (i.e., manufacturing of cylindrical diffusion samples) and the swelling pressure upon saturation with synthetic pore water.

The µCT scan of the unsaturated OPA sample showed micro-fractures along the entire scanning range (indicated as yellow cube in **Fig. 49**) with dimensions similar to the fractures found in the sample saturated with pore water. However, preliminary analysis of the scan suggests that the average volume fraction of the fractures is below 1 % v/v.

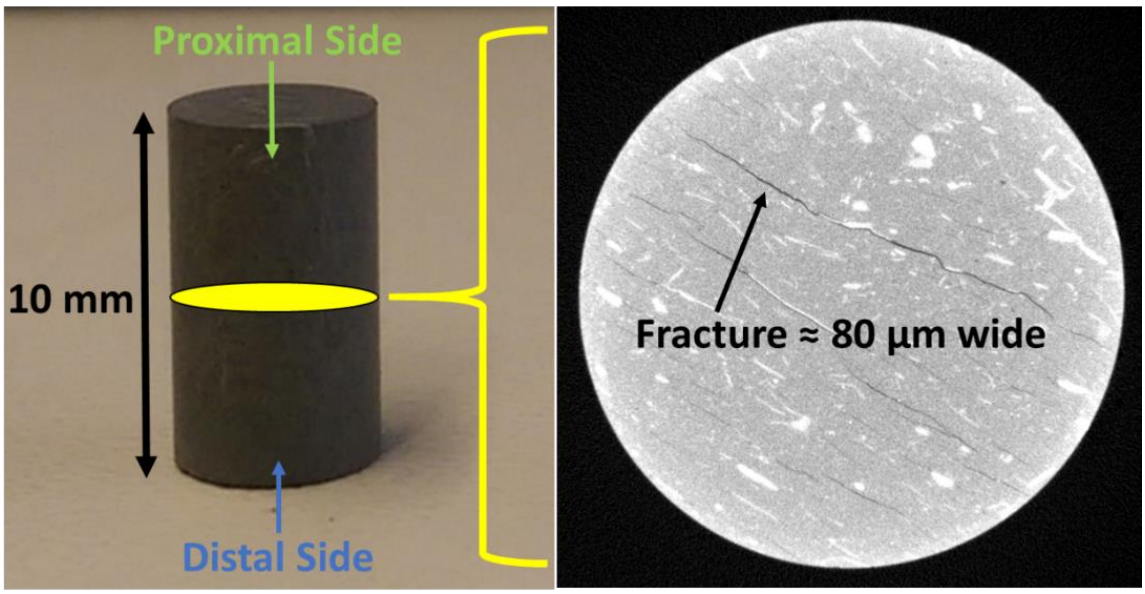

a)

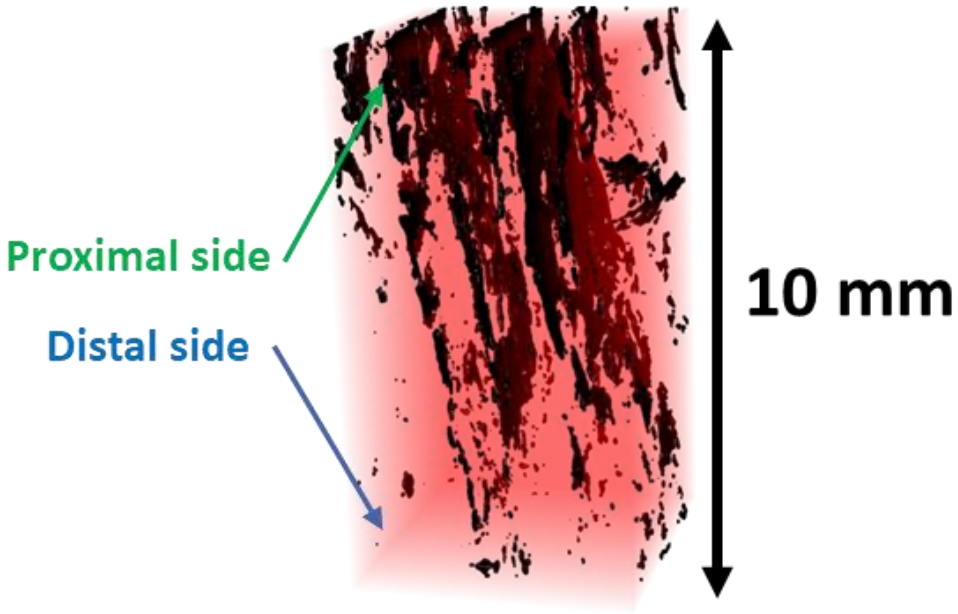

b)

Fig. 48 **a)** OPA cylinder contacted for 300 d with synthetic pore water; µCT scan at approximately 5 mm height, as indicated in yellow. Fracture highlighted with arrow: almost 6 mm long and 80 µm wide, **b)** 3D structure of OPA cylinder after segmentation. Fractures are represented as black areas, bulk clay matrix is highlighted in light red.

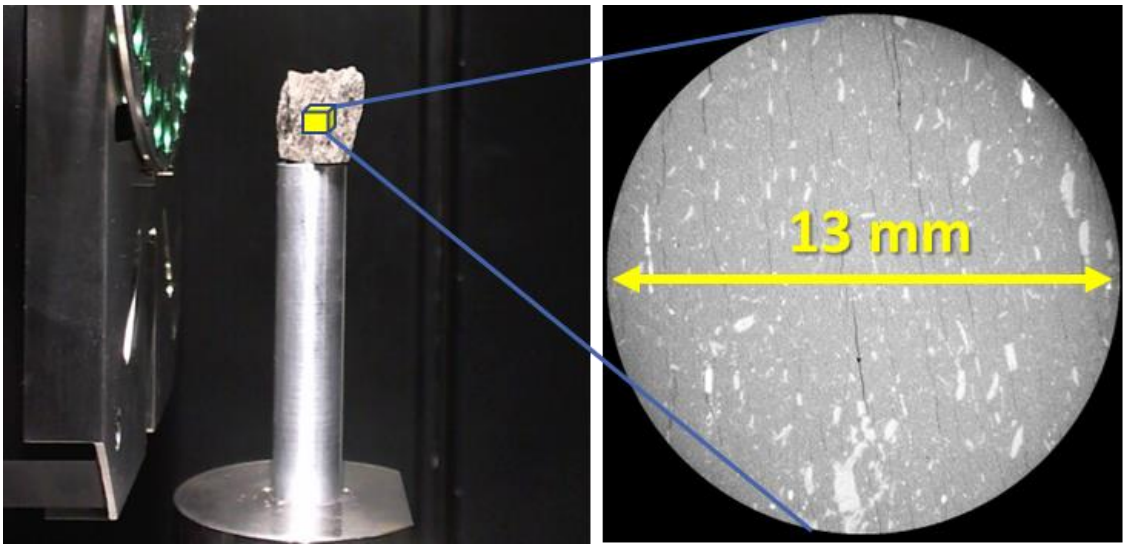

Fig. 49 Raw, unsaturated piece of OPA, mounted on a µCT sample holder (left); Exemplary CT image (right).

The results show that micro-fractures are already present in the OPA samples prior to fine machining and saturation with pore water. Fracture formation due to desaturation of pore water is unlikely, since the OPA specimen was kept in synthetic pore water until assembly in the µCT device. The fractures might occur during drilling of the bore cores or during the subsequent transportation. However, the swelling pressure evolving during saturation of OPA cylinders with synthetic pore water induces additional fractures, in particular towards the proximal sample side. It is very likely, that those pathways have an impact on radionuclide diffusion and are notably responsible for the fast-diffusing Am(III) fraction as discussed below.

7.10 Summary and comprehensive interpretation of diffusion profiles

For U(VI), all diffusion profiles gave fairly comparable D_e and K_d values (**Tab. 32**). All values were higher by about one order of magnitude than values reported in a previous study.[2] Given the differences in the experimental setups, the increase of D_e can be explained: In the literature study, the diffusion of U(VI) was studied perpendicular to the bedding with a confining pressure of 5 MPa, whereas in the present study diffusion was investigated parallel to the bedding without confining pressure. Both the parallel bedding and the absence of confining pressure facilitate a more rapid diffusive transport.

The overall higher K_d values compared to the one given in the cited study[2] might be explained with the lower HCO_3^-/CO_3^{2-} concentration in the diffusion reservoir solutions. As confirmed via DIC analysis, HCO_3^-/CO_3^{2-} concentrations were as low as $(8.1\pm0.3) \times 10^{-5}$ mol/L compared to approximately 4×10^{-4} mol/L.[2] It is well known that slight variations in HCO_3^-/CO_3^{2-} concentrations and pH has an impact on the formation of the neutral ternary

complex $Ca_2UO_2(CO_3)_3$ (aq.) and, thus, on sorption onto the clay minerals of the OPA.[97] A similar behavior is discussed by Hartmann *et al.* (2008)[99] for the sorption of U(VI) onto OPA and COx clay. In such study, the increase in U(VI) sorption at $pH \geq 8$ is explained by the limitation of CO_3^{2-} in solution by the precipitation of calcite.

Tab. 32 Parameter values for D_e and K_d for ^{233}U(VI) obtained from diffusion experiments I, II, III, and IV after 126, 240, 20, and 36 d of diffusion, respectively; comparison with parameter values available from literature.

Parameter	^{233}U(VI) profile (126 d)	^{233}U(VI) profile (240 d)	^{233}U(VI) profile (20 d)	^{233}U(VI) profile (36 d)	U(VI) profile, literature [2]
D_e / ($\times 10^{-10}$ m²/s)	0.08(+0.04/ −0.05)	0.16(+0.15/ −0.11)	0.07±0.04	0.12(+0.06/ −0.05)	0.019±0.004
K_d / (m³/kg)	0.05(+0.06/ −0.04)	0.10(+0.09/ −0.06)	0.07(+0.05/ −0.03)	0.17±0.05	0.025±0.003

The K_d values derived from the slow-diffusing species profiles of Am(III) were similar in all diffusion experiments and in fairly good agreement with literature data (**Tab. 33**). D_e values showed variations of more than one order of magnitude, ranging between $(1.1\pm0.4) \times 10^{-11}$ m²/s after 126 d and $1.5(+1.0/-0.6) \times 10^{-10}$ m²/s after 240 d of diffusion. The D_e obtained from the 126 d experiment is in good agreement with the literature value. There is currently no explanation available for such variation. However, it shall be noted that a significant variability in D_e values was also observed for Eu(III) diffusion in illite.[26]

Tab. 33 Parameter values for D_e, D_a, and K_d for the profile of the slow-diffusing ^{243}Am(III) species obtained from diffusion experiment I, II, and IV after 126, 240, and 36 d of diffusion, respectively; comparison with parameters available from literature.

Parameter	^{243}Am(III) (126 d)	^{243}Am(III) (240 d)	^{243}Am(III) (36 d)	Literature *)
D_e / ($\times 10^{-10}$ m²/s)	0.11±0.04	1.5(+1.0/−0.6)	1.4(+1.1/−0.9)	≈ 0.15
D_a / ($\times 10^{-15}$ m²/s)	0.22±0.02	1.0(+1.5/−0.5)	3.8(+2.3/−1.8)	≈ 0.7
K_d / (m³/kg)	20±5	60±20	15±5	30±2

*) D_e and D_a from diffusion experiment with Eu(III) in OPA for 200 d.[3] K_d from batch sorption experiment with Am(III) in OPA.[51]

The statistically most relevant fast-diffusing species profile of Am(III) was obtained from diffusion experiment II (240 d). Compared to the K_d values derived from the slow-diffusing species profiles of Am(III) and the published K_d value determined in a Am(III) sorption experiment with OPA, the modelled K_d of the fast-diffusing species profile is fairly low and

suggests a species which is poorly retarded by the clay (**Tab. 34**). Given the fractured structure of the OPA cylinders (see µCT scans in sub-chapter 7.9) it is hypothesized that a fraction of Am(III) was transported as colloid-bound species with an initial concentration approximately ten times lower than the aqueous Am(III) species. Such hypothesis could also explain, why no fast-diffusing species profile is observed for U(VI). It was shown in migration experiments in a granitic fracture zone that bentonite colloids can act as carrier of Am(III), while the interaction of U(VI) with colloids is negligible.[100]

While a fast-diffusing Am(III) species profile was detected after 36 d of diffusion, no such profile was observed after 20 d of diffusion. This could indicate that in the investigated concentration range (approximately 10^{-10}–10^{-9} mol/m³) the fast-diffusing species profile of Am(III) occurs between 20 d and 36 d after the start of the diffusion experiment. Another explanation could also be that the availability of micro-fractures varies for the different clay plugs used for the diffusion studies. It definitely cannot be assumed that the apertures and thicknesses of fractures are uniform in all samples. A variable occurrence of fast-diffusing radionuclide species in different experiments was also stated by Glaus *et al.* (2020)[26] in their studies on Cs(I) and Eu(III) diffusion in illite.

Tab. 34 Parameter values for D_e, K_d for profile of the fast-diffusing ^{243}Am(III) species obtained from diffusion experiment I and II after 126 and 240 d of diffusion, respectively.

Parameter	**^{243}Am(III) (126 d)**	**^{243}Am(III) (240 d)**	**^{243}Am(III) (20 d)**	**^{243}Am(III) (36 d)**
D_e / ($\times 10^{-10}$ m²/s)	≈ 0.20	0.19(+0.16/−0.14)	n.a.	n.d.
K_d / (m³/kg)	≈ 0.15	0.20(+0.04/−0.11)	n.a	n.d.

n.a.: parameters not available, since no fast-diffusing species profile was observed for 20 d experiment. n.d.: not determined.

It is worth noting that overall, D_e and K_d values derived from the diffusion experiments in the present study are consistent with literature data. Altered clay density and porosity due to the presence of the micro-fractures will certainly have an impact in particular on the transport parameters D_e and D_a and be responsible for the variation in data. The µCT observation on micro-fractures in clay samples provides a reasonable explanation for the observed fast-diffusing fraction of Am(III).

8 Conclusions and outlook

In the course of this Ph.D. work, an experimental procedure was developed, which allowed for the investigation of the diffusion behavior of actinide elements in clay materials at ultra-trace levels. Laboratory-scale diffusion experiments were conducted in OPA. By means of AMS, diffusion profiles of ^{233}U(VI) and ^{243}Am(III) were determined and D_e and K_d values derived down to ultra-trace concentrations of the investigated actinide nuclides. The outcomes of this work provide a significant contribution to understanding actinide mobility in the far-field of a HLW repository constructed in a clay rock as host rock.

Diffusion profiles of U(VI) showed a fairly good agreement with literature data. No indication was found for a change in diffusion behavior of U(VI), present at ultra-trace concentrations.

In case of Am(III) it was the first time that diffusion profiles were determined in OPA or a similar lithology. Diffusion profiles of Am(III) were featured by a strongly sorbing part with rapid decrease in concentrations and a “fast runner” part with a much smaller concentration gradient. Such two-part profile is also known for the diffusion of Eu(III) used as an analogue for trivalent actinides. µCT scans of OPA specimens revealed the presence of fractures in the micrometer range, potentially facilitating a colloid-mediated transport of Am(III) species along such fractures. Colloid-mediated radionuclide migration is not to be expected in a clay rock formation under confined conditions as it is the case under the lithostatic pressure in a DGR. Such type of migration processes might be of potential relevance locally in the case of perturbed clay. Such perturbation could be the impact of evolving H_2 overpressure caused by container corrosion, leading to fracture (re)activation. In the context of diffusion in undisturbed clay rock such fast-diffusing radionuclide fractions are not to be expected.

Future investigations should focus on the further investigation of the hypothesis of colloid-mediated transport through fractures in OPA. The in part fairly high uncertainties of the fitted D_e and K_d values could be reduced by AMS analysis of a higher number of clay segments. Furthermore, more comprehensive modelling of the fast-diffusing species profile of Am(III) shall be performed, comprising the geometry of the fractured OPA specimens.

9 References

1. Gimmi, T., Leupin, O. X., Eikenberg, J., Glaus, M. A., Loon, L. R. Van, Waber, H. N., Wersin, P., Wang, H. A. O., Grolimund, D., Borca, C. N., Dewonck, S. & Wittebroodt, C. Anisotropic diffusion at the field scale in a 4-year multi-tracer diffusion and retention experiment - I: Insights from the experimental data. *Geochim. Cosmochim. Acta* **125**, 373–393 (2014).

2. Joseph, C., Van Loon, L. R., Jakob, A., Steudtner, R., Schmeide, K., Sachs, S. & Bernhard, G. Diffusion of U(VI) in Opalinus Clay: Influence of temperature and humic acid. *Geochim. Cosmochim. Acta* **109**, 74–89 (2013).

3. LES-PSI. Progress Report 2019. *Annual Reports*. Paul Scherrer Institut, Villigen, Switzerland (2019).

4. Bröskamp, H., Brammer, K.-J. & Graf, R. Endlagerung radioaktiver Abfälle in Deutschland: Abfallaufkommen und Endlagerverfügbarkeit aus EVU-Sicht. *atw 49. Jahrgang* Heft 4 – April, 248–254 (2004).

5. Bundesgesetzblatt. *Gesetz zur Suche und Auswahl eines Standortes für ein Endlager für hochradioaktive Abfälle (Standortauswahlgesetz - StandAG)*. BGBl. I S. 1074/2017 idF BGBl. I S. 1328/2020.

6. Gompper, K., Geist, A. & Geckeis, H. Actinoidenabtrennung aus hochradioaktiven Abfällen. *Nachchrichten aus der Chemie* **58**, 1015–1019 (2010).

7. Nagra. Demonstration of disposal feasibility for spent fuel, vitrified high-level waste and long-lived intermediate-level waste (Entsorgungsnachweis). *Technial Report NTB 02-05*. Nagra, Wettingen, Switzerland (2002).

8. SKB. Long-term safety for KBS-3 repositories at Forsmark and Laxemar – a first evaluation: Main Report of the SR-Can project. *Technical Report TR-06-09*. SKB, Stockholm, Sweden (2006).

9. Wu, T., Amayri, S., Drebert, J., Van Loon, L. R. & Reich, T. Neptunium(V) sorption and diffusion in Opalinus Clay. *Environ. Sci. Technol.* **43**, 6567–6571 (2009).

10. Joseph, C., Mibus, J., Trepte, P., Müller, C., Brendler, V., Park, D. M., Jiao, Y., Kersting, A. B. & Zavarin, M. Long-term diffusion of U(VI) in bentonite: Dependence on density. *Sci. Total Environ.* **575**, 207–218 (2017).

11. Yamaguchi, T., Nakayama, S., Nagao, S. & Kizaki, M. Diffusive transport of neptunium and plutonium through compacted sand-bentonite mixtures under anaerobic conditions. *Radiochim. Acta* **95**, 115–125 (2007).

12. Sawaguchi, T., Yamaguchi, T., Iida, Y., Tanaka, T. & Kitagawa, I. Diffusion of Cs, Np, Am and Co in compacted sand-bentonite mixtures: evidence for surface diffusion of Cs cations. *Clay Miner.* **48**, 411–422 (2013).

13. Pearson, F. J., Arcos, D., Bath, A., Boisson, J. Y., Fernández, A. M., Gäbler, H. E., Gaucher, E., Gautschi, A., Griffault, L., Hernán, P. & Waber, H. N. Mont Terri Project – Geochemistry of water in the Opalinus Clay formation at the Mont Terri rock laboratory. *Reports of the Federal Office for Water and Geology, Geology Series No. 5*. Federal Office for Water and Geology, Bern, Switzerland (2003).

14. Quinto, F., Golser, R., Lagos, M., Plaschke, M., Schäfer, T., Steier, P. & Geckeis, H. Accelerator mass spectrometry of actinides in ground- and seawater: An innovative method allowing for the simultaneous analysis of U, Np, Pu, Am, and Cm isotopes below ppq levels. *Anal. Chem.* **87**, 5766–5773 (2015).

15. Quinto, F., Blechschmidt, I., Garcia Perez, C., Geckeis, H., Geyer, F., Golser, R., Huber, F., Lagos, M., Lanyon, B., Plaschke, M., Steier, P. & Schäfer, T. Multiactinide analysis with accelerator mass spectrometry for ultratrace determination in small samples: Application to an in situ radionuclide tracer test within the colloid formation and migration experiment at the Grimsel test site (Switzerland). *Anal. Chem.* **89**, 7182–7189 (2017).

16. Glückman, D., Quinto, F., Hain, K., Joseph, C., Montoya, V., Steier, P. & Geckeis, H. Concurrent determination of U, Np, Pu, Am, and Cm in clay systems at ultra-trace levels with accelerator mass spectrometry. *J. Anal. At. Spectrom.* **37**, 1696–1705 (2022).

17. Villar, M. V. Thermo-hydro-mechanical characterisation of the Bentonite of a simulated HLW repository after five years operation (in situ test of the FEBEX project). *Informes Técnicos Ciemat 1049*. Ciemat, Madrid, Spain (2004).

18. Villar, M. V. MX-80 Bentonite. Thermo-hydro-mechanical characterisation performed at CIEMAT in the Context of the prototype project. *Informes Técnicos Ciemat 1053*. Ciemat, Madrid, Spain (2005).

19. Gautschi, A. Safety-relevant hydrogeological properties of the claystone barrier of a

Swiss radioactive waste repository: An evaluation using multiple lines of evidence. *Grundwasser* **22**, 221–233 (2017).

20. Zhang, C.-L., Czaikowski, O. & Rothfuchs, T. Thermo-hydro-mechanical behaviour of the Callovo-Oxfordian Clay rock. *Report GRS-266.* Braunschweig, Germany (2010).

21. Jasmund, K., Lagaly, G. (Eds.) *Tone und Tonminerale*. Steinkopff, Darmstadt, Germany (1993).

22. Van Loon, L. R., Soler, J. M., Müller, W. & Bradbury, M. H. Anisotropic diffusion in layered argillaceous rocks: A case study with Opalinus Clay. *Environ. Sci. Technol.* **38**, 5721–5728 (2004).

23. Tournassat, C., Bourg, I. C., Steefel, C. I. & Bergaya, F. Surface Properties of Clay Minerals. *Developments in Clay Science* **6**, 5–31 (2015).

24. Schulze, D. G. *Clay Minerals*. Encyclopedia of Soils in the Environment (pp. 246–254), Elsevier, Amsterdam, Netherlands (2005).

25. Wimpenny, J. *Clay Minerals*. Encyclopedia of Geochemistry. Encyclopedia of Earth Sciences Series (pp. 265–275), Springer, Cham, Switzerland (2018).

26. Glaus, M. A., Frick, S. & Van Loon, L. R. A coherent approach for cation surface diffusion in clay minerals and cation sorption models: Diffusion of Cs^{+} and Eu^{3+} in compacted illite as case examples. *Geochim. Cosmochim. Acta* **274**, 79–96 (2020).

27. Krejci, P., Gimmi, T. & Van Loon, L. R. On the concentration-dependent diffusion of sorbed cesium in Opalinus Clay. *Geochim. Cosmochim. Acta* **298**, 149–166 (2021).

28. Keller, L. M., Holzer, L., Wepf, R. & Gasser, P. 3D geometry and topology of pore pathways in Opalinus clay: Implications for mass transport. *Appl. Clay Sci.* **52**, 85–95 (2011).

29. Bourg, I. C. & Tournassat, C. Self-diffusion of water and ions in clay barriers. *Developments in Clay Science* **6**, 189–226 (2015).

30. Keller, L. M., Holzer, L., Schuetz, P. & Gasser, P. Pore space relevant for gas permeability in Opalinus clay: Statistical analysis of homogeneity, percolation, and representative volume element. *J. Geophys. Res. Solid Earth* **118**, 2799–2812 (2013).

31. Wigger, C. & Van Loon, L. R. Importance of interlayer equivalent pores for anion diffusion in clay-rich sedimentary rocks. *Environ. Sci. Technol.* **51**, 1998–2006 (2017).

32. Mont Terri Project. https://www.mont-terri.ch/de/mont-terri-projekt/organisation.html (2022).

33. Hoth, P., Wirth, H., Reinhold, K., Krull, P. & Feldrappe, H. Untersuchung und Bewertung von Tongesteinsformationen. *Endlagerung radioaktiver Abfälle in tiefen geoloischen Formationen Deutschlands*. Bundesanstalt für Geowissenschaften und Rohstoffe (BGR), Hannover, Germany (2007).

34. Voegelin, A., Kretzschmar, R. Stability and Mobility of Colloids in Opalinus Clay. *Technical Report NTB 02-14*. Nagra, Wettingen, Switzerland (2002).

35. Bossart, P. & Thury, M. Mont Terri Rock Laboratory. Project , Programme 1996 to 2007 and Results. *Reports of the Swiss Geological Survey No. 3*. Swiss Geological Survey, Wabern, Switzerland (2008).

36. Pearson, F. J. Opalinus Clay experimental water: A1Type, Version 980318. *PSI Internal report TM-44-98-07*. Paul Scherrer Institut, Villigen, Switzerland (1998).

37. Fernández, A. M., Turrero, M. J., Sánchez, D. M., Yllera, A., Melón, A. M., Sánchez, M., Peña, J., Garralón, A., Rivas, P., Bossart, P. & Hernán, P. On site measurements of the redox and carbonate system parameters in the low-permeability Opalinus Clay formation at the Mont Terri Rock Laboratory. *Phys. Chem. Earth* **32**, 181–195 (2007).

38. Wersin, P., Johnson, L. H., Schwyn, B., Berner, U. & Curti, E. Redox Conditions in the Near Field of a Repository for SF/HLW and ILW in Opalinus Clay. *Technical Report NTB 02-13*. Nagra, Wettingen, Switzerland (2003).

39. Reich, T., Amayri, S., Börner, P. J. B., Drebert, J., Fröhlich, D. R., Grolimund, D. & Kaplan, U. Speciation of neptunium during sorption and diffusion in natural clay. *J. Phys. Conf. Ser.* **712**, 5–9 (2016).

40. Bossart, P. Characteristics of the Opalinus Clay at Mont Terri. *Reports of the Swiss Geological Survey No. 3*. Swiss Geological Survey, Wabern (2008).

41. Archie, G. E. The electrical resistivitylog as an aid in determining some reservoir characteristics. *Transaction of the AIME* **146**, 54–62 (1942).

42. Molera, B. M. & Eriksen, T. Diffusion of $^{22}Na^{+}$, $^{85}Sr^{2+}$, $^{134}Cs^{+}$ and $^{57}Co^{2+}$ in bentonite clay compacted to different densities: experiments and modeling. *Radiochim. Acta* **90**, 753–760 (2002).

43. Van Loon, L. R., Baeyens, B. & Bradbury, M. H. Diffusion and retention of sodium and strontium in Opalinus Clay: Comparison of sorption data from diffusion and batch sorption measurements, and geochemical calculations. *Appl. Geochemistry* **20**, 2351–2363 (2005).

44. Loon, L. R. Van, Soler, J. M. & Bradbury, M. H. Diffusion of HTO , $^{36}Cl^-$ and $^{125}I^-$ in Opalinus Clay samples from Mont Terri Effect of confining pressure. *J. Contam. Hydrol.* **61**, 73–83 (2003).

45. Dasent, W. E. *Inorganic Energetics: An Introduction*. Camebridge University Press, Camebridge, United Kingdom (1982).

46. Van Loon, L. R. & Müller, W. A modified version of the combined in-diffusion/abrasive peeling technique for measuring diffusion of strongly sorbing radionuclides in argillaceous rocks: A test study on the diffusion of caesium in Opalinus Clay. *Appl. Radiat. Isot.* **90**, 197–202 (2014).

47. Wersin, P., Soler, J. M., Van Loon, L., Eikenberg, J., Baeyens, B., Grolimund, D., Gimmi, T. & Dewonck, S. Diffusion of HTO, Br^-, I^-, Cs^+, $^{85}Sr^{2+}$ and $^{60}Co^{2+}$ in a clay formation: Results and modelling from an in situ experiment in Opalinus Clay. *Appl. Geochemistry* **23**, 678–691 (2008).

48. Bradbury, M. H. & Baeyens, B. A generalised sorption model for the concentration dependent uptake of caesium by argillaceous rocks. *J. Contam. Hydrol.* **42**, 141–163 (2000).

49. Bradbury, M. & Baeyens, B. Far field sorption data bases for performance assessment of a high-level radioactive waste repository in an undisturbed Opalinus Clay host rock, *PSI-Report 03-08*. Paul Scherrer Institut, Villigen, Switzerland (2003).

50. Fröhlich, D. R., Amayri, S., Drebert, J. & Reich, T. Influence of humic acid on neptunium(V) sorption and diffusion in Opalinus Clay. *Radiochim. Acta* **101**, 553–560 (2013).

51. Amayri, S., Fröhlich, D. R., Kaplan, U., Trautmann, N. & Reich, T. Distribution coefficients for the sorption of Th, U, Np, Pu, and Am on Opalinus Clay. *Radiochim. Acta* **104**, 33–40 (2016).

52. Loveland, W., Morissey, D. J. & Seaborg, G. T. *Modern Nuclear Chemistry, Second Edition*. John Wiley & Sons, Inc., Hoboken, New Jersey, United States (2017).

53. Kautenburger, R., Brix, K. & Hein, C. Applied Geochemistry Insights into the retention behaviour of europium(III) and uranium(VI) onto Opalinus Clay influenced by pore water composition, temperature, pH and organic compounds. *Appl. Geochemistry* **109**, 104404 (2019).

54. Turner, D. R., Pabalan, R. T. & Paul, F. Neptunium(V) sorption on montmorillonite: An experimental and surface complexation modeling study. *Clays Clay Miner.* **46**, 256–269 (1998).

55. Altmann, S., Tournassat, C., Goutelard, F., Parneix, J., Gimmi, T. & Maes, N. Diffusion-driven transport in clayrock formations. *Appl. Geochemistry* **27**, 463–478 (2012).

56. Glaus, M. A., Frick, S., Rosse, R. & Van Loon, L. R. Comparative study of tracer diffusion of HTO , $^{22}Na^{+}$ and $^{36}Cl^{-}$ in compacted kaolinite, illite and montmorillonite. *Geochim. Cosmochim. Acta* **74**, 1999–2010 (2010).

57. Van Loon, Luc R., Soler, J. M. Diffusion of HTO, $^{36}Cl^{-}$ and $^{125}I^{-}$ and $^{22}Na^{+}$ in Opalinus Clay: Effect of confining pressure, sample orientation, sample depth and temperature. *PSI-Report 04-03*. Paul Scherrer Institut, Villigen, Switzerland (2004).

58. Kamp, G. Van Der, Stempvoort, D. R. Van & Wassenaar, L. I. The radial diffusion method: 1. Using intact cores to determine isotopic composition, chemistry, and effective porosities for groundwater in aquitards. *Water Resour. Res.* **32**, 1815–1822 (1996).

59. Savoye, S., Michelot, J., Wittebroodt, C. & Altinier, M. V. Contribution of the diffusive exchange method to the characterization of pore-water in consolidated argillaceous rocks. *J. Contam. Hydrol.* **86**, 87–104 (2006).

60. Savoye, S., Michelot, J.-L. & Wittebroodt, C. Evaluation of the reversibility of iodide uptake by argillaceous rocks by the radial diffusion method. *Radiochim. Acta* **94**, 699–704 (2006).

61. Aldaba, D., García-Gutiérrez, M., Abrão, T., Rigol, A. & Vidal, M. Transport of radioselenium oxyanions by diffusion in unsaturated soils. *Radiochim. Acta* **103**, 501–511 (2015).

62. García-Gutiérrez, M., Cormenzana, J. L., Missana, T., Alonso, U. & Mingarro, M. Diffusion of strongly sorbing cations (^{60}Co and ^{152}Eu) in compacted FEBEX bentonite. **36**, 1708–1713 (2011).

63. Missana, T. & Geckeis, H. (Eds.) The CRR Final Project Report Series II: Supporting Laboratory Experiments with Radionuclides and Bentonite Colloids. *Technical Report NTB 03-02*. Nagra, Wettingen, Switzerland (2006).

64. Bennett, C. L., Beukens, R. P., Clover, M. R., Elmore, D., Gove, H. E., Kilius, L., Litherland, A. E. & Purser, K. H. Radiocarbon dating with electrostatic accelerators: dating of milligram samples. *Am. Assoc. Adv. Sci.* **201**, 345–347 (1978).

65. Nishiizumi, K., Arnold, J. R., Elmore, D., Ferraro, R. D., Gove, H. E., Finkel, R. C., Beukens, R. P., Chang, K. H. & Kilius, L. R. Measurements of ^{36}Cl in Antarctic meteorites and Antarctic ice using a Van de Graaff accelerator. *Earth Planet. Sci. Lett.* **45**, 285–292 (1979).

66. Henning, W., Bell, W. A., Billquist, P. J., Glagola, B. G., Kutschera, W., Liu, Z., Lucas, H. F., Paul, M., Rehm, K. E. & Yntema, J. L. Calcium-41 concentration in terrestrial materials: Prospects for dating of pleistocene samples. *Science* **236**, 725–727 (1987).

67. Quinto, F., Busser, C., Faestermann, T., Hain, K., Koll, D., Korschinek, G., Kraft, S., Ludwig, P., Plaschke, M., Schäfer, T. & Geckeis, H. Ultratrace determination of ^{99}Tc in small natural water samples by accelerator mass spectrometry with the gas-filled analyzing magnet system. *Anal. Chem.* **91**, 4585–4591 (2019).

68. Elmore, D., Gove, H. E., Ferraro, R., Kilius, L. R., Lee, H. W., Chang, K. H., Beukens, R. P., Litherland, A. E., Russo, C. J., Purser, K. H., Murrell, M. T. & Finkel, R. C. Determination of ^{129}I using tandem accelerator mass spectrometry. *Nature* **286**, 138–140 (1980).

69. Hain, K., Steier, P., Froehlich, M. B., Golser, R., Hou, X., Lachner, J., Nomura, T., Qiao, J., Quinto, F. & Sakaguchi, A. ^{233}U/^{236}U signature allows to distinguish environmental emissions of civil nuclear industry from weapons fallout. *Nat. Commun.* **11**, 1275 (2020).

70. Hain, K., Faestermann, T., Famulok, N., Fimiani, L., Gómez-Guzmán, J. M., Korschinek, G., Kortmann, F., Lierse V. Gostomski, C., Ludwig, P. & Shinonaga, T. Analytical method for the determination of Np and Pu in sea water by AMS with respect to the Fukushima accident. *Nucl. Instruments Methods Phys. Res. Sect. B Beam Interact. with Mater. Atoms* **361**, 505–509 (2015).

71. Quinto, F., Hrnecek, E., Krachler, M., Shotyk, W., Steier, P. & Winkler, S. R. Determination of ^{239}Pu, ^{240}Pu, ^{241}Pu and ^{242}Pu at femtogram and attogram levels-

evidence for the migration of fallout plutonium in an ombrotrophic peat bog profile. *Environ. Sci. Process. Impacts* **15**, 839–847 (2013).

72. Winkler, S. R., Steier, P., Buchriegler, J., Lachner, J., Pitters, J., Priller, A. & Golser, R. He stripping for AMS of accelerator of ^{236}U and other actinides using a 3 MV tandem accelerator. *Nucl. Inst. Methods Phys. Res. B* **361**, 458–464 (2015).

73. Steier, P., Hain, K., Klötzli, U., Lachner, J., Priller, A., Winkler, S. & Golser, R. The actinide beamline at VERA. *Nucl. Inst. Methods Phys. Res. B* **458**, 82–89 (2019).

74. Steier, P., Dellinger, F., Forstner, O., Golser, R., Knie, K., Kutschera, W., Priller, A., Quinto, F., Srncik, M., Terrasi, F., Vockenhuber, C., Wallner, A., Wallner, G. & Wild, E. M. Analysis and application of heavy isotopes in the environment. *Nucl. Instruments Methods Phys. Res. Sect. B Beam Interact. with Mater. Atoms* **268**, 1045–1049 (2009).

75. Boulyga, S. F. & Heumann, K. G. Determination of extremely low ^{236}U/^{238}U isotope ratios in environmental samples by sector-field inductively coupled plasma mass spectrometry using high-efficiency sample introduction. *J. Environ. Radioact.* **88**, 1–10 (2006).

76. Middleton, R., Juenemann, D. & Klein, J. Isotopic fractionation of negative ions produced by Cs sputtering in a high-intensity source. *Nucl. Inst. Methods Phys. Res. B* **93**, 39–51 (1994).

77. Vogel, J. S. Neutral resonant ionization in the high-intensity cesium sputter source. *AIP Conf. Proc.* **1515**, 89–98 (2013).

78. Vockenhuber, C., Ahmad, I., Golser, R., Kutschera, W., Liechtenstein, V., Priller, A., Steier, P. & Winkler, S. Accelerator mass spectrometry of heavy long-lived radionuclides. *Int. J. Mass Spectrom.* **223**–**224**, 713–732 (2003).

79. Steier, P., Bichler, M., Keith Fifield, L., Golser, R., Kutschera, W., Priller, A., Quinto, F., Richter, S., Srncik, M., Terrasi, P., Wacker, L., Wallner, A., Wallner, G., Wilcken, K. M. & Maria Wild, E. Natural and anthropogenic ^{236}U in environmental samples. *Nucl. Inst. Methods Phys. Res. B* **266**, 2246–2250 (2008).

80. Quinto, F., Golser, R., Lagos, M., Plaschke, M., Schäfer, T., Steier, P. & Geckeis, H. Accelerator mass spectrometry of actinides in ground- and seawater: An innovative method allowing for the simultaneous analysis of U, Np, Pu, Am, and Cm isotopes below ppq levels. *Anal. Chem.* **87**, 5766–5773 (2015).

81. Christl, M., Dai, X., Lachner, J., Kramer-Tremblay, S. & Synal, H. A. Low energy AMS of americium and curium. *Nucl. Inst. Methods Phys. Res. B* **331**, 225–232 (2014).

82. López-Lora, M. & Chamizo, E. Accelerator Mass Spectrometry of ^{237}Np, ^{239}Pu and ^{240}Pu for environmental studies at the Centro Nacional de Aceleradores *Nucl. Inst. Methods Phys. Res. B* **455**, 39–51 (2019).

83. Quinto, F., Hrnecek, E., Krachler, M., Shotyk, W., Steier, P. & Winkler, S. R. Measurements of ^{236}U in ancient and modern peat samples and implications for postdepositional migration of fallout radionuclides. *Environ. Sci. Technol.* **47**, 5243–5250 (2013).

84. Gräsele, W. & Plischke, I. LT Experiment: Strength and deformation of Opalinus Clay. *Technical Report 2007-05*. Bundesanstalt für Geowissenschaften und Rohstoffe (BGR), Hannover, Germany (2007).

85. Dahler, D. P. Diffusionsexperimente mit stark sorbierenden Radionukliden in Tongestein, *diploma thesis*. Johannes Gutenberg-Universität, Mainz, Germany (2018).

86. Zeisel, S. Diffusion von Neptunium und Cäsium in Tongestein, *diploma thesis*. Johannes Gutenberg-Universität, Mainz, Germany (2018).

87. Van Loon, L. R. & Eikenberg, J. A high-resolution abrasive method for determining diffusion profiles of sorbing radionuclides in dense argillaceous rocks. *Appl. Radiat. Isot.* **63**, 11–21 (2005).

88. Xiao, G., Liu, Y. & Jones, R. L. Determination of ^{237}Np and ^{239}Pu in urine using sector field inductively coupled plasma mass spectrometry (SF-ICP-MS). *J. Radioanal. Nucl. Chem.* **324**, 887–896 (2020).

89. Gross, J. H. *Massenspektrometrie - Ein Lehrbuch*. Springer, Berlin, Germany (2011).

90. Linge, K. L. & Jarvis, K. E. Quadrupole ICP-MS: Introduction to instrumentation, measurement techniques and analytical capabilities. *Geostand. Geoanalytical Res.* **33**, 445–467 (2009).

91. Croudace, I. W., Russell, B. C. & Warwick, P. W. Plasma source mass spectrometry for radioactive waste characterisation in support of nuclear decommissioning: A review. *J. Anal. At. Spectrom.* **32**, 494–526 (2017).

92. Carter, J. A., Barros, A. I., Nóbrega, J. A. & Donati, G. L. Traditional calibration

methods in atomic spectrometry and new calibration strategies for inductively coupled plasma mass spectrometry. *Front. Chem.* **6**, 1–25 (2018).

93. Becker, J., Biebl, F., Glatt, E., Cheng, L., Grießer, A., Groß, M., Linden, S., Mosbach, D., Wagner, C., Weber, A., & Westerteiger, R. GeoDict (Release 2022) [Simulation software]. Math2Market GmbH (2022).

94. Parkhurst, D. L. & Appelo, C. A. J. Description of Input and Examples for PHREEQC Version 3—A Computer Program for Speciation, Batch-Reaction, One-Dimensional Transport, and Inverse Geochemical Calculations. *U.S. Geological Survey Techniques and Methods, book 6, chap. A43,* (2013).

95. ThermoChimie Partners. Thermochimie version 10 database. https://www.thermochimie-tdb.com/, ANDRA, Châtenay-Malabry, France (2018).

96. COMSOL. Multiphsysics version 5.6. https://www.comsol.com, COMSOL AB, Stockholm, Sweden (2022).

97. Tournassat, C., Tinnacher, R. M., Grangeon, S. & Davis, J. A. Modeling uranium(VI) adsorption onto montmorillonite under varying carbonate concentrations: A surface complexation model accounting for the spillover effect on surface potential. *Geochim. Cosmochim. Acta* **220**, 291–308 (2018).

98. Maes N., Glaus M., Baeyens B., Marques Fernandes M., Churakov S., Dähn R., Grangeon S., Tournassat C., Geckeis H., Charlet L., Brandt F., Poonoosamy J., Hoving A., Havlova V., Fischer C., Scheinost A., Noseck U., Britz S., Siitari-Kauppi M., Missana, T. *State-of-the-Art report on the understanding of radionuclide retention and transport in clay and crystalline rocks.* Final version as of 30.04.2021 of deliverable D5.1 of the HORIZON 2020 project EURAD. EC Grant agreement no: 847593 (2021).

99. Hartmann, B. E., Geckeis, H., Rabung, T., Lützenkirchen, J. & Fanghänel, T. Sorption of radionuclides onto natural clay rocks. *Radiochim. Acta* **96**, 699–707 (2008).

100. Geckeis, H., Schäfer, T., Hauser, W., Rabung, T., Missana, T., Degueldre, C., Möri, A., Eikenberg, J., Fierz, T. & Alexander, W. R. Results of the colloid and radionuclide retention experiment (CRR) at the Grimsel Test Site (GTS), Switzerland - impact of reaction kinetics and speciation on radionuclide migration. *Radiochim. Acta* **92**, 765–774 (2004).

Appendix

Appendix A

Tab. A1 Diffusion experiment II (240 d): Count rates of ^{233}U, ^{243}Am, and internal standards ^{236}U and ^{248}Cm [cts/s] in diffusion samples (DS-11 to DS-24, as well as core and rim segments), calibration samples (Cal-4 to Cal-6), and blank samples (Blank 6 to Blank 9); corresponding tracer concentrations [mol/m³]; concentrations in diffusion and calibration samples are blank and CIY corrected and normalized to count rates of internal tracers ^{236}U and ^{248}Cm.

Sample name	Ctr(^{233}U) / s^{-1}	^{233}U concentration in sample / (mol/m³)	Ctr(^{243}Am) / s^{-1}	^{243}Am concentration in sample / (mol/m³)	Ctr(^{236}U) / s^{-1}	Ctr(^{248}Cm) / s^{-1}
Blank 6–9*)	(3.6±0.6)×10^{-3}	(1.2±1.1)×10^{-10}	(7.3±0.1)×10^{-1}	(7.2±0.6)×10^{-8}	1.9±0.1	9.1±0.2
DS-11	(8.1±1.5)×10^{-3}	(4.7±1.4)×10^{-9}	(7.8±0.2)×10^{-1}	<	1.9±0.1	8.4±0.1
DS-12	(1.4±0.4)×10^{-2}	(7.4±2.4)×10^{-9}	(9.7±0.2)×10^{-1}	<	1.2±0.1	4.9±0.1
DS-13	(3.4±1.1)×10^{-3}	(1.7±0.9)×10^{-10}	(1.9±0.1)×10^{-1}	<	1.1±0.1	6.8±0.1
DS-C1	4.2±0.1	(1.0±0.1)×10^{-7}	(3.7±0.1)×10^{-1}	<	2.0±0.1	5.1±0.1
DS-C1-R1	(5.7±1.3)×10^{-3}	(1.1±0.5)×10^{-9}	(2.9±0.1)×10^{-1}	<	1.8±0.1	7.9±0.1
DS-C1-R3	(9.2±0.5)×10^{-2}	(1.4±0.5)×10^{-8}	(5.0±0.1)×10^{-1}	<	1.7±0.1	7.6±0.1
DS-C2	(9.7±0.1)×10^{-2}	(2.7±0.2)×10^{-6}	(1.2±0.1)×10^{2}	(6.3±1.8)×10^{-5}	5.0±0.1	2.4±0.1
DS-C2-R1	(1.2±0.1)×10^{-2}	(2.6±0.2)×10^{-7}	(3.0±0.1)×10^{-1}	<	1.1±0.1	5.6±0.1
DS-C2-R4	(3.3±0.1)×10^{1}	(2.6±0.1)×10^{-6}	(1.1±0.1)×10^{1}	(1.7±0.5)×10^{-6}	1.6±0.1	5.3±0.1
DS-14	(2.2±0.1)×10^{1}	(6.1±0.4)×10^{-6}	4.1±0.1	(1.3±0.5)×10^{-6}	1.9±0.1	9.7±0.1
DS-15	(1.4±0.1)×10^{1}	(1.9±0.1)×10^{-5}	3.6±0.1	(5.4±0.2)×10^{-6}	3.4±0.1	(1.9±0.1)×10^{1}
DS-16	(2.0±0.1)×10^{1}	(4.0±0.2)×10^{-5}	3.4±0.1	(1.0±0.3)×10^{-5}	2.8±0.1	(1.3±0.1)×10^{1}
DS-17	(5.2±0.1)×10^{1}	(9.3±0.5)×10^{-5}	5.9±0.1	(1.6±0.5)×10^{-5}	3.5±0.1	(1.6±0.1)×10^{1}
DS-18	(9.1±0.1)×10^{1}	(1.4±0.1)×10^{-4}	9.9±0.1	(2.4±0.7)×10^{-5}	3.5±0.1	(1.6±0.1)×10^{1}
DS-19	(1.2±0.1)×10^{2}	(5.4±0.2)×10^{-4}	4.7±0.1	(2.6±0.9)×10^{-5}	2.1±0.1	(1.3±0.1)×10^{1}
DS-20	(2.1±0.1)×10^{1}	(4.0±0.4)×10^{-4}	3.4±0.1	(9.6±3.0)×10^{-6}	5.0±0.1	(2.3±0.1)×10^{1}
DS-21	(4.6±0.1)×10^{1}	(7.6±0.6)×10^{-4}	3.8±0.1	(8.8±2.5)×10^{-5}	5.2±0.1	(2.6±0.1)×10^{1}
DS-22	(7.2±0.2)×10^{-1}	(1.7±0.3)×10^{-3}	2.3±0.1	(8.8±2.9)×10^{-3}	4.2±0.1	(1.8±0.1)×10^{1}
DS-23	1.3±0.1	(4.4±0.1)×10^{-4}	(1.1±0.1)×10^{2}	(6.2±1.7)×10^{-2}	4.6±0.1	(1.8±0.1)×10^{1}

DS-24	$(2.5\pm0.1)\times10^{-1}$	$(1.3\pm0.1)\times10^{-4}$	$(7.0\pm0.1)\times10^{1}$	$(6.4\pm1.7)\times10^{-2}$	4.9±0.1	$(2.0\pm0.1)\times10^{1}$
Cal-4	15.5±0.1		7.2±0.1		4.7±0.1	1.9±0.1
Cal-5	16.6±0.1	**)	7.9±0.1	**)	5.0±0.1	2.4±0.1
Cal-6	8.6±0.1		4.4±0.1		2.7±0.1	1.4±0.1

<: consistent with background. *) Indicated values are mean values, determined from Blank 6–9 **) nominal ≈ 10^{-16} mol of spike per calibration sample.

Tab. A2 Diffusion experiment III (20 d): Count rates of ^{233}U, ^{243}Am, and internal standards ^{236}U and ^{248}Cm [cts/s] in diffusion samples (DS-25 to DS-31) calibration sample (Cal-7), and blank samples (Blank 10, 12, and 13); corresponding tracer concentrations [mol/m³]; indicated concentrations in diffusion and calibration samples are blank and CIY corrected and normalized to count rates of internal tracers ^{236}U and ^{248}Cm.

Sample name	**Ctr(^{233}U) / s^{-1}**	**^{233}U concentration in sample / (mol/m³)**	**Ctr(^{243}Am) / s^{-1}**	**^{243}Am concentration in sample / (mol/m³)**	**Ctr(^{236}U) / s^{-1}**	**Ctr(^{248}Cm) / s^{-1}**
Blank 10, 12, and 13 *)	$(4.5\pm4.4)\times10^{-4}$	$(3.3\pm4.9)\times10^{-11}$	$(3.8\pm1.5)\times10^{-4}$	$(3.7\pm5.8)\times10^{-11}$	1.6±0.3	7.6±0.8
DS-25	$(3.8\pm5.3)\times10^{-4}$	<	– *)	<	2.2±0.1	8.9±0.1
DS-26	– **)	<	– *)	<	1.2±0.1	1.0±0.1
DS-27	$(6.3\pm0.5)\times10^{-3}$	$(4.4\pm0.4)\times10^{-9}$	– *)	<	2.3±0.1	1.3±0.1
DS-28	$(4.5\pm0.1)\times10^{-1}$	$(2.1\pm0.1)\times10^{-7}$	$(7.5\pm6.4)\times10^{-4}$	<	1.7±0.1	1.0±0.1
DS-29	1.5±0.1	$(1.0\pm0.1)\times10^{-6}$	$(2.0\pm0.3)\times10^{-2}$	$(1.2\pm0.3)\times10^{-8}$	2.1±0.1	1.1±0.1
DS-30	$(6.6\pm0.3)\times10^{-1}$	$(1.4\pm0.2)\times10^{-6}$	$(1.1\pm0.1)\times10^{-1}$	$(1.4\pm0.2)\times10^{-7}$	$(3.9\pm0.1)\times10^{-1}$	3.0±0.1
DS-31	2.3±0.1	$(5.6\pm0.7)\times10^{-6}$	1.3±0.1	$(1.7\pm0.2)\times10^{-6}$	$(4.1\pm0.1)\times10^{-1}$	$(3.3\pm0.1)\times10^{-1}$
Cal-7	9.7±0.1	***)	1.2±0.1	***)	1.4±0.1	6.6±0.1

<: consistent with background. *) Indicated values are mean values, determined from Blank 10, 12, and 13. Blank 11 was discarded from data treatment due to short measurement times **) Zero counts detected, thus, no concentration determined. ***) nominal ≈ 10^{-16} mol of spike per calibration sample.

Tab. A3 Diffusion experiment IV (36 d): Count rates of ^{233}U, ^{243}Am, and internal standards ^{236}U and ^{248}Cm [cts/s] in diffusion samples (DS-32 to DS-39) and corresponding tracer concentrations [mol/m³]; indicated concentrations in diffusion and calibration samples are blank and CIY corrected and normalized to count rates of internal tracers ^{236}U and ^{248}Cm.

Sample name	Ctr(^{233}U) / s^{-1}	^{233}U concentration in sample / (mol/m³)	Ctr(^{243}Am) / s^{-1}	^{243}Am concentration in sample / (mol/m³)	Ctr(^{236}U) / s^{-1}	Ctr(^{248}Cm) / s^{-1}
DS-32	$(7.5\pm6.4)\times10^{-4}$	<	– **)	<	2.0±0.1	$(1.1\pm0.1)\times10^{1}$
DS-33	$(3.5\pm4.8)\times10^{-4}$	<	$(1.7\pm0.8)\times10^{-3}$	$(1.8\pm2.0)\times10^{-10}$	1.4±0.1	7.3±0.1
DS-34	$(3.8\pm5.3)\times10^{-4}$	<	$(6.0\pm1.5)\times10^{-3}$	$(6.5\pm2.8)\times10^{-10}$	1.7±0.1	$(1.1\pm0.1)\times10^{1}$
DS-35	$(2.9\pm0.3)\times10^{-2}$	$(6.6\pm0.8)\times10^{-9}$	$(3.0\pm1.0)\times10^{-3}$	$(4.1\pm2.9)\times10^{-10}$	2.1±0.1	$(1.3\pm0.1)\times10^{1}$
DS-36	$(1.8\pm0.1)\times10^{-1}$	$(5.1\pm0.3)\times10^{-8}$	$(4.0\pm1.1)\times10^{-3}$	$(5.7\pm3.6)\times10^{-10}$	1.8±0.1	$(1.3\pm0.1)\times10^{1}$
DS-37	2.9±0.1	$(3.3\pm0.3)\times10^{-6}$	$(8.1\pm0.6)\times10^{-1}$	$(4.4\pm0.5)\times10^{-7}$	1.1±0.1	$(1.1\pm0.1)\times10^{1}$
DS-38	$(4.1\pm0.2)\times10^{-1}$	$(8.8\pm1.2)\times10^{-6}$	2.4±0.1	$(7.2\pm1.4)\times10^{-6}$	$(4.1\pm0.1)\times10^{-1}$	3.3±0.1
DS-39	$(1.5\pm0.4)\times10^{-2}$	$(1.9\pm0.2)\times10^{-6}$	$(1.1\pm0.1)\times10^{-1}$	$(1.7\pm1.1)\times10^{-6}$	$(4.6\pm0.1)\times10^{-1}$	3.7±0.1

<: consistent with background. **) Zero counts detected, thus, no concentration determined.

Appendix B

Tab. B1 Actinide tracer stock solutions: concentrations, matrices, and isotopic compositions of the of ^{233}U, ^{236}U, ^{243}Am, and ^{248}Cm solutions.

Nuclide	Concentration / (mol/L)	Matrix	Manufacturer / description	Isotopic composition / atom %
^{233}U	(4.680±0.083) × 10^{-3}	HNO_3, 5 mol/L	Institute for Reference Materials and Measurements, Geel, Belgium / certified reference material IRMM-040a	^{233}U 98.0201±0.0098 ^{238}U < 0.83 ^{236}U < 0.03
^{236}U	(4.359±0.004) × 10^{-4}	HNO_3, 1 mol/L	Institute for Reference Materials and Measurements, Geel, Belgium / certified reference material IRMM-3660a	^{236}U 99.97333±0.00004 ^{233}U 0.00000343±0.00000003 ^{238}U 0.02254±0.00004
^{243}Am	(1.302±0.008) × 10^{-5}	HNO_3, 0.1 mol/L	In-house	^{243}Am 96.983±0.006 ^{241}Am 3.0453±0.0004 ^{233}U < 0.006 ^{238}U 0.003334±0.000002 ^{236}U < 0.0004
^{248}Cm	(1.158±0.020) × 10^{-7}	HNO_3, 0.3 mol/L	In-house	^{248}Cm 99.986±0.006 ^{238}U 0.00798±0.00004 ^{233}U < 0.006 ^{236}U < 0.0006 ^{241}Am < 0.0006 ^{243}Am < 0.0001

Tab. B2 Concentrations of ^{233}U, ^{236}U, ^{243}Am, and ^{248}Cm in diluted solutions, given in mol/L.

Nuclide	Dilution 1	Dilution 2	Dilution 3	Dilution 4
^{233}U	1.00 × 10^{-4}	9.95 × 10^{-8}	4.68 × 10^{-11}	–
^{236}U	1.40 × 10^{-5}	1.67 × 10^{-8}	1.61 × 10^{-11}	–
^{243}Am	1.30 × 10^{-5}	1.51 × 10^{-8}	1.39 × 10^{-11}	1.65 × 10^{-12}
^{248}Cm	7.95 × 10^{-11}	2.31 × 10^{-12}	–	–

Analytical uncertainty of concentrations < 2 %